Quantifying emissions and flame geometry of lab-scale air-assisted flares

by

Sina Mobaseri

A thesis submitted in partial fulfillment of the requirements for the degree of

Master of Science

Department of Mechanical Engineering

University of Alberta

© Sina Mobaseri, 2021

Abstract

Flaring has been a routine practice in the petroleum and petrochemical industry and flaring levels have remained virtually constant over the past ten years despite the efforts to reduce or eliminate the activity. Injecting an inert fluid into the combustion area in order to induce complete combustion of hydrocarbons and suppress smoke is referred to as assisting and the fluid of choice is commonly steam or air. Emissions from air-assisted flares have been studied but flame shape characteristics and the effects of operating parameters such as fuel heating value, burner size, etc. on emissions and flame geometry remain to be systematically studied. Two geometrically similar stainless steel burners with a scaling factor of 2:1 were built with a tube-in-tube design where the larger burner (2" burner) measured 50.8mm in outer tube and 25.4mm in inner tube outside diameter. Air was delivered through the inner tube and fuel flowed in the annular region between the two tubes. Propane was used as hydrocarbon fuel and it was diluted with CO_2 maintaining a total flow rate of either 10 or 20SLPM with propane mixture fractions of 100, 70, 50 and 30% by volume to achieve different fuel heating values. Air flow was increased from zero up to 225SLPM or flame blow-off, whichever was achieved first. The plume of combustion products was captured through an exhaust hood above the flame and directed into a duct, downstream of which samples were drawn through a probing tube and directed to the diagnostic equipment suite for black carbon (BC), NO_x and CO_2 concentrations to be measured which were subsequently converted to per unit mass of fuel emission indices (EI) through a carbon-based closed mass balance technique. Digital instantaneous pictures of the flame were taken continuously at a rate of 3-4Hz and a software package was devised to process the photographs and extract flame intermittency contours. Flame length and width were defined as the height and width of the box bounding the 50% intermittency contours of the flames.

Results of the 2" burner with 20SLPM pure propane as fuel showed BC emissions of 0.35g/kgFuel to remain unchanged with increasing air assist up to a mass flow ratio (MFR) of 1.3 and to decrease by multiple orders of magnitude past this point (e.g., two orders of magnitude by MFR=2.5) down to being fully suppressed by further increasing the air assist. At lower flow rates of air assist a second flame was observed to sit on the tip of the inner tube which blew off with increasing MFR. Interestingly, the blow-off point was observed to be concurrent with the onset of BC suppression. NO_x emission index increased monotonously from 1.7g/kgFuel at zero assist up to 2.3g/kgFuel at MFR=8.8. Flame length went up from 74.0cm at zero assist up to 92.2cm at MFR=3.3, then decreased by further increasing assist, while flame width starting at 16.5cm decreased monotonically after inner flame blow off with assist flow rate. At about the same point where flame length decay began, a narrowing of the flame just above the burner occurred. This "neck" became narrower and closer to the burner as assist was further increased. The same overall patterns were observed with lowering fuel heating value or flow rate for emissions but fuels with lower heating values had generally lower emission indices than pure propane and lowering fuel flow resulted in BC suppression onset MFR to be delayed. Additionally, the peaking pattern was not observed in 10SLPM fuel flow cases and flame lengths were not observed to significantly increase before going down. In the smaller burner BC suppression started at a much smaller MFR of 0.3 and changing fuel flow rate did not impact the observed flame length or BC emission patterns. A dilution-corrected air assist-fuel mixture fraction was introduced and an empirical exponent of 0.2 best fit the different fuel dilutions.

Acknowledgements

I would like to acknowledge the kind support of my thesis supervisor Dr. Larry Kostiuk whose deep technical and scientific knowledge always inspired me to learn more, and his intellectual support got me through a very tough time during my studies caused by the horrific downing of flight PS572 which was a great shock to everyone in the campus community, only to be followed by the COVID-19 pandemic which would among other things intermittently interrupt the research by multiple campus closures throughout the past year. Our discussions and his sincere guidance became a beacon of hope during these tough times. I would also like to thank Dr. Jason Olfert for his contribution to the research as my co-supervisor by facilitating the use of his lab space and equipment and providing his precious insight throughout the course of my studies. I also acknowledge the help of my fellow research associates in the FlareNet team at the University of Alberta, particularly Milad Zamani for his help with getting started with setting up the lab equipment and Dr. Ehsan Abbsasi-Atibeh for providing me with his insight into flame visualization techniques.

Table of Contents

1 Introduction **1**
1.1 Previous studies on flares . . . 5
1.2 Research Objectives . . . 10

2 Experimental Setup and methodology **12**
2.1 Experimental setup . . . 12
2.2 Diagnostic equipment . . . 16
2.3 Data acquisition procedure . . . 17
2.4 Data processing techniques . . . 17
2.4.1 Emission data . . . 18
2.4.2 Imaging and image processing . . . 20

3 Results and discussion **25**
3.1 Results of Base Case . . . 26
3.1.1 Visual Appearance of Flame . . . 26
3.1.2 Black carbon and NO_x emissions . . . 29
3.1.3 Characterization of Flame Size and Shape . . . 30
3.2 Emission indices results - all cases . . . 31
3.2.1 BC emissions . . . 31
3.2.2 NO_x emissions . . . 33
3.3 Characterization of Flame Size and Shape - all cases . . . 35
3.4 Investigating normalized BC emission factors and potential correlations in emission and flame shape . . . 38

4 Conclusion **42**
4.1 Recommendations for future work . . . 44

A Uncertainty analysis **52**
A.1 Methodology . . . 52
A.2 Error propagation for Emission Indices . . . 54
A.3 Emission measurement uncertainty analysis . . . 56
A.3.1 Mass flow controllers . . . 57
A.3.2 NOx Analyser . . . 57
A.3.3 PAX Black Carbon measurement . . . 57

B Full-size plots **59**
B.1 BC emission index plots 59
B.2 Flame length plots 63
B.3 Flame width plots 67

C Sample raw instantaneous flame images **71**
C.1 Long exposure images 71
C.2 Flame image progression for all cases 72

D MATLAB image processing code **78**

List of Tables

2.1 Measured dimensions of the 2" and 1" burners 14

3.1 Testing matrix and attributes of the cases. Each row in the table corresponds to a dataset presented in the results and discussion section. Reynolds numbers for air (Re_{air}) and fuel (Re_f) were calculated at room temperature for the flow rates tested. 26

List of Figures

1.1 Annual flaring (in billion cubic meters) and oil production (million barrels per day) from 1996 to 2019 based on satellite imaging. Data adapted from [44] 3

2.1 Schematic of the experimental setup and diagnostic equipment. . . . 15
2.2 a) Schematic of the burner exit port. Glass beads and steel mesh cloths were used in the 2" burner for flow straightening. b) View of the 2" burner mounted on the frame 16
2.3 User interface of the software, where a preview of raw and processed images is displayed and the processing parameters can be chosen . . . 21
2.4 The 10, 50 and 90% contours are displayed, and if the results are satisfactory they can be saved 23
2.5 Tentative necking locations are marked and the user could decide on the actual location 24

3.1 Long exposure flame images for 10 SLPM pure propane on 2" burner case before inner flame blow-off. Refer to Appendix C for more select long exposure pictures of flames with an inner flame 27
3.2 Instantaneous images of the flame for the base case. A pale radiance of the inner flame attached to the inner tube is visible for MFR=0.99 and 1.31. Assist flow is increased from left to right. The inner flame is blown off at MFR=1.42. For instantaneous images of all other cases refer to Appendix C. 28
3.3 Emission results for the base case (20prCO2-TwoOne-fuel100percent). Black carbon emissions are depicted on log scale, PAX detection limit is shown by a red dashed line (a), NO_x emission index is shown on linear scale (b) 29
3.4 Flame size characterization for the base case. 31

3.5 Black carbon emission indices on log scale. Emission indices remain constant with increasing assist flow until they start to be suppressed by multiple orders of magnitude. Fuel flow rates of 20SLPM are depicted by solid and 10 by hollow markers. Black color corresponds to pure propane and blue, cyan and green show increasing levels of dilution(a, b, and c). The two cases for 1" burner are marked by navy blue stars (d). Detection limit of PAX is marked by red dashed lines. Refer to section B.1 for full-size plots 33
3.6 NOx emission indices for all cases. Emissions go down with increasing dilution levels and go up with increasing assist MFR 34
3.7 Flame length variations with air assist flow. For high fuel flow rates, flame length peaks at some intermediate MFR before starting to drop(c) while it remains constant up to a point before starting to shrink for low fuel flow rate cases (a, and b). Refer to section B.2 for full-size plots 36
3.8 Flame width variations with air assist flow show a decreasing trend with air assist MFR. Refer to section B.3 for full-size plots 37
3.9 Flame neck height above burner (a) and width (b) variations with air assist flow. For all cases it was observed that the neck location lowered down closer to the burner exit and became narrower in width with increasing air assist MFR. 38
3.10 BC emission indices normalized by EI_0, i.e. EI_{BC} of the respective case at zero air assist, plotted against MFR (a), air assist mixture mass fraction (b), and dilution-corrected air assist mixture fraction (c). High fuel flow rate cases are shown by solid lines and markers. Low fuel low rate cases are represented by dashed lines and hollow markers 39
3.11 Flame visual and emission characteristics for 20SLPM fuel flow rate of pure propane (a) and 50% diluted propane (b) on 2" burner 40
3.12 Flame visual and emission characteristics for 10SLPM fuel flow rate of pure propane (a) and 50% diluted propane (b) on 2" burner 41

C.1 Long exposure images of 20 SLPM pure propane flame on 1" burner. The inner flame is ignited and elongated with increasing the assist flow rate (a-c), and is finally blown off (d) 71
C.2 Long exposure images of 10 SLPM pure propane flame on 1" burner. The inner flame is lifted just before blow-off (c) 72
C.3 Instantaneous images of the flame for the *20prCO2-TwoOne-fuel100percent* case (base case) (also provided in section 3.1) 73
C.4 Instantaneous images of the flame for the *10prCO2-TwoOne-fuel100percent* case 73
C.5 Instantaneous images of the flame for the *20prCO2-OneHalf-fuel100percent* case 74
C.6 Instantaneous images of the flame for the *10prCO2-OneHalf-fuel100percent* case 74

C.7 Instantaneous images of the flame for the *20prCO2-TwoOne-fuel70percent* case 75
C.8 Instantaneous images of the flame for the *10prCO2-TwoOne-fuel70percent* case 75
C.9 Instantaneous images of the flame for the *20prCO2-TwoOne-fuel50percent* case 76
C.10 Instantaneous images of the flame for the *10prCO2-TwoOne-fuel50percent* case 76
C.11 Instantaneous images of the flame for the *20prCO2-TwoOne-fuel30percent* case 77
C.12 Instantaneous images of the flame for the *10prCO2-TwoOne-fuel30percent* case 77

Chapter 1

Introduction

Flares are commonly utilized in the upstream as well as downstream petroleum and petrochemical industries to dispose of, through an open atmospheric flame, unwanted flammable gasses that can not be otherwise safely handled or consumed due to infrastructural, economic, etc. constraints. Flaring is specifically preferred over direct venting of these gasses primarily due to methane's staggering global warming potential (GWP) estimated to be 25-40 based on a 100-year GWP basis [15]. According to the Intergovernmental Panel on Climate Change (IPCC) GWP is defined as "the time-integrated commitment to climate forcing from the instantaneous release of 1 kg of a trace gas expressed relative to that from 1 kg of carbon dioxide" [5]. Even though methane has the highest GWP among the volatile organic compounds (VOC) prevalent in the petroleum industry, other hydrocarbons can also be significant greenhouse effect contributors. Ethane and propane, for instance, are shown to have a total (combined direct and indirect) 100-year GWP of 5.5 and 3.3, respectively [34].

Flaring in petroleum and petrochemical plants can be classified into production, process and emergency flaring [1]. Production flaring occurs when the flammable gasses produced as a by-product in oil fields (associated gas) where there is no provision for its processing, or its commercial utilization is prohibited due to factors like meager produced quantities or sourness of the gas due to existence of excessive sulfur-

containing compounds in the associated gas. Process flaring occurs when flammable gasses leak past safety valves, or at greater rates when they need to be disposed of during unit shut-down or off-specification start-up. Emergency flaring refers to scenarios when large quantities of flammable gasses need to be safely disposed of in an emergency such as fire, power or cooling water loss, over-pressurization of vessels, etc.

Attempts have been made to quantify global gas flaring levels based on satellite imaging. One survey estimated 140 to 170 billion cubic meters (BCM) of gas was flared annually from 1994 through 2008. The amount of gas flared in 2008 alone amounts to 21% of the US natural gas consumption, equivalent to $68 billion if dispatched to retail markets [13]. Despite consistent increasing oil production levels, gas flaring has declined since 1994 and remained somewhat constant in the past 10 years. According to an initiative launched by the World Bank in partnership with the National Oceanic and Atmospheric Administration (NOAA) which estimated annual flaring from satellite observations, 140 to 150 BCM gas was flared annually from 2009 to 2019, which shows a 38% decrease in flaring intensity (gas flared per barrel of oil produced) compared with 1996, given that oil production has gone up from 69 to 95 million barrels per day since then (Figure 1.1) [44]. Despite international attempts to curb flaring and replace the practice with more sustainable and commercial alternatives, like the World Bank's initiative to achieve zero routine flaring by 2030, Global Gas Flaring Reduction Partnership (GGFR), flaring is still commonly happening around the world. However, partner countries in the initiative have proven to limit flaring more successfully. For example, flaring intensity in 2019 was 50% lower than in 1996 for GGFR partner countries, compared with the 18% reduction achieved by non-partner countries [42].

Emissions from flares have been a matter of concern, more-so over the past two decades and multiple studies have attempted at quantifying them. In the region in close vicinity to the flaring site, plumes can negatively impact soil, vegetation

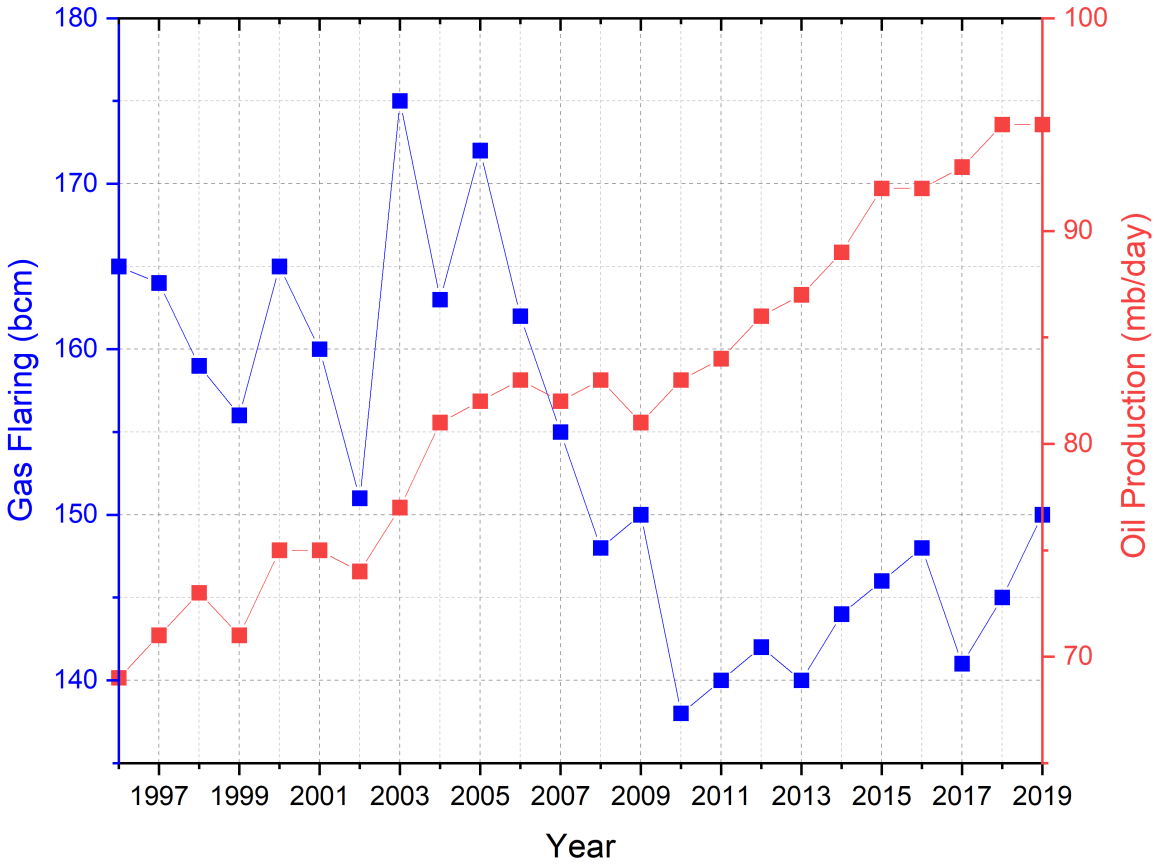

Figure 1.1: Annual flaring (in billion cubic meters) and oil production (million barrels per day) from 1996 to 2019 based on satellite imaging. Data adapted from [44]

and crops yield especially through inducing acid rain, black carbon deposition on soil, surfaces, water, etc., and raising soil temperatures [2, 14, 18]. At a global level, incomplete combustion of the flare gas can contribute to black carbon (BC) or unburned hydrocarbons (predominantly methane given that it is the main constituent of natural gas) emissions. BC is formed when carbon particles are cooled down before getting an opportunity to combust in the hot region of the flame and thus remain in the plume in the form of soot. BC, the light-absorbing fraction of soot, is of particular concern due to its potential contribution to global warming, making it the second most potent contributor only after CO_2, since it can deposit on arctic ice, heat the air and darken surfaces due to its high radiative forcing (RF) defined as

the change in radiative energy absorption due to the addition of a substance to the atmosphere [28, 5]. A recent study based on particle chemistry transport simulations has shown that BC emitted from flares can constitute 42-52% (in different times of the year) of the total BC surface concentrations in the Arctic, while only 3% of the global BC emissions can be attributed to flares. This might be partly due to the abundance of flares on oil sites at high latitudes in Russia, given that Russia is by far the leading contributor to gas flaring globally [27, 31]. Unburned hydrocarbons, on the other hand can be significant greenhouse effect contributors due to their high GWP as discussed earlier.

One of the common approaches adopted in industry to achieve better performance by flares, i.e. achieve complete combustion and suppress smoke, is the addition of a secondary fluid to the flame zone to enhance air-fuel mixing in the flame zone and increase ambient air entrainment by inducing turbulence. Most inefficiencies in flares can be attributed to fuel-rich conditions and therefore can be mitigated by ensuring a more uniform distribution of air throughout the combustion zone [32]. This technique is referred to as "assisted flares" and given the two most common assist media, air or steam, the system is termed air-assisted or steam-assisted flare. Steam-assisting is the more common technique practiced since it can suppress smoking more efficiently by not only adding momentum and improving air mixing, but also by participation in the chemistry of the combustion process [29]. For achieving the same suppression more mass of air is required as compared with steam which could drive installation and operation costs up [46]. Steam is also commonly available at petrochemical facilities where flaring occurs, so using it is more feasible when the infrastructure is already in place. However, steam assisting may not always be a practical choice in scenarios where the infrastructure for producing steam is not available or injecting steam is not a viable option due to environmental factors such as risk of freezing and water condensation due to extreme cold temperatures or scarcity of water resources in

arid areas such as the middle east [12]. However both steam and air are shown to be effective at promoting combustion efficiency and suppressing soot [19, 21]. The EPA's title 40 of Code of Federal Regulation (CFR), discusses regulations pertaining to safe operation of flares in part §60.18 . The article calls for the existence of a flame at all times and no visible smoke from flares except for periods that are shorter than five minutes in any two consecutive hours, and sets lower bounds for fuel heating values as well as upper bounds for the fuel exit velocity for different fuels and flare assist types [47]. These regulations might potentially encourage over-steaming or over-aerating of the flame to the point of compromising the stability of the flame as some studies have reported direct venting of fuel gasses in assisted flares [38]. Such observations led to a non-regulatory enforcement alert in 2012 by the EPA warning against excessive use of assist fluids and recommended constant monitoring of vent gas and assist ratios, especially during low vent gas flow periods [25].

1.1 Previous studies on flares

Most guidelines and studies pertaining to flares, are focused on emissions and specifically smoke, while flame visual characteristics are usually considered in a safety context only. API standard 521 for instance, recommends a minimum distance from the epicenter of the flame based on radiative characteristics of the flames for different fuels and provides rough estimates of the flame length and distortion due to wind, but cautions that the estimates should be treated as an upper bound for flame lengths since they do not consider assist and assisting makes the flame shorter and less radiant, but fails to provide further estimates for assisted flares [45]. There is a body of research on flares in cross-flow with a focus on flame shape and combustion efficiency. Bourguignon et al. studied a 1" flare stack in a closed-loop wind tunnel under different wind conditions and reported combustion efficiencies 91% or higher by mon-

itoring CO_2 concentrations [6]. It was proposed that a stripping mechanism in which the standing vortices on the leeward side of the stack transport the fuel out of the combustion zone and cause intermittent stripping of unburned gasses is responsible for the observed inefficiencies [7, 9]. Johnson and Kostiuk used the same methodology for measuring combustion efficiency and tested different fuel types, burner stack sizes and wind conditions, and proposed an empirical model for combustion efficiency as a function of fuel jet velocity and diameter, fuel gas heating value, and wind speed [10]. Majeski et al. studied propane flame lengths of four different burners 10.8-33.3mm diameter in cross flow and reported a trend of first increasing then decreasing flame lengths with increasing cross flow velocity, and larger flame lengths in larger diameter burners [11]. Even though flame visual characteristics for flares in cross-wind have been studied, there is little knowledge about that of assisted flares and the impact of co-flowing assist on flame lengths and their visual characteristics.

The first studies to investigate the performance of flares were those implemented by sponsorship of the United States Environmental Protection Agency (EPA) in the 80s. First in the series was a study on the efficiency of full-scale commercial air-assisted (with outflow surface areas of 11.2- and 5.3-in^2) and steam-assisted (27-in^2) flares over a wide range of conditions with different propylene and nitrogen mixtures as fuel by sampling the combustion products through a sample probe held by a crane above the flame. It was found that flare combustion efficiencies (CE), defined as the percentage of CO_2 in all carbon-containing species found in the extracted samples, was 98% or higher, even for highly sooting flames, unless excessive steam assist was used, causing steam-quenching of the flame, or the fuel velocity was increased too much especially for fuels with low heating values. Due to a lack of "isokinetic extraction" and the inability to account for plume dilution, however, the study failed to report soot emissions. Also for air-assisted flares, only qualitative measures of off, low and high were reported for assist flow due to the exact flow rates being "proprietary" [3].

In another study sponsored by EPA, a facility was built in a box canyon (for protection against wind) and pilot-scale and small commercial flares (3-, 6-, and 12-in diameter) were tested with propane and nitrogen mixtures as fuel. Plume dilution was accounted for by mapping concentration measurements to those theoretically measured in the combustion zone through comparing CO_2 measurements in the background and in the plume, and the measurements were used to calculate flare efficiencies. Combustion efficiency was found to be mainly contingent on flame stability which guarantied efficiencies above 98%, as opposed to flare head size or smoking, since in the smoky flares, soot accounted for less than 0.5% of total unburned hydrocarbons. Empirical plots were provided to characterize regions of flame stability as a function of fuel heating value and exit velocity. Even though the contribution of soot to combustion efficiency was deemed insignificant, no emission measurement was reported for soot and it was only noted that steam assists as low as 0.5 pound per pound of fuel would sufficiently suppress this soot [4]. Strosher studied various lab-, pilot-, and full-scale flares in oil well sites in Alberta over a span of five years, and reported combustion efficiencies of over 98% for lab- and pilot-scale flares, but 62-82% for oilfield flares. However, plume dilution was not considered and efficiencies were calculated from direct ratio of local CO_2 and all carbon-containing compounds measured using gas chromatography identifying up to 119 volatile compounds in the plume. Due to the limitations imposed by the methodology, the study failed to report emission factors per unit fuel and only as-measured concentrations of the compounds in ppm were reported. Soot and particulate matter were also not reported [8].

The issue of mass balance closure for open-atmospheric plumes seems to have been somewhat of a nuisance in the literature since calculation of combustion products-dependent parameters such as emission factors and efficiencies from ambient-diluted plume measurements requires exact knowledge of dilution ratio. Pohl, et al. used a "dilution factor" concept, defined based on the ratio of measured concentrations and

"theoretical stoichiometric" concentrations in the plume which implicitly assumes complete combustion [4]. Strosher found combustion efficiencies from the ratio of single-point concentration of CO_2 and other carbon-containing compounds, assuming a homogeneous plume, neglecting background CO_2 concentrations [8]. A series of field study campaign on full scale industrial air- and steam-assisted flares sponsored by the Texas Commission on Environmental Quality (TCEQ), took on a different approach by measuring species concentrations continuously over a period of several minutes, and plotting all measured concentrations against one of the species (usually CO). The slope of the linear correlation for all samples at all times (representative of different instantaneous dilution ratios over time) found between each of the species and CO, as the chosen reference species, yields a mass balance closure and enables calculation of reliable combustion efficiencies and emission factors for pollutants. [17]. This method, however, requires real-time, in-situ continuous measurement of species which needs a mobile gas analysing station equipped with a variety of sensing equipment with multiple technologies such as continuous flame ionization detector (e.g. for hydrocarbons), non-dispersive infrared absorbance (for CO_2), chemical ionization mass spectrometry, gas chromatography, etc., which could be prohibitive in terms of cost and availability [19]. The results of this campaign showed that steam-assisted flares are above 95% efficient with steam assist to fuel gas mass flow ratios below 0.5, and combustion efficiencies of air-assisted flares were reported 90% or higher at stoichiometric air mass ratios below 18 and dropped at higher steam or air assist rates [22, 24]. They also reported NO_x emission factors of $0.009 - 0.033$ and $0.044 - 0.083 \frac{lb}{10^6 BTU}$ for steam-, and air-assisted flares, respectively, but BC emissions were reported only as a ratio over CO_2 emissions not as standardized emission factors [23, 16]. The same approach was applied to remote sensing of flare plumes about $400 - 800m$ downstream of the stack and combustion efficiencies as low as 64% for an over-assisted flare with visible steam and as high as 87-99% for other flares were reported. Additionally, an unlit

air-assisted flare venting unburned fuel gas was observed, which was determined as a potential case for over-assisting with air [26]. The expressions developed by Johnson, et al. addressed the closure problem and provided a methodology to calculate plume parameters directly from plume species concentrations considering background ambient species as well as particulate matter concentrations so long as the fuel gas composition and flow rate are known and the plume can be assumed to be homogeneous, or the whole plume can be captured and mixed for sampling [30]. They also showed Strosher's approach to yield combustion efficiency systematic errors as high as 15% for incomplete combustion products (which partly explains the unexpectedly high inefficiencies reported by Strosher [8]), but other aforementioned techniques were shown to have less than 3% error regardless of dilution ratio or combustion efficiency [30]. This approach has been adopted in multiple studies ([36, 48, 37, 35]) and was used for this thesis as well.

More recent studies sponsored by the Natural Sciences and Engineering Research Council of Canada (NSERC) have investigated emissions and efficiencies of assisted flares with an emphasis on their association with assist flow ratios. Ahsan, et al. studied efficiency and emission indices of a 1" tube-in-tube lab-scale steam- and air-assisted flare for two fuel types (methane and propane) and found the flares to be 96% or higher efficient at assist to fuel mass flow ratios (MFR) below 3.5 (steam) and 15 (air) for methane, and 2.2 (steam) and 5.2 (air) for propane flames. They reported emission indices in the range of 0.001-0.1 (methane) and 0.001-3 g/kgFuel (propane) for BC, and 0.1-1 g/kgFuel for NOx. Even though the effect of burner geometry was explored through using two different sizes of the inner tube, where the assist medium was injected, geometric similarity was not maintained since the outer tube size was kept constant [36, 37, 35].

1.2 Research Objectives

Multiple efforts have been made to study the efficiency and performance of flares in both lab or industrial settings. However, there are key knowledge gaps in understanding flame visual characteristics of assisted flares and their potential interplay with emissions. Industrial guidelines, though provide estimates of flame stability zones and recommendations for controlling smoke through assisting, lack estimations of flame geometry for assisted flares. Additionally, previous studies have left out a systematic study of effects of fuel heating value and burner size on emissions and flame shape. Therefore, as a part of the NSERC FlareNet strategic network, research was conducted with the following objectives:

- Design and build two geometrically similar tube-in-tube burners as lab-scale air-assisted flares
- Develop hardware and software needed for a process to quantify the visual attributes of flames using digital photography and automate the process through devising a reliably repeatable image processing tool to characterize flame shapes through instantaneous photographs
- Use the existing diagnostic apparatus to quantify emissions of BC and NO_x under different conditions by systematically changing fuel heating value, fuel flow rate and burner size and investigate the impact of injecting different quantities of air assist on the measured parameters
- Investigate the impact of air assist on flame shape characteristic and emissions and inspect the potential interplay of the two within the range where the flame stability is not compromised

In the following chapters of this thesis, a detailed description of the experimental setup and diagnostic tools for emission measurement and image processing will be

outlined and the background theory will be presented in chapter 2. An explanatory discussion of the results for emissions as well as shape characteristics of the studied air-assisted flare flames will be presented in chapter 3. Finally concluding remarks and a summary of the key findings along with recommendations for future studies will be provided in chapter 4.

Chapter 2

Experimental Setup and methodology

The following sections will describe the experimental setup, including the material and equipment used, the diagnostic tools used for acquiring the data. Also described are the techniques that were adopted for processing the data, as well as the theoretical methodology and equations used for calculating emissions, flame characteristics, and other parameters that will be discussed in chapter 3 of this thesis.

2.1 Experimental setup

In order to study a co-axial, air-assist, jet diffusion flame, a burner, connected to flow regulated gas lines to supply the fuel and air, was placed underneath an exhaust hood is shown schematically in Figure 2.1.

Compressed liquefied propane of 99.5% purity was the reducing agent in the fuel stream. To investigate fuel composition effects in terms of either volume- or mass-based heating value on the flame outcomes, carbon dioxide was chosen as a fuel-diluent and tests were done at different levels of dilution, as well as pure fuel. (In this thesis the mixture of the reducing agent and the diluent will be referred to as the fuel stream.) Carbon dioxide (CO_2 44.01 g/mol)was specifically chosen as the diluent due to its virtually identical molar mass to propane (C_3H_8 44.1 g/mol) in order to avoid changing the burner exit hydrodynamics that would occur with a diluent of a different

density, and thereby using CO_2 keeps the focus on the impact on the flame region chemistry and thermodynamics. Air was used as assist medium, which was supplied through a building pressurized air system. All gas flows were separately controlled using calibrated Alicat mass flow controllers of different maximum flow rates (Alicat, MCR 50 slpm and 1000 slpm), and based on the required flow rates for the test conditions. The propane and carbon dioxide were fully mixed in a length of tubing following a tee-connection after their mass flow controllers and before entering the burner.

The burner was comprised of a concentric tube-in-tube assembly which created two exit ports: one for assist flow and the other for the fuel. The fuel flowed through the annular region between the two tubes, while the assist flowed out of the inner tube. Two burners that were essentially geometrically identical were constructed where the diameters of inner and outer tubes of the larger burner were twice that of the smaller burner. The large burner henceforth referred to as *"2-inch burner"* consisted of stainless steel tubes of 2" and 1" outer diameters, respectively, and the smaller burner which will be referred to as *"1-inch burner"*, measured half these values. Detailed dimensions corresponding to the two burners are outlined in Table 2.1. From the ratio of diameters, the rms (root mean square) from the mean of these ratios is 0.013, or 0.6% deviation in geometric scaling.

Inner and outer tubes ended at the burner rim at the same vertical location, and the inner tube was ensured to be centered using three set-screws positioned 120 degrees apart midway up the length of the outer tube, and centricity was verified by visual inspection. In order to avoid non-fully developed flow effects in the 2" burner given its small length to diameter ratio (L/D) for the outer tube, flow straightening was adopted. The annular space above the inlet tee was filled with 1 mm glass beads for a length of 20 mm as shown in Figure 2.2. The beads were kept in place using stainless steel wire mesh cloths of 0.14 mm and 0.76 mm opening size (30% and 36%

		2" burner	1" burner	Ratio of 2" to 1" burner
Outer tube	Outer diameter mm (in)	50.80 (2.00)	25.40 (1.00)	2.00
	Inner diameter mm (in)	44.70 (1.76)	22.90 (0.90)	1.95
Inner tube	Outer diameter mm (in)	25.40 (1.00)	12.70 (0.50)	2.00
	Inner diameter mm (in)	22.86 (0.90)	11.30 (0.45)	2.02
Length (Inlet to outlet port)	Inner tube mm (in)	520.0 (20.5)	495.0 (19.5)	-
	Outer tube mm (in)	245.0 (9.7)	360.0 (14.2)	-

Table 2.1: Measured dimensions of the 2" and 1" burners

open area respectively) used on top of each other below and above the area filled with beads. These mesh cloths were cut into annular disks matching the shape of the flow area.

The plume of combustion products from the flame, as illustrated in Figure 2.1, was captured fully through an over-hanging exhaust hood with a square opening measuring 90 cm on each side. This capture hood was connected to a duct of 30 cm diameter. The flow rate of this duct could be regulated using a Venturi air control valve and was set at 17 m^3/min in order to ensure that the flow within the duct was fully turbulent for mixing purposes (Re $\approx$ 70000). The area surrounding the burner was somewhat isolated from the rest of the room by glare-resistant vinyl curtains (not shown in Figure 2.1) approximately 3 m in height and enclosing a rectangular area 2 meters away from the exhaust hood on all sides. However, air flow in and out of the enclosed area was not fully isolated given that the curtains were 5 cm above the floor from the bottom and approximately 2 m below the ceiling from the top. This arrangement allowed a net flow of air into the burner area while isolating the flame from random perturbations in the room air movement. In order to provide a proper

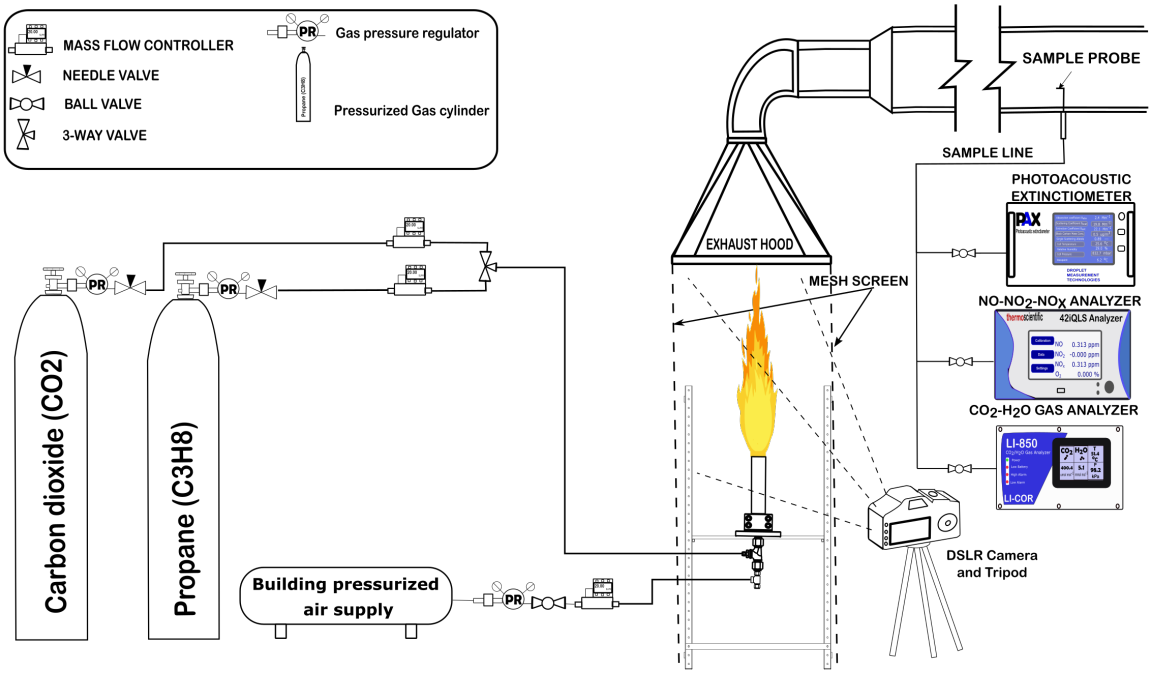

Figure 2.1: Schematic of the experimental setup and diagnostic equipment.

background for imaging, a black vinyl-covered flame resistant curtain was hung on the side of the hood opposing the camera. In order to further minimize perturbations, two fire-resistant mesh screens were also used on the two lateral sides of the exhaust hood.

Samples for emission diagnosis were extracted using a sampling probe inserted into the exhaust duct 6 m downstream of the exhaust hood. Samples taken using this probe have been previously shown to be radially homogeneous. [37]. The probe was then connected through a 1.59 cm OD copper tube to a union cross, which was connected to the set of diagnostic gas analysis equipment using flexible plastic tubing. The union connecting each piece of equipment to the sampling probe had a separate valve for each of the ports.

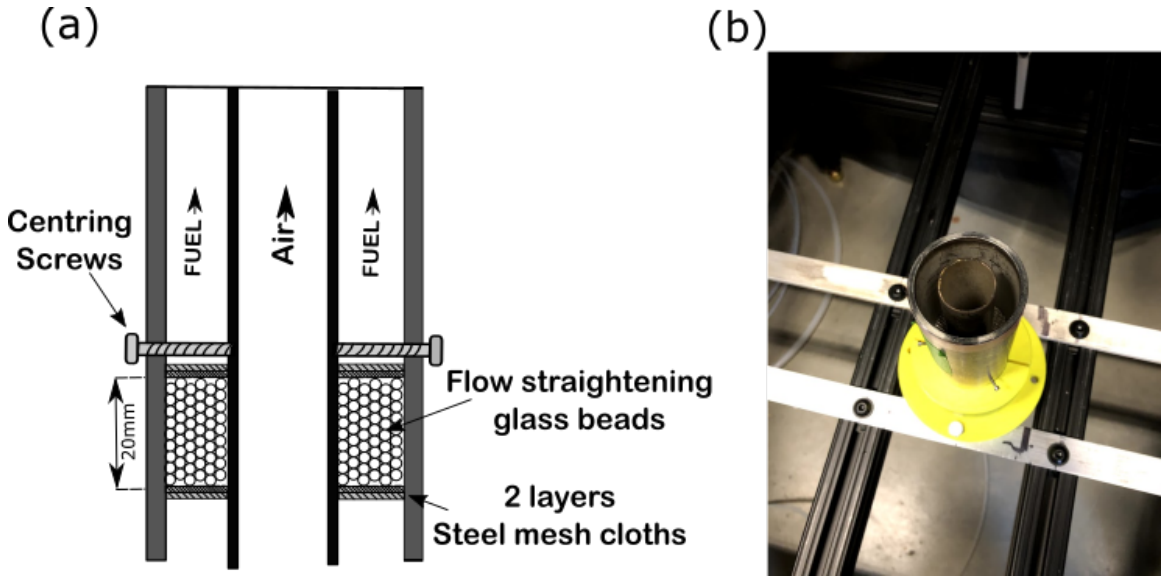

Figure 2.2: a) Schematic of the burner exit port. Glass beads and steel mesh cloths were used in the 2" burner for flow straightening. b) View of the 2" burner mounted on the frame

2.2 Diagnostic equipment

The emission diagnostic equipment set consisted of a photo-acoustic extinctiometer (Droplet Measurement Technologies, PAX) for measuring black carbon (BC) concentrations, which was connected to the union port using a conductive rubber tube so as to minimise particle deposition, a NO_x analyser (Thermo Scientific, 42iQLS), and a CO_2 gas analyser (LI-COR, LI850). These devices, as well as flow controllers described earlier (Alicat, MCR 50 slpm and 1000 slpm), were connected using serial ports to a desktop computer running LabView software in order to record the emission along with the flow rate setting on the computer following the procedure outlined in section 2.3.

For imaging, a digital DSLR camera was used (Nikon D5300 equipped with AF-S DX Nikkor 18-55 mm lens), which was mounted on a tripod approximately 1.5 m away from the burner. A standard measuring tape was used as a scale reference in order to find the pixel-to-length factor for each set of images taken for any particular

camera and burner position configuration.

2.3 Data acquisition procedure

A testing matrix was designed based on varying the parameters of the "Base Case", defined as the case with the 2" burner, pure propane as fuel (no dilution) with a flow rate of 20 SLPM. For each case, data points where chosen by incrementally increasing air assist flow rate from zero to either near the point of collapse or the facility's capacity to supply pressurized air, whichever was smaller. The size of the air assist increments was determined intuitively based on the observations of emission or flame shape in real time, i.e. the increments were chosen to be smaller when any specific trend was observed, and larger when changes were observed to be less significant. At each set point for the fuel and assist flow rates, $\sim$180 pictures were captured using the continuous shutter mode on the camera, which based on shutter speed and other settings would would yield an imaging frequency of about 2-4 frames per second (fps), depending on exposure and other imaging parameters. The shutter speed was adjusted based on an initial sampling of images in order to achieve as clear photos as possible. Usually a shutter speed of 1/1000 s was used but this was occasionally increased or reduced for significantly brighter or darker flames, respectively, and aperture was set automatically by the camera. After waiting an approximate 3 minutes for concentration readings on the gas analyzers to reach steady state, they were recorded for a period of 1 minute with 1 Hz frequency, before moving on to the next assist flow rate setting.

2.4 Data processing techniques

Data derived from experiments comprised of two kinds: emissions and images data, and each will be discussed in the following subsections

2.4.1 Emission data

Species concentrations including NO, NO_2, NOx, CO_2, and black carbon were downloaded from the data acquisition station computer for analysis. Data for each case was initially inspected and possible outliers (e.g., unexpected zeros resulting from digital communication glitches, etc.) were excluded and averages were taken over the recorded data to give a representative concentration value for the given case. Concentration values were then used for emission index calculations, which will be outlined below.

Emission indices derivation

The methodology used here to calculate emission indices was based on a steady state carbon balance analysis written for a control volume (CV) enclosing the region above the burner, where fuel and assist gases exiting the burner and ambient air flow into the CV and the plume is the outlet flow of the CV. This methodology was developed by [30] , where the full derivation can be found. For the purposes of this work, it was assumed that a combustion efficiency of approximately 100% was achieved. This assumption is consistent with previous studies done using the same experimental setup, where it has been shown that as long as recorded CO_2 concentrations do not drop significantly with increasing the assist flow rate, calculated combustion efficiencies remain above 98%, past which point they immediately "collapse" [37]. This was the case for all the conditions studied here, and it was verified that CO_2 concentrations remain consistent within 5% over the ranges tested for air assist flow rates.

Starting with a carbon mass-balance for the described control volume, and knowing the composition of the fuel gas, as well as relevant species concentrations in the ambient air, the flow rate of the plume captured by the exhaust hood can be calculated without the need for any further information about the amount of air entrained

by the plume. Then, as a result the flow rates of other species of interest can be found by using the plume flow rate and their corresponding measured concentrations. The equation derived based on the assumption of having CO_2 as the only carbon-containing product of combustion [30] in the plume was used to calculate the plume gas molar flow rate:

$$\dot{n}_{plume,100\%} = \frac{x(X_{C_xH_y,FG})\dot{n}_{FG} + (X_{CO_2,FG})\dot{n}_{FG} - (X_{CO_2,\infty})\frac{M_{FG}}{M_\infty}\dot{n}_{FG}}{X_{CO_2,plume} - X_{CO_2,\infty}} \tag{2.1}$$

where x is the number of carbons per molecule of the hydrocarbon fuel (e.g. $x = 3$ for propane C_3H_8), X_i is the mole fraction of species i which can be assumed to be identical to volume fractions readings in ppm given the ideal gas assumption, FG refers to the fuel gas comprising of hydrocarbon and non-reacting diluents, $X_{CO_2,FG}$ indicates mole fraction of CO_2 in the fuel gas stream where there is dilution with CO_2, $X_{CO_2,\infty}$ is mole fraction of CO_2 measured in the ambient, and M_{FG},M_∞ are molecular weights of the fuel gas and ambient air, respectively.

With the plume flow rate now known, specific gaseous species flow rates can be found:

$$\dot{m}_{i,produced} = M_i\left((X_{i,plume} - X_{i,\infty})\dot{n}_{plume,gas} - \left\{X_{i,FG}\frac{\dot{m}_{FG}}{M_{FG}}\right\}_{inert} + X_{i,\infty}\frac{\dot{m}_{FG}}{M_\infty}\right) \tag{2.2}$$

where the molar flow rate found from Equation 2.1 can be substituted for $\dot{n}_{plume,gas}$, and inert constituents of the fuel gas are accounted for in the second term. For black carbon emission rates, assuming that background ambient BC is negligible and since measurements from the PAX are given in mass concentration $\frac{\mu g}{m^3}$ units, and correcting for the fact that the PAX cell is kept at a lower temperature T_{cell} (which is recorded in the output data file along with BC concentrations), the following equation can be

written for produced solid state black carbon mass flow rate:

$$\dot{m}_{BC,produced} = f_{m,measured} \frac{R_u T_{cell}}{P_{plume}} \dot{n}_{plume} \tag{2.3}$$

where $f_{m,measured}$ is the measured mass concentration of BC by PAX, R_u is the universal gas constant and P_{plume} is the absolute pressure of the plume in the duct and was measured using a pressure transducer (Omega, PX409-100AI). Mass flow rate of each species is then divided by the mass flow rate of the fuel gas to find the corresponding emission index (EI), i.e. mass of produced species per unit mass of the fuel gas:

$$EI_i = \frac{\dot{m}_{i,produced}}{\dot{m}_{FG}} \tag{2.4}$$

A thorough error analysis was performed on species emission rates and indices and is presented as error bars in the results section. For each measured parameter, precision (stemming from the variations of the recorded values for the parameter over the course of one minute of data recording) as well as accuracy error due to device bias error, span drift, etc. provided by the manufacturer was considered and their propagation into the derived parameters was then found. For a detailed discussion of error propagation and analysis refer to Appendix A.

2.4.2 Imaging and image processing

Average flame shape analysis, which is one of the main foci of this thesis, was enabled by taking multiple images of a flame and adopting image analysis techniques to quantify characteristic dimensions of the various flames. Images were analysed using a Matlab code developed specifically for the purposes of this study (a copy of the code is provided in Appendix D). For each "batch" of 180 images (images taken of a single flame corresponding to a given set of fuel composition, and fuel and air flow rates),

the user could adjust settings for pre-processing and processing in an interactive user interface, and the processed results could be reviewed in a separate window, where they could be chosen to be saved in a separate file.

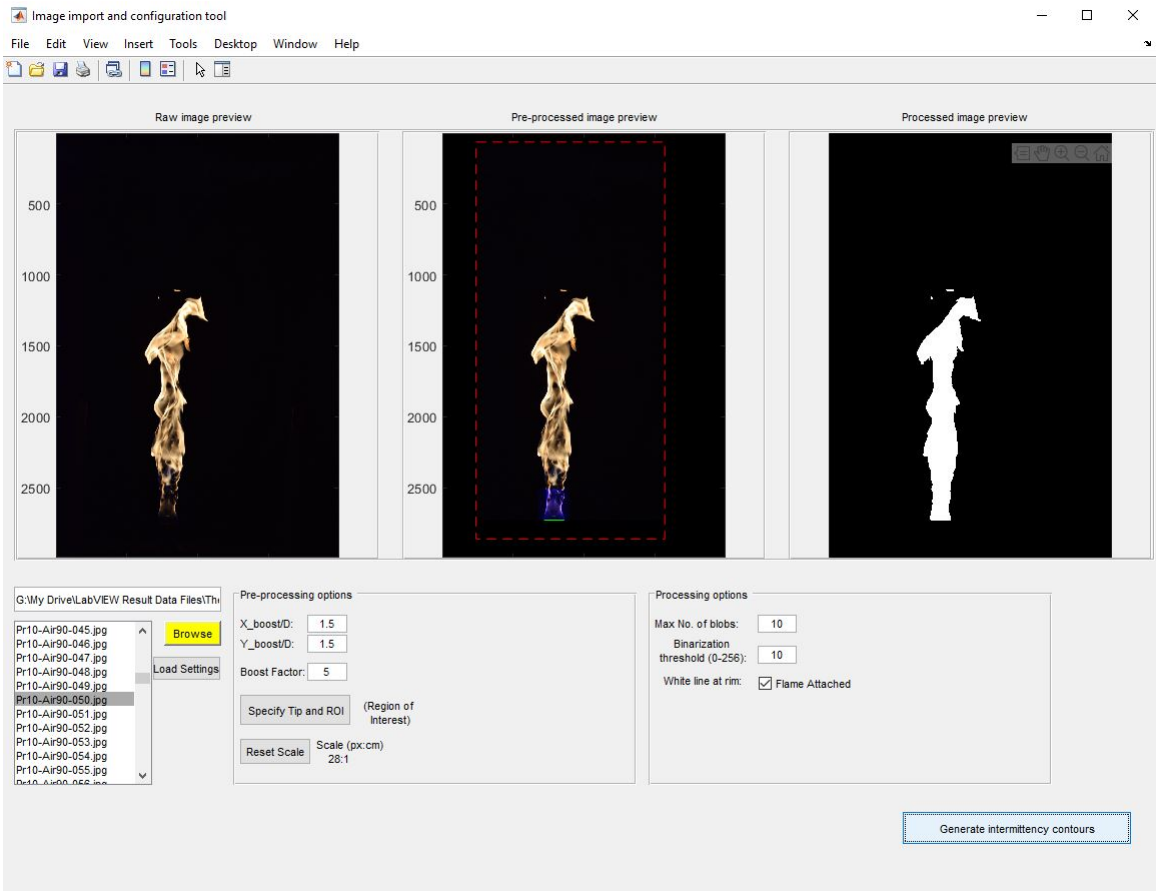

Figure 2.3: User interface of the software, where a preview of raw and processed images is displayed and the processing parameters can be chosen

The Matlab code first converted the RGB pictures into black and white, assigning each pixel an intensity value between 0 and 255. It then binarized each image using a threshold intensity set by the user based on visual intuition, where often a value of 10 was found to best isolate the flame from the surroundings, but slightly smaller or larger values were occasionally used. The optimal value was chosen based on a trial and error approach on sample images in the batch in which increasing the threshold would result in losing large segments of the less bright parts of the flame or

or decreasing it would lead to including the background noise and reflections into the isolated flame. Pixels with intensity values less than the threshold were set to black (i.e., zero for binary images) and pixels with intensities above that value were set to white.

Due to lower luminosity of the flame in the bottom part near the burner tip, using a global threshold was found to be troublesome especially for brighter flames where the bright upper region of the flame would make the less luminous lower part (where soot has yet to develop) appear darker in the image due to the camera's limited dynamic range. For that reason, the user was given the option to "boost" the blue component of the pixels enclosed by a rectangle sitting on the burner rim whose width and height could be customized and often a width- and height-to-diameter (burner's outer diameter as it appears in the picture) ratios of 1-2 and 1-6 were used respectively given that the soot free region of the flame spanned an area within these limits. The region was chosen so that no artificial discontinuity was found in the resulting binarized image in the bottom part of the flame. In order to filter out random noise and make sure that only the visibly significant "blobs" of flame made it to the binarized picture, a MATLAB image processing toolbox function was utilized to keep only the 10 largest blobs of flame in the binarized image. Additionally, pertaining to flame surface continuity assumption, each blob was chosen to be "filled-in" if there were holes left in the flame image due to lighting conditions, etc. After satisfactory results with individual images was observed, the code would stack all the binarized, pre-processed images in the batch on top of each other to generate "intermittency contours" of 10%, 50% and 90%, defined as the pixels which had values equal to 10%, 50% and 90%, respectively, of the total number of images in the batch. For example, a threshold of $0.5 \times 180 = 90$ was used for the 50% intermittency contour of a batch of 180 images.

Finally, to quantify "width" and "height" of the flame an enclosing rectangle was

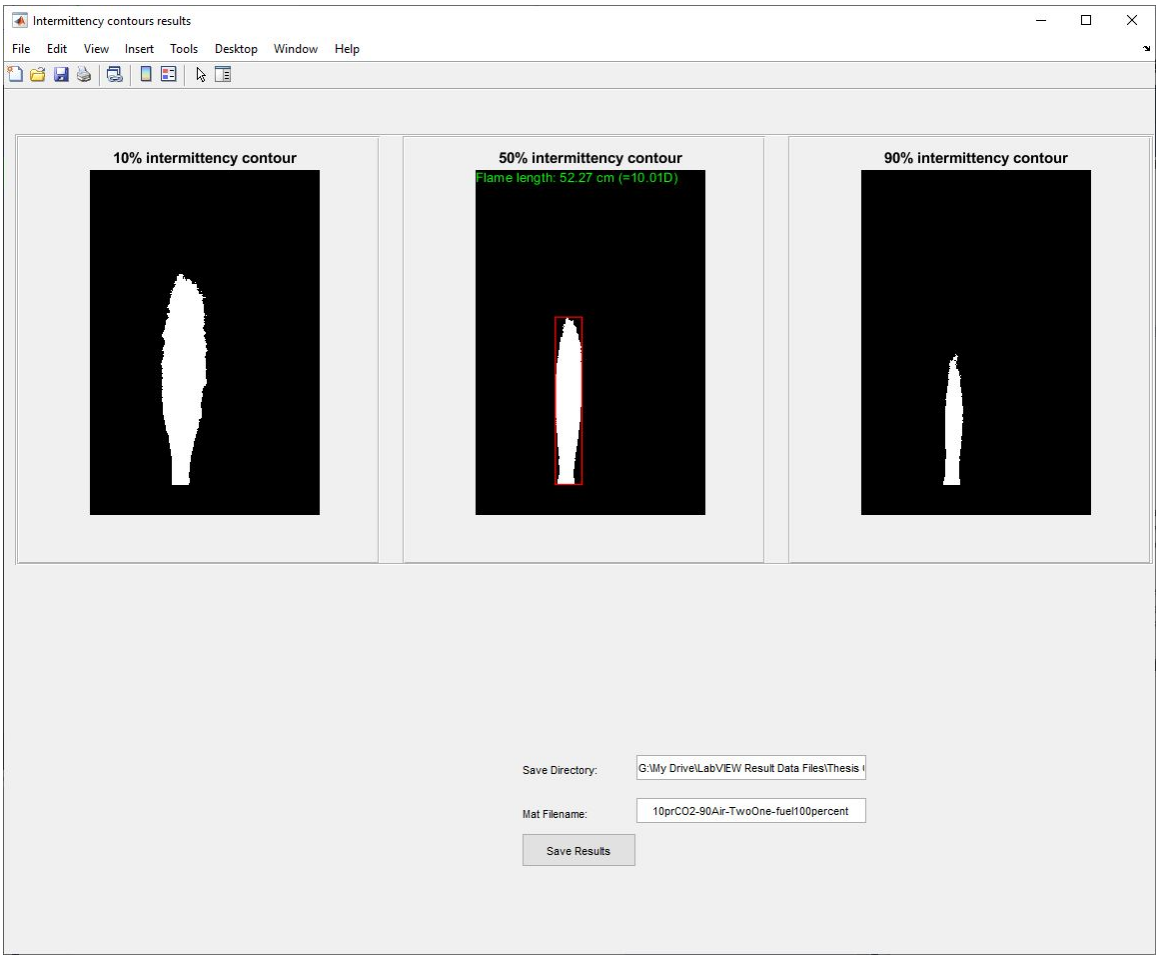

Figure 2.4: The 10, 50 and 90% contours are displayed, and if the results are satisfactory they can be saved

fit to the largest blob in the 50% contour using another pre-defined image processing MATLAB function, height and width of which were attributed to those of the flame. In cases with high assist flow rates where the turbulence induced by the air stream made the flow field and the flame visibly turbulent, a phenomenon was observed where starting from the burner tip, the flame would narrow down to a width smaller than the burner diameter, and then grow wider again. This shape will be referred to as "flame necking" and its location above the burner and width was quantified. The code first "smoothed" the edges of the 50% contour by calculating the 2-D convolution of the image using a 10×10 pixel window. Then starting at the burner tip, horizontal

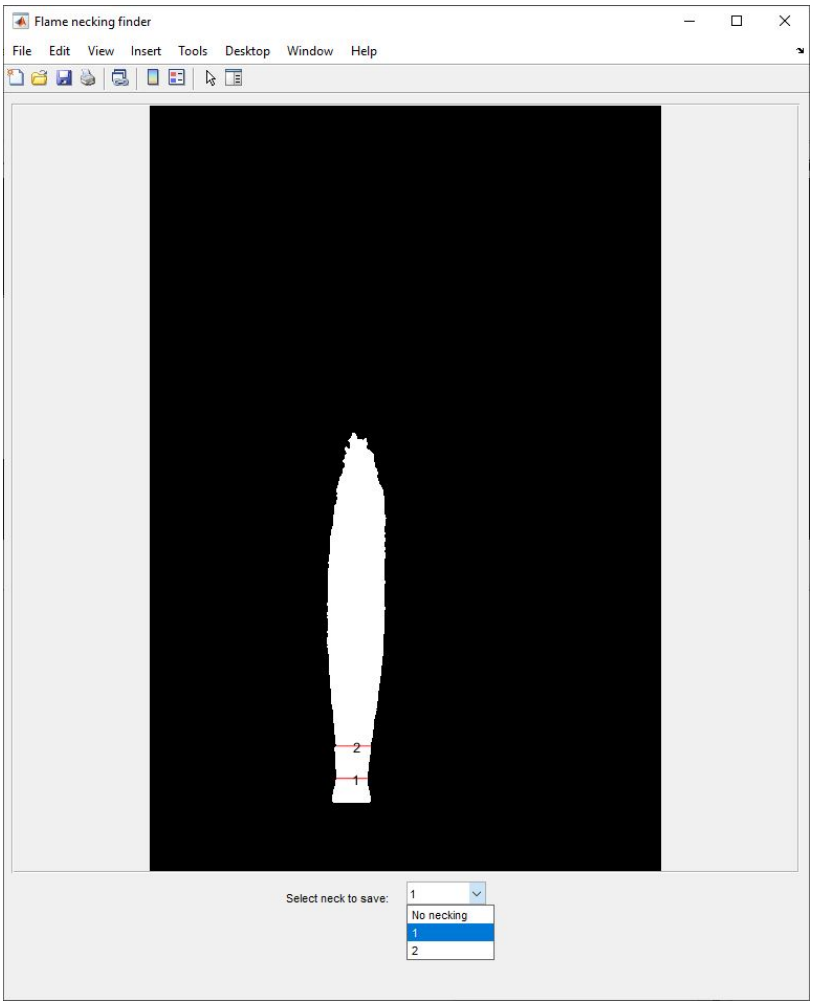

Figure 2.5: Tentative necking locations are marked and the user could decide on the actual location

width of the flame at each vertical location was measured up to 5 diameters above the tip and locations with a width smaller than that below and above them were marked as tentative necking locations, if any meeting these conditions was found. The user was then prompted to choose one (or none) as the actual flame neck based on visual intuition, and the height and width of the neck were saved to the results file along with other parameters of interest. Pixel-based length measurements were converted to physical lengths using an image with a measuring scale for each batch of images (a measuring tape).

Chapter 3

Results and discussion

The case of the 2" burner with a 20SLPM flow of pure propane was chosen as the reference or base case and then the burner, fuel composition and fuel flow rate were changed to compare the ensuing results against this base case. Details of all test cases can be found in Table 3.1. For 1" burner air assist was increased up to the point of flame blowout, while for the 2" burner, flame was stable within the tested air flow range.

In the following sections results will first be presented on the visual appearance of the flame and emission indices and shape parameters for the base case. Special consideration is given to the formation and eventual blowing off of a flame that can occur between the fuel and assist air streams (referred to as the inner flame and is separate from the flame between the fuel and the ambient air). In the subsequent section BC results will be presented and the role of the inner flame is highlighted. This chapter will end with sections on NO_x emissions and the quantification of the size and shape of the visible flame for all tested cases.

Table 3.1: Testing matrix and attributes of the cases. Each row in the table corresponds to a dataset presented in the results and discussion section. Reynolds numbers for air (Re_{air}) and fuel (Re_f) were calculated at room temperature for the flow rates tested.

Case designator	**Fuel stream flow rate**	**Burner**	**Fuel stream composition (%by volume)**	**Assist air flow range**	Re_f	Re_{air}
20prCO2-TwoOne-fuel100percent	20SLPM	2" burner	100% propane 0% CO_2	0∼250SLPM	1334	0∼14028
10prCO2-TwoOne-fuel100percent	10SLPM	2" burner	100% propane 0% CO_2	0∼250SLPM	667	0∼14028
20prCO2-OneHalf-fuel100percent	20SLPM	1" burner	100% propane 0% CO_2	0∼150SLPM	2626	0∼17028
10prCO2-OneHalf-fuel100percent	10SLPM	1" burner	100% propane 0% CO_2	0∼125SLPM	1313	0∼14190
20prCO2-TwoOne-fuel70percent	20SLPM	2" burner	70% propane 30% CO_2	0∼250SLPM	1121	0∼14028
10prCO2-TwoOne-fuel70percent	10SLPM	2" burner	70% propane 30% CO_2	0∼250SLPM	561	0∼14028
20prCO2-TwoOne-fuel50percent	20SLPM	2" burner	50% propane 50% CO_2	0∼250SLPM	996	0∼14028
10prCO2-TwoOne-fuel50percent	10SLPM	2" burner	50% propane 50% CO_2	0∼250SLPM	498	0∼14028
20prCO2-TwoOne-fuel30percent	20SLPM	2" burner	30% propane 70% CO_2	0∼250SLPM	881	0∼14028
10prCO2-TwoOne-fuel30percent	10SLPM	2" burner	30% propane 70% CO_2	0∼250SLPM	441	0∼14028

3.1 Results of Base Case

3.1.1 Visual Appearance of Flame

Before adding any assist, the flame is highly buoyant and radiant, bright orange/yellow in color throughout the length of the flame, and producing significant amounts of soot (Figure 3.2(a)). As the air assist is introduced, an "inner flame" is ignited and stabilized on the rim of the inner tube. A pale outline of the inner flame can be seen in Figure 3.2(b). To better depict the appearance of the inner flame,long exposure pictures (1/20 s rather than the regular 1/1000 s exposure used for other images) of flames with stable inner flame for the case of 10 SLPM pure propane on the 2" burner are shown in Figure 3.1. Long exposure images of inner flames for the 1" burner are also provided in Appendix C section C.1

Once ignited, the inner flame was stable up to the point of inner flame blow-off,

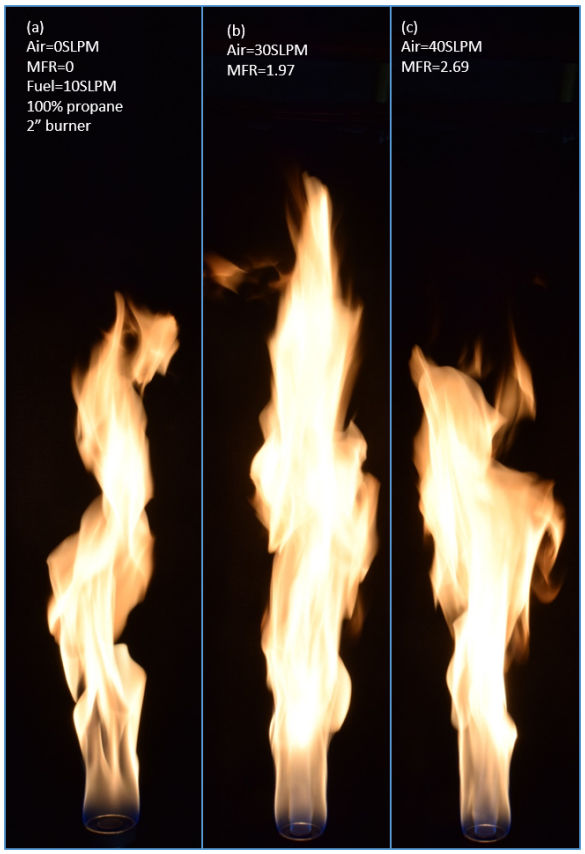

Figure 3.1: Long exposure flame images for 10 SLPM pure propane on 2" burner case before inner flame blow-off. Refer to Appendix C for more select long exposure pictures of flames with an inner flame

when the air flow destabilized the flame and eventually blew it out (Figure 3.2(d)). This secondary flame was less stable than the main flame and might occasionally not self-ignite unless triggered by an external mild perturbation from the room air, and was less stable when the inner tube was still cold, e.g., the flame would sustain better when the inner flame was present for a few minutes and it was harder to get it to reignite by reducing the air flow back down from a flow rate above the blow-off point. As assist rate was progressively increased, the outer flame became less luminous and a blue region began to develop in the lower part of the flame (Figure 3.2(e-g)).

Turbulent eddies began to form in this bottom region of the flame and the flame also became taller. By further increasing the assist flow rate, the blue region grew

Figure 3.2: Instantaneous images of the flame for the base case. A pale radiance of the inner flame attached to the inner tube is visible for MFR=0.99 and 1.31. Assist flow is increased from left to right. The inner flame is blown off at MFR=1.42. For instantaneous images of all other cases refer to Appendix C.

longer and brighter and the turbulent eddies spread across the length of the flame (Figure 3.2(h-i)), making the yellow sooty portion of the flame shorter and less bright, resulting in an overall shortening of the flame. Furthermore, with the development of the turbulent region in the lower part of the flame, a narrowing of the flame was observed in the vicinity of the burner (Figure 3.2(g-i)), causing the flame to narrow down close to the burner exit before widening again to the flame width, which will be referred to as necking. This phenomenon was characterized quantitatively, and the results will be presented later in this chapter. Moreover, diluting the fuel resulted in shorter flames that were less luminous and bluer than the bases case. The effects of dilution and burner size will be further discussed in the subsequent sections. Similar image progressions of all other cases are provided in Appendix C section C.2

3.1.2 Black carbon and NO_x emissions

Black carbon emission results for the base case are illustrated in Figure 3.3(a) and show approximately constant emissions of $0.3 g/kg Fuel$ for assist MFRs up to 1.3, past which point emissions start to go down exponentially by more than 3 orders of magnitude, by the point where assist is increased up to $MFR = 5$.

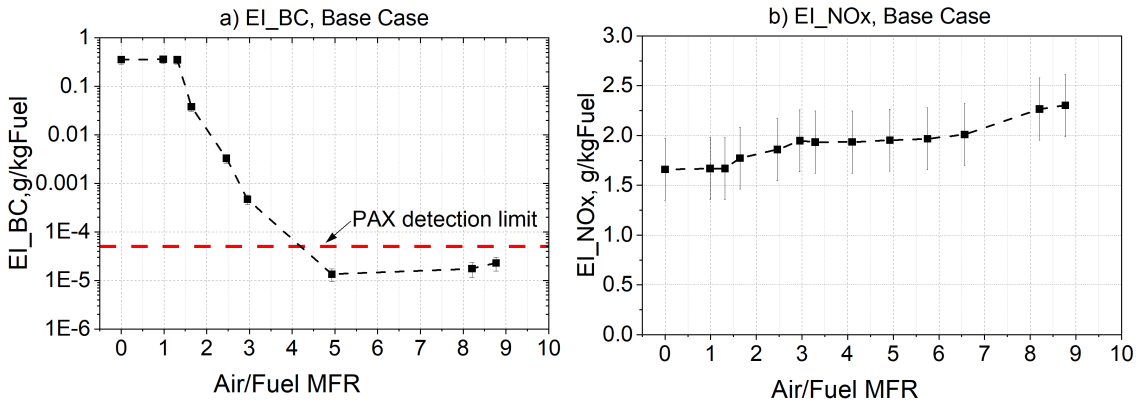

Figure 3.3: Emission results for the base case (20prCO2-TwoOne-fuel100percent). Black carbon emissions are depicted on log scale, PAX detection limit is shown by a red dashed line (a), NO_x emission index is shown on linear scale (b)

Past this point emissions remain the same and essentially fully suppressed, given that the $1.4 \pm 0.3 ppm$ detection limit of PAX (found from BC measurements reading for filtered room air) would give an emission index that amounts to approximately 10^{-4}–10^{-5}g/kgFuel based on the different fuel compositions and flows tested. Therefore, it can be concluded that emission indices below 5×10^{-5} g/kgFuel indicate negligible black carbon emissions, or at least below the amounts detectable by the PAX.

A closer look at the point of the onset of BC suppression reveals an interesting correlation with a secondary flame attached to the rim of the inner tube. For the base case (as well as all the other cases studied), BC emissions did not start to go down significantly until after the inner flame was blown off, i.e., the first point where BC

emission dropped at least an order of magnitude was also the first point past inner flame blow-off. Whether or not the correlation between the inner flame blow-off and soot suppression is a mere coincidence or there is a causative relationship between the two requires in-flame sampling and is beyond the scope of this study and remains to be investigated in a future work focusing on soot emission resulting from these inner flames. For now, it is just speculation that the inner flame exists in an overall fuel rich environment and provides a connection to the soot formation and particle growth, and a lack of oxygen to immediately consume this soot.

The NO_x analyser was capable of measuring NO and NO_2 concentrations the sum of which yields NO_x concentrations from which emission indices could be found. As shown in Figure 3.3 (b), by introducing air assist, NO_x emission index remains almost at the same level as the unassisted flame at around 1.7g/kgFuel. As the air flow is increased past the inner-flame blow-out point, NO_x emissions start to rise monotonically and end up at 2.3g/kgFuel at the highest MFR recorded.

3.1.3 Characterization of Flame Size and Shape

Flame images were pre- and post-processed in batches of 180 images to find 10, 50 and 90% intermittency contours, of which 50% contours where used to quantify visual characteristics of the flame, namely flame length, width and necking location. Flame length for the base case increases with the introduction of the assist flow up to a peak 25% longer than the initial length (from 74 cm up to 92 cm) at MFR=3.3, past which point the flame starts to shrink almost down to the initial length at the highest MFR tested (Figure 3.4(a)).

Flame width, however, follows a declining trend picking up after the inner flame blow-out (Figure 3.4(b). Starting at a width of 16 cm, it remains somewhat constant with the addition of air assist and begins to decrease after MFR=1.4 down to a final width of 11 cm. Flame necking begins at around MFR=3 with both height and width

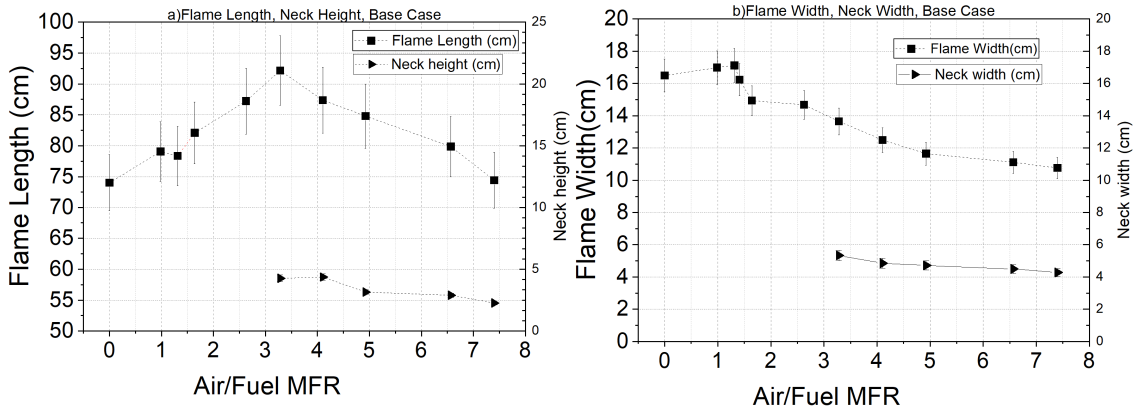

Figure 3.4: Flame size characterization for the base case.

on the same scale as the burner width, 4.3 cm and 5.3 cm, respectively. The neck decreases in height and width with further increasing the assist flow rate down to 2.3 cm ad 4.3 cm, respectively. It is worth noting that the flame length and flame width data has a discontinuity at essentially the same MFR as when the inner flame blows off.

3.2 Emission indices results - all cases

Species concentration measurements from the PAX and NO_x analyser were converted using the methodology detailed in section 2.4 to emission indices for the different cases studied and results were compared to investigate the effect of different control parameters, i.e., burner size, fuel composition and fuel flow on the outcomes.

3.2.1 BC emissions

Referring to Figure 3.5(a and b), different test cases demonstrate a similar trend as the base case of initially constant BC emissions, followed by a transitional phase leading to complete, or nearly complete suppression of black carbon, however initial and final values differ. Reducing the fuel flow rate from 20 SLPM (solid black squares) to 10 SLPM (hollow black squares) increases the pre-suppression BC emission indices

for pure propane by 42%. Similar flow affects are seen for other fuel stream mixtures, for example, pre-suppression BC emissions increase by 69% for the 70% propane fuel, and by 180% for the 30% propane fuel case when fuel flow rate is decreased from 20 to 10 SLPM, while for the 50% diluted case there is the anomalous result of a 36% reduction.

Lower flow rates of the fuel also require higher assist MFR to trigger BC suppression when compared with the higher fuel flow rate of the same fuel composition for all dilution levels. Suppression onset occurs at relatively close MFRs for different dilution levels of the same fuel flow rates (Figure 3.5(c)), however increasing dilution reduces the suppression onset MFR by a small amount, a trend which is consistent for all dilution levels among the same fuel flow rates. Transitional BC suppression region spans a wider range for fuels with higher mole fractions of propane compared with more diluted ones, however BC emissions have gone down by at least three orders of magnitude or levels below detectable limits by the point where assist MFR is increased to 7 across all the cases with 2" burner. The reason that the plots for cases with 20 SLPM fuel flow rate end at MFRs almost half of those with 10 SLPM is that the building air supply capacity was no more than 250 SLPM for all cases, which yields twice the MFR for 10 SLPM compared with 20 SLPM, which also implies that the flames for all cases tested on the 2" burner were stable up to the highest tested assist flow rates. On the contrary, both inner and main flame became unstable at lower MFRs for the 1" burner and the main flame blow-off was found to be within the ranges tested(Figure 3.5(d)). For both the fuel flows of pure propane tested on the 1" burner, BC suppression (coincident with inner-flow blow-off) was initiated at approximately MFR=0.3 and the main flame became unstable at MFR=4.1 and 8.2 for 20 SLPM and 10 SLPM fuel flow rates, respectively.

A potential reason for the generally lower BC emissions for higher flow rates of the fuel is that these streams have greater momentum to more readily mix in more

ambient air, which is seen as a mechanism to reduce BC emissions.

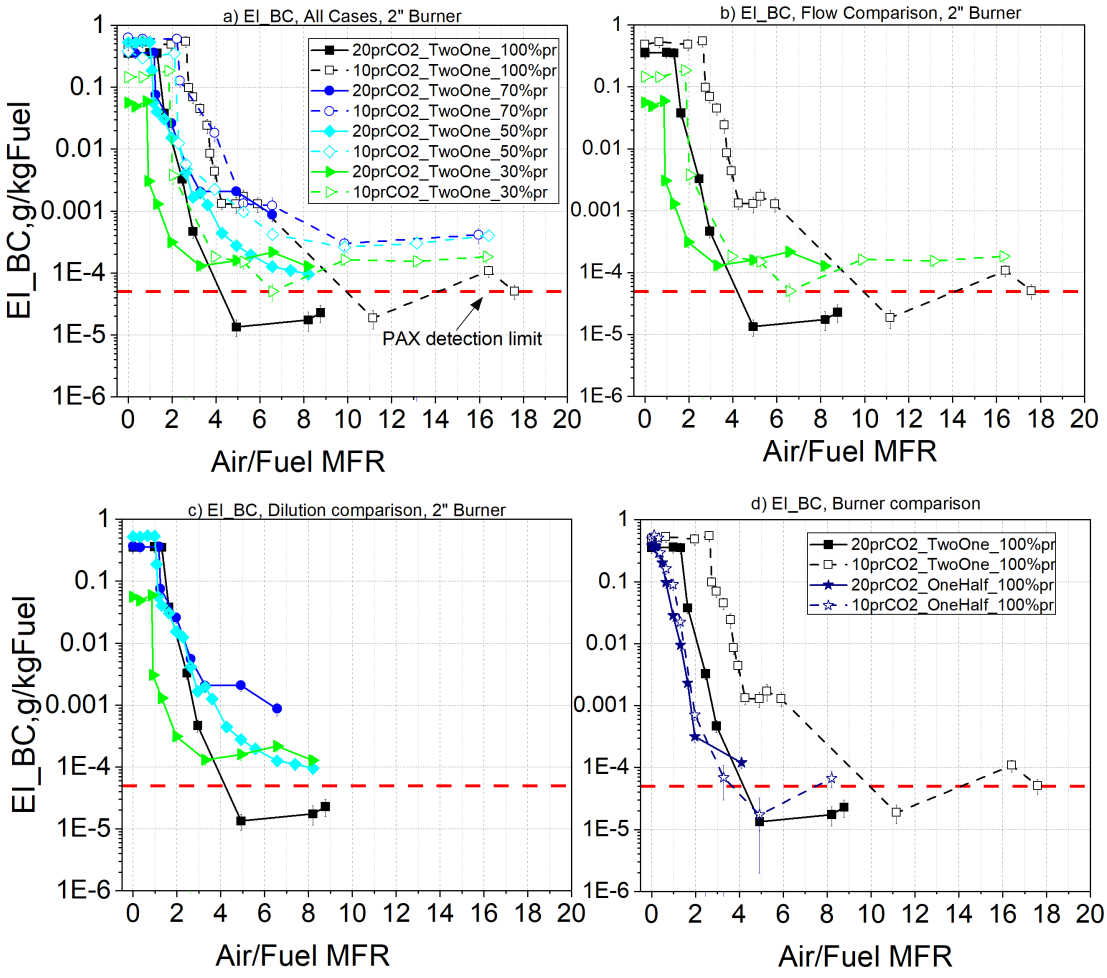

Figure 3.5: Black carbon emission indices on log scale. Emission indices remain constant with increasing assist flow until they start to be suppressed by multiple orders of magnitude. Fuel flow rates of 20SLPM are depicted by solid and 10 by hollow markers. Black color corresponds to pure propane and blue, cyan and green show increasing levels of dilution(a, b, and c). The two cases for 1" burner are marked by navy blue stars (d). Detection limit of PAX is marked by red dashed lines. Refer to section B.1 for full-size plots

3.2.2 NO_x emissions

Increasing dilution of the fuel results in a consistent reduction of NO_x, as shown in Figure 3.6. The diluted fuel containing 30% propane produces 0.59 while pure

propane produces 1.66 g/kgFuel NO_x for 20 SLPM of fuel on the 2" burner.

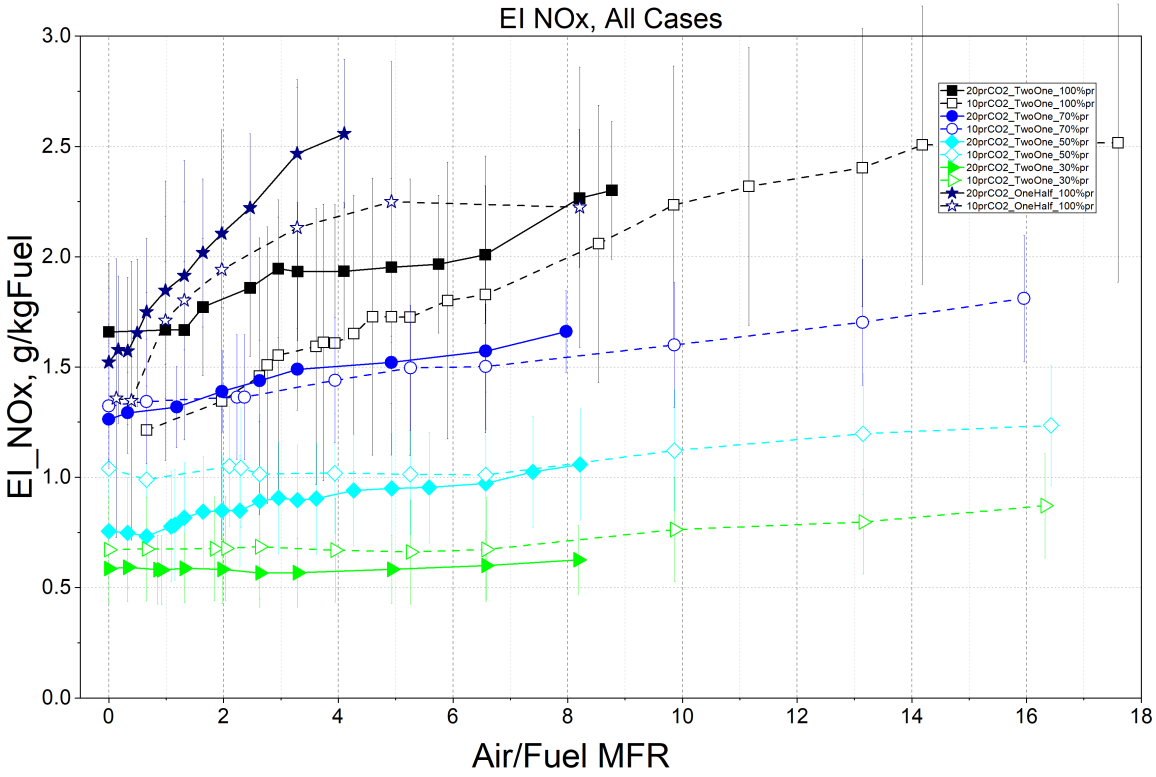

Figure 3.6: *NOx* emission indices for all cases. Emissions go down with increasing dilution levels and go up with increasing assist MFR

Reducing the fuel flow rate from 20 to 10 SLPM reduces NO_x emission indices for pure and 70% propane fuels, but has the opposite effect for 50% and 30% fuels. However, for all fuel compositions, emission indices for the two fuel flow rates are within each other's error bars. NO_x production levels go up with increasing assist flow rate consistently for all dilution levels and fuel flow rates, however, the increase is more significant for less diluted fuels. For instance EI increases by 39% for 20 SLPM pure propane with the 2" burner at the highest assist MFR tested, while it only increases 9% for the 30% propane fuel. The 1" burner, however, demonstrates a steeper increase (68% for 20 SLPM fuel flow rate case) in NO_x emission index in spite of the narrower range of flame stability compared with the 2" burner, even

though they start at relatively close initial EIs.

3.3 Characterization of Flame Size and Shape - all cases

A similar trend to that of the base case is observed for the diluted fuels with high fuel flow rate, however the increase from no-assist flame length at peak value is smaller for 50% and 30% propane fuels at 13% and 10%, respectively (compared with the 25% increase for the pure propane flame). Additionally, the MFR at which maximum length is observed to shift to the left as fuel dilution is increased, however, flame length shrinks at a steeper rate past the peak point for the more diluted fuels (Figure 3.7(c)). In contrast, the 10 SLPM fuel cases demonstrate an almost constant flame length before starting to shrink at an intermediate assist flow of approximately MFR=5 for all fuel compositions. Furthermore, lower fuel flow rate flames are shorter in general than the high flow rate ones and the no-assist flame for low fuel flow is 7-11% shorter than the high fuel flow for all fuel compositions (Figure 3.7(a and b)).

Unlike the 2" burner, both fuel flow rates tested on the 1" burner demonstrate a significant peak in flame length before starting to shrink at approximately MFR=2 (Figure 3.7(d)). The peak flame length for both flows on the 1" burner is approximately 20% longer than the initial flame length. Consistent with the 2" burner, flames from lower fuel flow rate shown by hollow markers are shorter than high fuel flow rate ones and the low fuel flow initial flame is 19% shorter than the high fuel flow non-assisted flame.

Flame width on the other hand follows a more consistent declining trend where in all cases flame width reduces with increasing air assist MFR. The rate of decline is slower at $MFR < 2$ (Figure 3.8(a and c)) but then picks up at higher MFRs. Even though the initial no-assist flame width is smaller for low fuel flow compared with the high fuel flow cases of most fuels, they both follow approximately the same trend

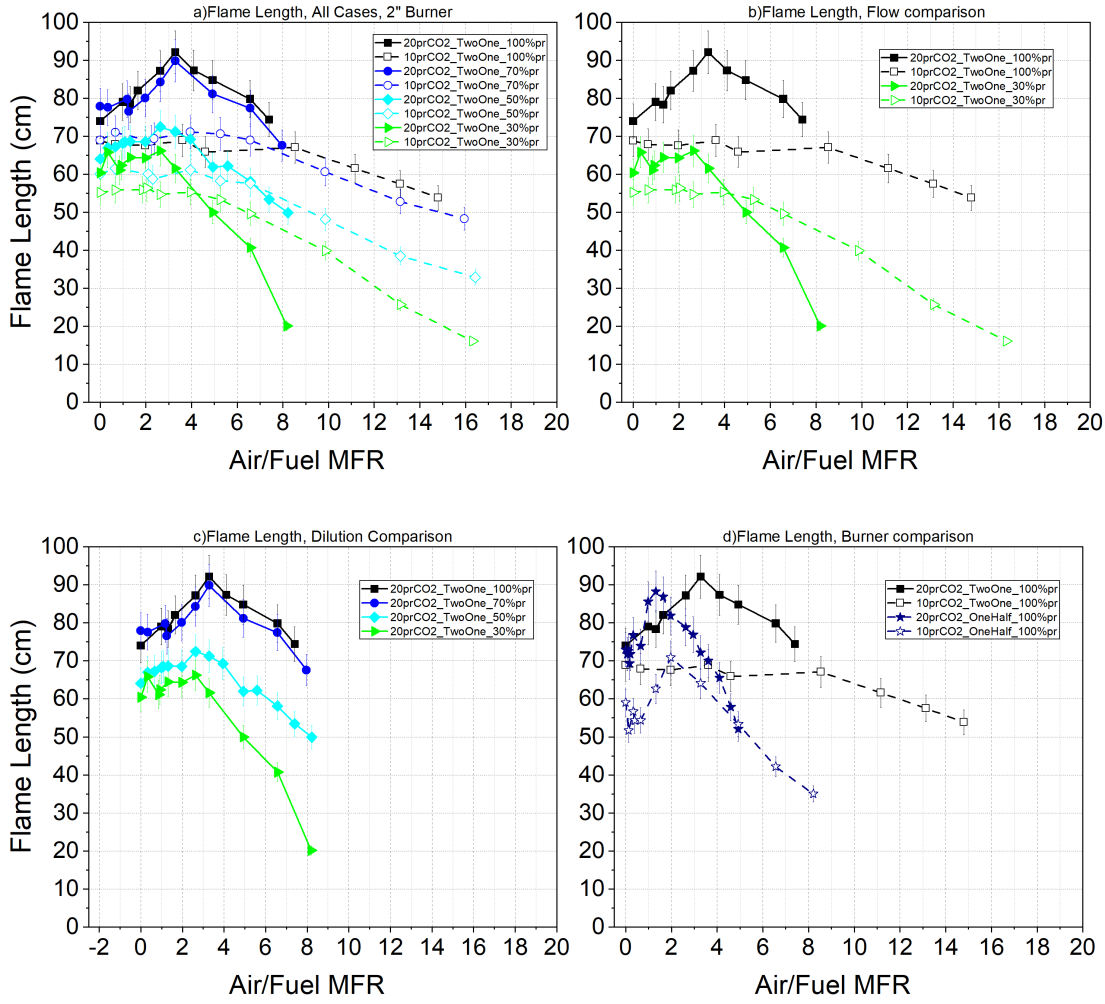

Figure 3.7: Flame length variations with air assist flow. For high fuel flow rates, flame length peaks at some intermediate MFR before starting to drop(c) while it remains constant up to a point before starting to shrink for low fuel flow rate cases (a, and b). Refer to section B.2 for full-size plots

and remain within one another's error bars (Figure 3.8(a and b)). Fuel flow rate, however, has a more significant impact on the 1" burner flames where low fuel flow rate flames start at 40% narrower than high fuel flow rate and remain narrower at higher MFRs. However, width reduces at a steeper rate for the high fuel flow rate case (Figure 3.8(d)). There is also a downward trend in flame width with fuel dilution, with the flame of the most diluted fuel 23% narrower than pure propane flame at no assist condition. This gap in width is maintained at higher assist MFRs for all

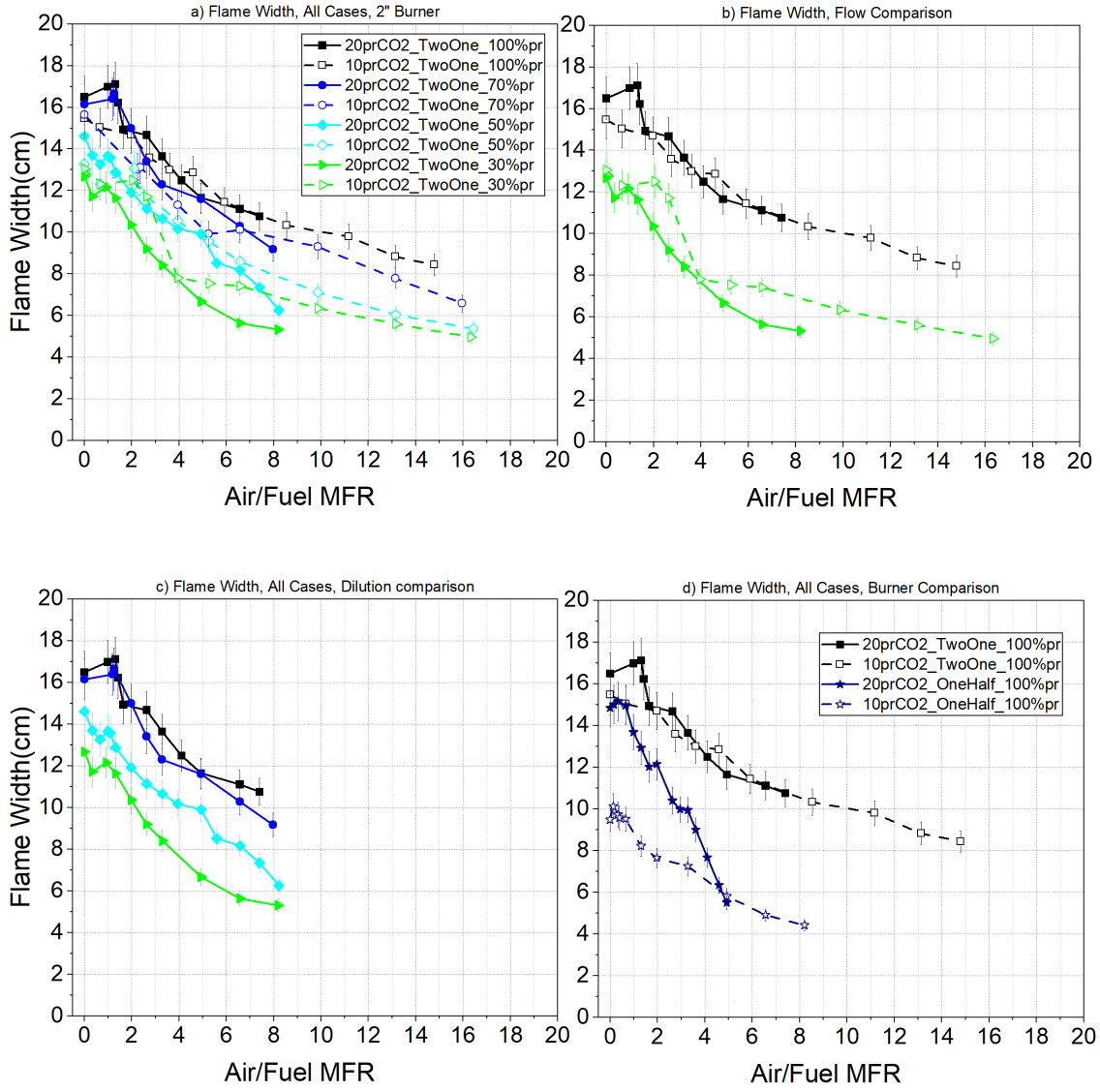

Figure 3.8: Flame width variations with air assist flow show a decreasing trend with air assist MFR. Refer to section B.3 for full-size plots

dilution levels (Figure 3.8,(c)).

As discussed earlier, with the presence of increased turbulence ensuing from the air flow leaving the burner, flame shape was characterised with a narrowing region immediately above the burner. Once established, this constriction termed as "neck" persisted and narrowed in width and lowered in the height it stood above the burner with further increasing assist MFR (Figure 3.9(a and b)). All cases followed a gen-

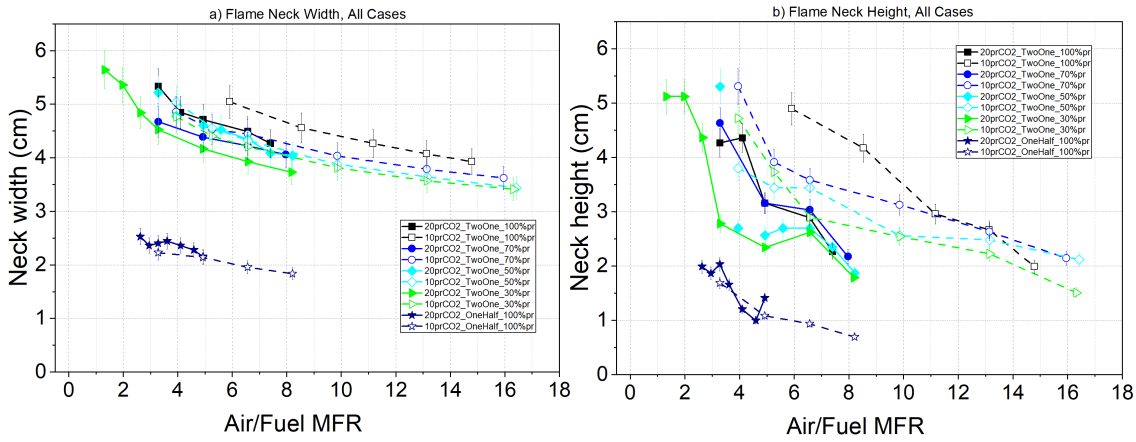

Figure 3.9: Flame neck height above burner (a) and width (b) variations with air assist flow. For all cases it was observed that the neck location lowered down closer to the burner exit and became narrower in width with increasing air assist MFR.

erally identical downward trend in both neck height above the burner and width, however, lower fuel flow rate shifted neck width and height variations with respect to assist MFR slightly to the right, and increasing dilution shifted them to the left. Burner size, on the other hand, had the most profound effect on necking and both height and width were observed to decrease down to 50% of their value for the same fuel and MFR in 2" burner.

3.4 Investigating normalized BC emission factors and potential correlations in emission and flame shape

Given the importance of BC emissions and the main purpose of assist being BC suppression, an attempt was made to investigate the suppression patterns across all the different studied case. As noted earlier, BC suppression takes place at relatively low MFRs, and remains virtually suppressed with further increasing assist. To bring the focus on suppression patterns as opposed to absolute emission values, emission indices were normalized for each case by the emission factor for that case when no assist was used, EI_0 (Figure 3.10, (a)). To provide insight into emissions at lower MFRs, the

normalized emissions were plotted against air mixture mass fraction, defined as the ratio of mass flow rate of air assist (A) over total mass flow rate of air plus fuel (A+F) (Figure 3.10, (b)). This helped group each of the two fuel flow rates closer together, low fuel flow cases represented by dashed lines and high fuel flows by solid lines. However discrepancies among different fuel dilutions can be observed. To account for the buoyancy effects of heat release rate variations due to fuel dilution, mixture fraction was multiplied by a dilution term $\frac{1}{X}$, where X is defined as volumetric fraction of propane in fuel, and an emperical X exponent of 0.2 was found to best group all fuel dilutions together. As shown in Figure 3.10, (c), BC suppression begins as a dilution-corrected assist mixture fraction of approximately 0.55 for high fuel flow rates, and 0.75 for low fuel flow rate cases. The two fuel flow rates and the 1" burner remain separate from the groupings and further treatment is needed to address their effects.

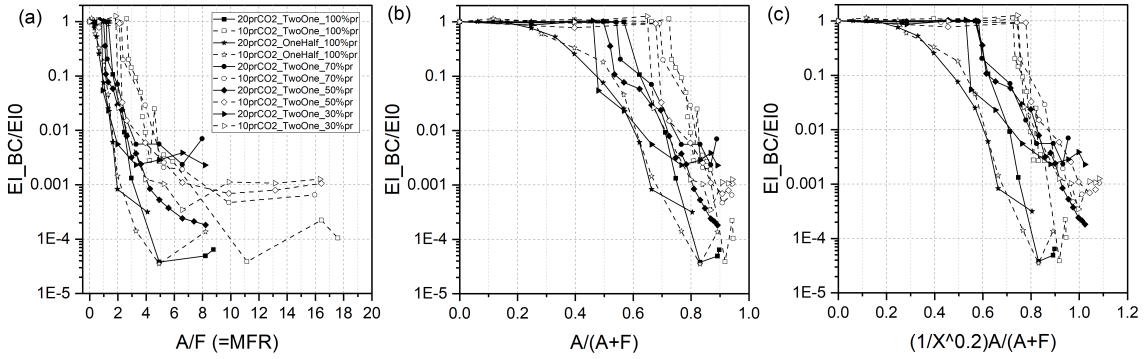

Figure 3.10: BC emission indices normalized by EI_0, i.e. EI_{BC} of the respective case at zero air assist, plotted against MFR (a), air assist mixture mass fraction (b), and dilution-corrected air assist mixture fraction (c). High fuel flow rate cases are shown by solid lines and markers. Low fuel low rate cases are represented by dashed lines and hollow markers

Of particular interest to this study was to investigate the correlation between flame visual and emission characteristics. Results reveal that as inner flame blows off and BC suppression begins, flame width becomes narrower at a higher rate than

before the suppression onset (Figure 3.11). A similar trend is observed for NO_x emissions where emissions pick up after this point. As discussed previously, in high fuel flow rate cases, flame length peaks before starting to reduce. This peak coincides approximately with BC emission indices suppressed by at least 3 orders of magnitude smaller than the initial emissions around $MFR = 3$ for both the fuel compositions depicted in Figure 3.11. For both fuel compositions necking begins at approximately the point where flame length decay starts. In comparison, in the low fuel flow rate

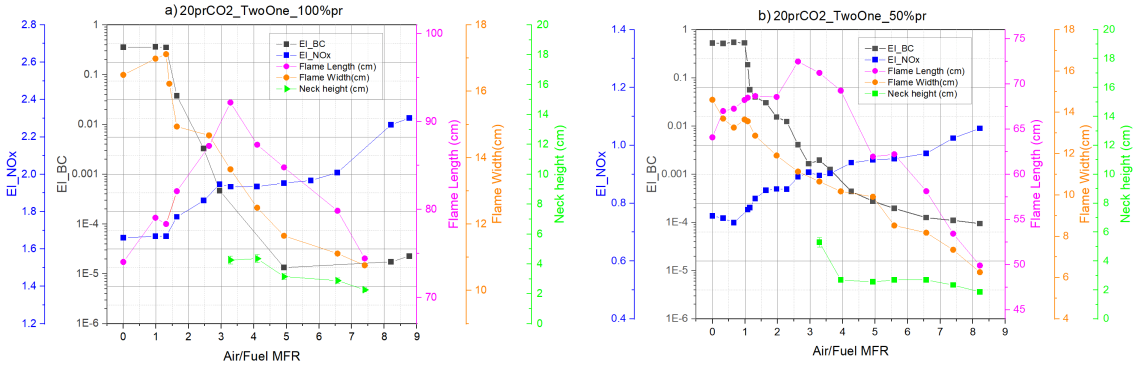

Figure 3.11: Flame visual and emission characteristics for 20SLPM fuel flow rate of pure propane (a) and 50% diluted propane (b) on 2" burner

cases, flame length did not increase before starting to decay but rather remained constant and by the point where decay started, BC was already suppressed by at least 3 orders of magnitude (Figure 3.12). For both fuels, the first point that necking is identified, approximately MFR=4, also coincides with at least 3 orders of magnitude suppression of BC . A similar trend with high fuel flow rate is observed for low fuel flow cases where after the inner flame is blown off and BC suppression begins, flame width reduces at a higher rate with the increase of assist MFR. Figure 3.12

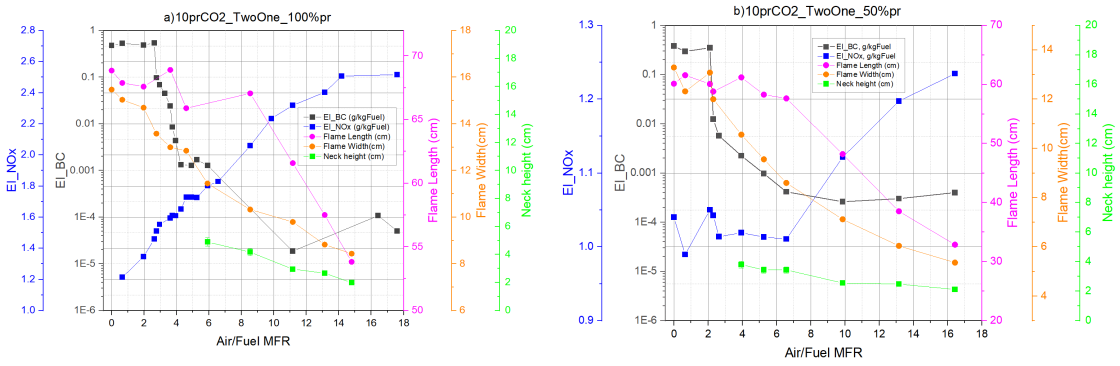

Figure 3.12: Flame visual and emission characteristics for 10SLPM fuel flow rate of pure propane (a) and 50% diluted propane (b) on 2" burner

Chapter 4

Conclusion

Flames from two geometrically similar stainless steel tube-in-tube burners with 1" and 2" outer tube diameters (inner tubes measured half as large as the outer in both burners) were tested in order to study emissions and flame shape characteristics of air-assisted flares. Four different propane-CO_2 mixtures with 1, 0.7, 0.5 and 0.3 propane volumetric mixture fraction were used as fuel at two flow rates of 10 and 20SLPM for the fuel mixture. Air assist stream was delivered through the inner tube while fuel was delivered through the outer tube. Air flow was increased progressively up to the point of flame blow-off (for 1" burner) or up to 225SLPM (2" burner). Through an exhaust hood, the plume was collected and through a probing tube products were directed to the diagnostic suite comprising of PAX (BC concentrations), NOx analyser and LICOR (CO_2 concentrations). Instantaneous photographs of the flame (about 180 of each flame taken at a rate of 3-4Hz) were captured and later processed using an automated software package to extract flame width, length as well as the height above burner and width of the "flame neck" which was observed at elevated assist flow rates. BC and NOx concentration measurements were converted to emission indices (grams of species per kg of fuel) using a carbon-based mass balance.

The case of 20SLPM flow of pure propane as fuel on the 2" burner was used as a reference case and results of other cases were compare against it. Results of the base

case showed that with increasing assist flow mass flow ratio (MFR), BC emission index remained constant at 0.35g/kgFuel up to MFR=1.3, past which BC was suppressed exponentially by several degrees of magnitude, eventually below the detection limits of the measurement device. This point of collapse was observed to be concurrent with the blow-off of a secondary inner flame that was stabilised on the rim of the inner tube and existed in the region inside the main flame. NOx emission index started at 1.7 g/kgFuel was observed to increase progressively up to 2.3 g/kgFuel at the highest tested MFR of 8.8, particularly at a higher rate past the point of inner flame collapse. Flame length followed a trend of first increasing then decreasing, starting at 74.0 cm and a peak of 92.2 cm at MFR=3.3, while flame width (16.5 cm at zero assist) decreased with assist flow after inner flame blow-off. Flame necking was also observed to occur at approximately the same MFR as length peaking. Same patterns were observed for BC and NO_x emissions for the diluted fuels and the reduced fuel flow rate, but diluting the fuel resulted in an overall reduction of both NO_x and BC emissions and reducing the fuel flow rate caused the point of BC suppression onset to increase. Flame lengths also decreased with fuel dilution and the peak was observed to become rounder for more diluted fuels. Also the peaking trend was not observed in low fuel flow cases and flame lengths remained constant before starting to shorten at higher MFRs. Flame widths, similar to the base case, decreased with increasing MFR. The patterns observed for the 1" burner were somewhat different than those for the other burner. The inner flame was blown off at a much smaller MFR of 0.3 and reducing the fuel flow rate did not make a significant change to the BC suppression onset point or emissions. Additionally, the same pattern of peaking before shortening was observed for flame length, however, unlike the 2" burner, reducing fuel flow rate did not change this pattern. When emissions and flame geometry results were considered together, it was revealed that the onset of BC suppression was coincident with an increase in the rate of flame width reduction and NO_x increase, while flame

length started to decay when necking was observed in the vicinity of the burner. In an attempt to normalize the BC emission patterns across all the different cases, a new dilution-corrected air assist mixture mass fraction variable was introduced and an empirical exponent of 0.2 for the dilution term was found to best predict the point of BC suppression onset for different fuel compositions. However, the suggested parameter could not capture the effect of fuel flow rate or burner size.

4.1 Recommendations for future work

One interesting finding of this research was the existence of a secondary inner flame and its apparent correlation with black carbon emission, as the suppression did not begin until after this flame extinguished. It is recommended that this inner flame be more closely studied in a future work through in-flame sampling and to gain insight into whether this flame contributes to the soot formation processes, or its blow-off coinciding with the onset of soot suppression is a mere coincidence. If the former is true, this could have important implications for industrial guidelines regarding operation of air-assisted flares.

Another possible opportunity for a future study is developing a comprehensive model capable of extrapolating flame geometry parameters of air-assisted flares as a function of working parameters such as burner size, fuel type, assist rate, etc. which considers the complicated hydrodynamic and chemical processes related to combustion. Even though effects of varying heating value through dilution were explored here, other hydrocarbons particularly those of higher soot propensity remain to be studied. Additionally investigating the stabilization mechanisms of such flames could provide further insight into the safe operation ranges of assisted flares which could be achieved through burner near-field flow visualization techniques.

Bibliography

[1] T.A. Brzustowski. "Flaring in the energy industry". In: *Progress in Energy and Combustion Science* 2.3 (1976), pp. 129–141. ISSN: 0360-1285. DOI: https://doi.org/10.1016/0360-1285(76)90009-5. URL: https://www.sciencedirect.com/science/article/pii/0360128576900095.

[2] A. O. Isichei and W. W. Sanford. "The effects of waste gas flares on the surrounding vegetation in South Eastern Nigeria". In: *Journal of Applied Ecology* 13.1 (1976).

[3] Marc McDaniel and Bruce A Tichenor. *Flare efficiency study*. Washington, DC, USA, Jan. 1983. URL: https://www3.epa.gov/ttn/chief/ap42/ch13/related/ref_01c13s05_jan1995.pdf.

[4] John H. Pohl et al. "Combustion Efficiency of Flares". In: *Combustion Science and Technology* 50.4-6 (1986), pp. 217–231. DOI: 10.1080/00102208608923934.

[5] J T. Houghton, G J. Jenkins, and J J Ephraums. *Climate Change: The IPCC Scientific Assessment, IPCC First Assessment Report (FAR)*. United Kingdom, Jan. 1990, p. 58. URL: https://archive.ipcc.ch/publications_and_data/publications_ipcc_first_assessment_1990_wg1.shtml.

[6] E. Bourguignon, M.R. Johnson, and L.W. Kostiuk. "The use of a closed-loop wind tunnel for measuring the combustion efficiency of flames in a cross flow".

In: *Combustion and Flame* 119.3 (1999), pp. 319–334. ISSN: 0010-2180. DOI: 10.1016/S0010-2180(99)00068-1.

[7] M.R Johnson and L.W Kostiuk. "Efficiencies of low-momentum jet diffusion flames in crosswinds". In: *Combustion and Flame* 123.1 (2000), pp. 189–200. ISSN: 0010-2180. DOI: 10.1016/S0010-2180(00)00151-6.

[8] Mel T. Strosher. "Characterization of Emissions from Diffusion Flare Systems". In: *Journal of the Air & Waste Management Association* 50.10 (2000), pp. 1723–1733. DOI: 10.1080/10473289.2000.10464218.

[9] M. R. Johnson, D. J. Wilson, and L. W. Kostiuk. "A fuel stripping mechanism for wake-stabilized jet diffusion flames in crossflow". In: *Combustion Science and Technology* 169.1 (2001), pp. 155–174. DOI: 10.1080/00102200108907844.

[10] M.R. Johnson and L.W. Kostiuk. "A parametric model for the efficiency of a flare in crosswind". In: *Proceedings of the Combustion Institute* 29.2 (2002), pp. 1943–1950. ISSN: 1540-7489. DOI: 10.1016/S1540-7489(02)80236-X.

[11] Adrian J. Majeski, David J. Wilson, and Larry W. Kostiuk. "Predicting the length of low-momentum jet diffusion flames in crossflow". In: *Combustion Science and Technology* 176.12 (2004), pp. 2001–2025. DOI: 10.1080/00102200490514769.

[12] David Castiñeira and Thomas F. Edgar. "CFD for Simulation of Steam-Assisted and Air-Assisted Flare Combustion Systems". In: *Energy & Fuels* 20.3 (2006), pp. 1044–1056. DOI: 10.1021/ef050332v.

[13] Christopher D. Elvidge et al. "A Fifteen Year Record of Global Natural Gas Flaring Derived from Satellite Data". In: *Energies* 2.3 (2009), pp. 595–622. ISSN: 1996-1073. DOI: 10.3390/en20300595. URL: https://www.mdpi.com/1996-1073/2/3/595.

[14] P. A. O. Odjugo and E. J. Osemwenkhae. "Natural gas flaring affects microclimate and reduces maize (Zea mays) yield". English. In: *International Journal of Agriculture and Biology* 11.4 (2009), pp. 408–412.

[15] Drew T. Shindell et al. "Improved Attribution of Climate Forcing to Emissions". In: *Science* 326.5953 (2009), pp. 716–718. DOI: 10.1126/science.1174760.

[16] E. C. Fortner et al. "Particulate Emissions Measured During the TCEQ Comprehensive Flare Emission Study". In: *Industrial & Engineering Chemistry Research* 51.39 (2012), pp. 12586–12592. DOI: 10.1021/ie202692y.

[17] Scott C. Herndon et al. "Application of the Carbon Balance Method to Flare Emissions Characteristics". In: *Industrial & Engineering Chemistry Research* 51.39 (2012), pp. 12577–12585. DOI: 10.1021/ie202676b.

[18] O. S. Ismail and G. E. Umukoro. "Global Impact of Gas Flaring". In: *Energy and Power Engineering* 4.4 (2012). DOI: 10.4236/epe.2012.44039.

[19] W. Berk Knighton et al. "Direct measurement of volatile organic compound emissions from industrial flares using real-time online techniques: Proton Transfer Reaction Mass Spectrometry and Tunable Infrared Laser Differential Absorption Spectroscopy". In: *Industrial & Engineering Chemistry Research* 51.39 (2012), pp. 12674–12684. DOI: 10.1021/ie202695v.

[20] *Photoacoustic Extinctiometer (PAX) Operator Manual*. Droplet Measurement Technologies, 2012, p. 64.

[21] Vincent M. Torres, Scott Herndon, and David T. Allen. "Industrial Flare Performance at Low Flow Conditions. 2. Steam- and Air-Assisted Flares". In: *Industrial & Engineering Chemistry Research* 51.39 (2012), pp. 12569–12576. DOI: 10.1021/ie202675f.

[22] Vincent M. Torres, Scott Herndon, and David T. Allen. "Industrial Flare Performance at Low Flow Conditions. 2. Steam- and Air-Assisted Flares". In: *Industrial & Engineering Chemistry Research* 51.39 (2012), pp. 12569–12576. DOI: 10.1021/ie202675f.

[23] Vincent M. Torres et al. "Emissions of Nitrogen Oxides from Flares Operating at Low Flow Conditions". In: *Industrial & Engineering Chemistry Research* 51.39 (2012), pp. 12600–12605. DOI: 10.1021/ie300179x.

[24] Vincent M. Torres et al. "Industrial Flare Performance at Low Flow Conditions. 1. Study Overview". In: *Industrial & Engineering Chemistry Research* 51.39 (2012), pp. 12559–12568. DOI: 10.1021/ie202674t.

[25] EPA United States Environmental Protection Agency. *EPA Enforcement Targets Flaring Efficiency Violations*. 2012. URL: https://www.epa.gov/sites/production/files/documents/flaringviolations.pdf (visited on 04/10/2021).

[26] Ezra C. Wood et al. "Combustion and Destruction/Removal Efficiencies of In-Use Chemical Flares in the Greater Houston Area". In: *Industrial & Engineering Chemistry Research* 51.39 (2012), pp. 12685–12696. DOI: 10.1021/ie202717m.

[27] A. Stohl et al. "Black carbon in the Arctic: the underestimated role of gas flaring and residential combustion emissions". In: *Atmospheric Chemistry and Physics* 13.17 (2013), pp. 8833–8855. DOI: 10.5194/acp-13-8833-2013.

[28] Novakov T. and H. Rosen. "The Black Carbon Story: Early History and New Perspectives". In: *Ambio* 42 (2013), pp. 840–851. DOI: 10.1007/s13280-013-0392-8.

[29] Jr. Charles E. Baukal. *The John Zinc Hamworthy Combustion Handbook, Volume 3 — Applications*. Second. Vol. 3. Taylor Francis Group, 2014.

[30] Darcy J. Corbin and Matthew R. Johnson. "Detailed Expressions and Methodologies for Measuring Flare Combustion Efficiency, Species Emission Rates, and Associated Uncertainties". In: *Industrial & Engineering Chemistry Research* 53.49 (2014), pp. 19359–19369. DOI: 10.1021/ie502914k.

[31] Olusegun G. Fawole, X.-M. Cai, and A.R. MacKenzie. "Gas flaring and resultant air pollution: A review focusing on black carbon". In: *Environmental Pollution* 216 (2016), pp. 182–197. ISSN: 0269-7491. DOI: 10.1016/j.envpol.2016.05.075. URL: https://www.sciencedirect.com/science/article/pii/S0269749116304638.

[32] American Petroleum Institute. *Flare Details for Petroleum, Petrochemical, and Natural Gas Industries , API Standard 537*. Third. Washington, DC, 2017.

[33] *42iQLS Instruction Manual*. English. ThermoFisher Scientific, Sept. 27, 2018.

[34] Øivind Hodnebrog, Stig B. Dalsøren, and Gunnar Myhre. "Lifetimes, direct and indirect radiative forcing, and global warming potentials of ethane (C2H6), propane (C3H8), and butane (C4H10)". In: *Atmospheric Science Letters* 19.2 (2018). DOI: https://doi.org/10.1002/asl.804.

[35] Abbas Ahsan. "Quantifying the Carbon Conversion Efficiency and Emission Indices of a Lab-Scale Steam-Assisted Flare". Master of Science. University of Alberta, 2019. DOI: 10.7939/r3-jtz6-m751.

[36] Abbas Ahsan et al. "Quantifying the carbon conversion efficiency and emission indices of a lab-scale natural gas flare with internal coflows of air or steam". In: *Experimental Thermal and Fluid Science* 103 (2019), pp. 133–142. ISSN: 0894-1777. DOI: 10.1016/j.expthermflusci.2019.01.013. URL: https://www.sciencedirect.com/science/article/pii/S0894177718316558.

[37] Hamza Ahsan. "Experimental Study on the Carbon Conversion Efficiency and Emission Indices of a Lab-Scale Air-Assisted Flare". Master of Science. University of Alberta, 2019. DOI: 10.7939/r3-e04y-tz30.

[38] Daniel H. Chen and Arokiaraj Alphones. "Characterization of the incipient smoke point for steam-/air-assisted and nonassisted flares". In: *Journal of the Air & Waste Management Association* 69.1 (2019), pp. 119–130. DOI: 10.1080/10962247.2018.1525443.

[39] Mohsen Kazemimanesh. "Particulate emissions from flares with entrained droplets". PhD. University of Alberta, 2019, p. 189. DOI: https://doi.org/10.7939/r3-ts57-2c70.

[40] Mohsen Kazemimanesh et al. "Size, effective density, morphology, and nanostructure of soot particles generated from buoyant turbulent diffusion flames". In: *Journal of Aerosol Science* 132 (2019), pp. 22–31. ISSN: 0021-8502. DOI: https://doi.org/10.1016/j.jaerosci.2019.03.005.

[41] Jason Olfert and Steven Rogak. "Universal relations between soot effective density and primary particle size for common combustion sources". In: *Aerosol Science and Technology* 53.5 (2019), pp. 485–492. DOI: 10.1080/02786826.2019.1577949.

[42] Global Gas Flaring Reduction Partnership. *Global Gas Flaring Data*. 2019. URL: https://www.ggfrdata.org/.

[43] *Technical Data for Alicat MC-Series Mass Flow Controllers*. English. 2019. URL: https://documents.alicat.com/specifications/DOC-SPECS-HIGHFLOWCONTROLLERS.pdf (visited on 02/26/2021).

[44] *Global Gas Flaring Tracker Report*. World Bank, July 2020. URL: https://pubdocs.worldbank.org/en/503141595343850009/WB-GGFR-Report-July2020.pdf.

[45] American Petroleum Institute. *Pressure-relieving and Depressuring Systems, API Standard 521*. Seventh. Washington, DC, 2020.

[46] Akash Kumar, Sachin Phadatare, and Pradeep Deore. "A GUIDE ON SMOKELESS FLARING: AIR/STEAM ASSISTED AND HIGH PRESSURE FLARING". In: *International Journal of Engineering Applied Sciences and Technology* 4 (2020), pp. 517–520. URL: http://ijeast.com/papers/517-520,Tesma412,IJEAST.pdf.

[47] EPA United States Environmental Protection Agency. *Code of Federal Regulations (CFR), Title 40 - Protection of Environment, Part 60 - STANDARDS OF PERFORMANCE FOR NEW STATIONARY SOURCES, sub-part §60.18 - General control device and work practice requirements*. 2020. URL: https://www.govinfo.gov/content/pkg/CFR-2020-title40-vol7/pdf/CFR-2020-title40-vol7-part60.pdf (visited on 04/10/2021).

[48] M. Zamani et al. "An experimental study on the carbon conversion efficiency and emission indices of air and steam co-flow diffusion jet flames". In: *Fuel* 287 (2021), p. 119534. ISSN: 0016-2361. DOI: 10.1016/j.fuel.2020.119534. URL: https://www.sciencedirect.com/science/article/pii/S0016236120325308.

Appendix A

Uncertainty analysis

A.1 Methodology

Uncertainty in a measurement can be attributed to either the repeatability of the recorded value, often referred to as precision error, or the systematic uncertainty inherent to the measurement device or technique, often referred to as accuracy or bias.

Precision can be quantified by repeating the same measurement multiple times and use standard deviation and statistical analysis to find uncertainty. For example, for our emission data, device output data was recorded over a duration of 60 seconds producing approximately 60 data points for each experiments, which could be used as the dataset for that specific point. Precision can therefore be found by using the t-score equation:

$$P_x = t\frac{\sigma}{\sqrt{n}} \tag{A.1}$$

, where t is student's t-score evaluated at 2.001 for a sample size of 60 and confidence interval of 95%, n is the sample size and σ is standard deviation found from:

$$\sigma = \sqrt{\frac{(x_i - \bar{x})}{n}} \tag{A.2}$$

, where $\bar{x}$ is the sampled data mean.

On the other hand, accuracy can be found from manufacturer's specifications sheet for each device which is usually provided in the form of a percentage of reading and/or full operation range of the device. Total uncertainty of the parameter can then be calculated from:

$$U_x = \Delta x = \sqrt{P_x^2 + B_x^2} \tag{A.3}$$

, where P_x is the precision uncertainty and B_x is the bias or accuracy uncertainty.

Once the uncertainty for individual measured parameters are known using the aforementioned methodology, their propagation into parameters of interest should be considered. From multivariate calculus for a dependent variable $y = f(x_1, x_2, \dots)$ which is a function of multiple variables $x_1, x_2, \dots$ the uncertainty of y can be written as:

$$\Delta y = \sqrt{(\frac{\partial f}{\partial x_1}\Delta x_1)^2 + (\frac{\partial f}{\partial x_2}\Delta x_2)^2 + \dots} \tag{A.4}$$

, where $\frac{\partial f}{\partial x_i}$ is partial derivative of the function with respect to the i_th variable x_i and Δx_i is the calculated uncertainty for the variable x_i. Alternatively if the function f is of the form $y = x_1^{a_1} x_2^{a_2} \dots$, propagation of error can more conveniently be calculated by first taking log of the function:

$$\ln y = a_1 \ln x_1 + a_2 \ln x_2 + \dots$$

, and then finding error propagation by taking partial derivatives:

$$\left|\frac{\Delta y}{y}\right| = \sqrt{\left(a_1 \frac{\Delta x_1}{x_1}\right)^2 + \left(a_2 \frac{\Delta x_2}{x_2}\right)^2 + \dots} \tag{A.5}$$

A.2 Error propagation for Emission Indices

Given the equations detailed in Appendix section A.1, the methodology can be implemented for each dependent variable and uncertainties can be found. Starting with plume mole flow rate Equation 2.1:

$$\begin{aligned}\dot{n}_{plume,100\%} &= \frac{x(X_{C_xH_{y,FG}})\dot{n}_{FG} + (X_{CO_2,FG})\dot{n}_{FG} - (X_{CO_2,\infty})\frac{M_{FG}}{M_\infty}\dot{n}_{FG}}{X_{CO_2,plume} - X_{CO_2,\infty}} \\ &= \dot{n}_{FG}\frac{x(X_{C_xH_{y,FG}}) + (X_{CO_2,FG}) - (X_{CO_2,\infty})\frac{M_{FG}}{M_\infty}}{X_{CO_2,plume} - X_{CO_2,\infty}}\end{aligned}$$

Neglecting uncertainties in fuel gas composition, we can take partial derivatives to get:

$$\begin{aligned}\delta\dot{n}_{plume,100\%} =& \delta\dot{n}_{FG}\left(\frac{x(X_{C_xH_{y,FG}}) + (X_{CO_2,FG}) - (X_{CO_2,\infty})\frac{M_{FG}}{M_\infty}}{X_{CO_2,plume} - X_{CO_2,\infty}}\right) \\ &+ \dot{n}_{FG}\Bigg[-\delta X_{CO_2,\infty}\frac{\frac{M_{FG}}{M_\infty}}{X_{CO_2,plume} - X_{CO_2,\infty}} \\ &- (\delta X_{CO_2,plume} - \delta X_{CO_2,\infty})\frac{x(X_{C_xH_{y,FG}}) + (X_{CO_2,FG}) - (X_{CO_2,\infty})\frac{M_{FG}}{M_\infty}}{(X_{CO_2,plume} - X_{CO_2,\infty})^2}\Bigg]\end{aligned}$$

, where $\dot{n}_{FG} = \left(\frac{\rho}{MW}\right)_{FG}Q$, and Q is the volumetric flow rate recorded by the mass flow controller. So uncertainty in $\dot{n}_{FG}$ can be found from:

$$\Delta\dot{n}_{FG} = \left(\frac{\rho}{M}\right)_{FG}\Delta Q \tag{A.6}$$

, where ΔQ is the uncertainty in volumetric flow rate readings. Therefore molar flow rate of plume gas can be rewritten as:

$$\begin{aligned}\Delta\dot{n}_{plume,100\%} =& \Bigg\{ (\Delta\dot{n}_{FG})^2 \left(\frac{x(X_{C_xH_{y,FG}}) + (X_{CO_2,FG}) - (X_{CO_2,\infty})\frac{M_{FG}}{M_\infty}}{X_{CO_2,plume} - X_{CO_2,\infty}} \right)^2 \\ &+ (\dot{n}_{FG})^2 \Bigg[(\Delta X_{CO_2,\infty})^2 \left(\frac{\frac{M_{FG}}{M_\infty}}{X_{CO_2,plume} - X_{CO_2,\infty}} \right)^2 \\ &+ \left((\Delta X_{CO_2,plume})^2 + (\Delta X_{CO_2,\infty})^2 \right) \\ &\times \left(\frac{x(X_{C_xH_{y,FG}}) + (X_{CO_2,FG}) - (X_{CO_2,\infty})\frac{M_{FG}}{M_\infty}}{(X_{CO_2,plume} - X_{CO_2,\infty})^2} \right)^2 \Bigg] \Bigg\}^{\frac{1}{2}}\end{aligned} \tag{A.7}$$

, where uncertainty in CO_2 concentration readings from LICOR can be substituted for ΔX_{CO_2}.

With the plume flow rate uncertainty know, uncertainties for species production rates can be calculated from Equation 2.2:

$$\dot{m}_{i,produced} = M_i \left((X_{i,plume} - X_{i,\infty})\dot{n}_{plume,gas} - \left\{ X_{i,FG}\dot{n}_{FG} \right\}_{inert} + X_{i,\infty}\dot{n}_{FG}\frac{M_{FG}}{M_\infty} \right)$$

Taking partial derivatives gives:

$$\begin{aligned}\delta\dot{m}_{i,produced} =& M_i \Bigg(\delta\dot{n}_{plume,gas}(X_{i,plume} - X_{i,\infty}) \\ &+ (\delta X_{i,plume} - \delta X_{i,\infty})\dot{n}_{plume,gas} - \left\{ (\delta X_{i,FG})\dot{n}_{FG} + X_{i,FG}(\delta\dot{n}_{FG}) \right\}_{inert} \\ &+ \left((\delta X_{i,\infty})\dot{n}_{FG} + (\delta\dot{n}_{FG})X_{i,\infty} \right)\frac{M_{FG}}{M_\infty} \Bigg)\end{aligned}$$

, where the term in curly brackets with subscript *inert* applies only when the species i of interest is also present in the fuel as an inert constituent, e.g. when the fuel is diluted with CO_2, otherwise it can be omitted, e.g. when considering NO,NO_2,etc.

Therefore uncertainty can be calculated as:

$$\begin{aligned}\Delta\dot{m}_{i,produced} =& M_i\Bigg\{(\Delta\dot{n}_{plume,gas})^2(X_{i,plume}-X_{i,\infty})^2 \\ &+\Big((\Delta X_{i,plume})^2+(\Delta X_{i,\infty})^2\Big)\dot{n}^2_{plume,gas}-\Big\{(\Delta X_{i,FG})^2\dot{n}^2_{FG}+X^2_{i,FG}(\Delta\dot{n}_{FG})^2\Big\}_{inert} \\ &+\Big((\Delta X_{i,\infty})^2\dot{n}^2_{FG}+(\Delta\dot{n}_{FG})^2X^2_{i,\infty}\Big)\left(\frac{M_{FG}}{M_\infty}\right)^2\Bigg\}^{\frac{1}{2}}\end{aligned} \tag{A.8}$$

, where ΔX_i is the uncertainty in concentration readings for species i And for black carbon production rates from Equation 2.3:

$$\dot{m}_{BC,produced} = f_{m,measured}\frac{R_uT_{cell}}{P_{plume}}\dot{n}_{plume}$$

Using the methodology explained for deriving Equation A.4, uncertainty can be written as:

$$\frac{\Delta\dot{m}_{BC}}{\dot{m}_{BC}} = \sqrt{\left(\frac{\Delta f_m}{f_m}\right)^2+\left(\frac{\Delta T_{cell}}{T_{cell}}\right)^2+\left(\frac{\Delta p_{plume}}{p_{plume}}\right)^2+\left(\frac{\Delta\dot{n}_{plume}}{\dot{n}_{plume}}\right)^2} \tag{A.9}$$

With the uncertainty in mass production rates of all species known, uncertainty in their corresponding emission indices can be found from:

$$\frac{\Delta EI_i}{EI_i} = \sqrt{\left(\frac{\Delta\dot{m}_i}{\dot{m}_i}\right)^2+\left(\frac{\Delta\dot{n}_{FG}}{\dot{n}_{FG}}\right)^2} \tag{A.10}$$

A.3 Emission measurement uncertainty analysis

The prerequisite for utilizing the error propagation equations derived in appendix section A.2, is a knowing the uncertainty in the individual measured parameters. As discussed in appendix section A.1, uncertainty for each parameter can be broken down to precision and accuracy. Precision error for all measured concentrations and flow

rates can be found using Equation A.1, given that 60 data points were recorded for each case. However, accuracy requires device-specific analysis which will be discussed below.

A.3.1 Mass flow controllers

According to the specifications data sheet by Alicat [43], the Mass Flow Controllers (MFC) used, namely 50, 100 and 1000SLPM, have a rated accuracy of 0.8% of reading +0.2% of full range, where full range corresponds to the model used (50, 100 or 1000SLPM).

A.3.2 NOx Analyser

The 42iQlS analyser was reported to have a span drift of 1% [33] of the 5000ppb full scale, which is the full scale that the device was calibrated at. The calibration gas used for calibrating the analyser (consisting of 50ppm high purity NOx diluted down to 5000ppb with air) had a reported traceable uncertainty of 0.7%. Therefore accuracy can be found as 1% full scale $+0.7\%reading$, where full scale is 5000ppb.

A.3.3 PAX Black Carbon measurement

Unlike Nox analyser or LICOR which directly measure species concentrations and the accuracy thereof is reported by the manufacturer, PAX measures black carbon concentration indirectly through measuring absorption coefficient of the sample and then converting it to BC concentration using mass absorption cross section (MAC) of BC. Therefore the uncertainty in absorption coefficient and MAC both need to be quantified in order to find the uncertainty in concentration. From definition:

$$\text{BC Concentration} = \frac{\text{Sample Absorption Coefficient}}{MAC_{BC}} \tag{A.11}$$

According to an analysis performed on the same device, an accuracy error of 9.6% has been reported for absorption coefficient readings from PAX based on repeatability of multiple independent calibration curves acquired over a period of two months [39]. According to the manufacturer, a default MAC value of $4.74 \pm 0.76 m^2/g$ is used by PAX to calculate BC concentrations, based on the 870nm laser beam wavelength. However, it is warned that the actual MAC may vary by up to 50% depending on the extent to which particles are coated [20] and this would lead to unfavourably large error bars. However, a case could be made that BC particulate emissions from burners similar to those used in this study are not significantly coated. A recent study on soot from a variety of common emission sources such as internal combustion engines, burners, revealed that provided soot particles are not coated, effective density of particles would be virtually identical [41]. Additionally, studies on soot particles from different burners under different conditions have shown that effective density of these particles is very similar [40]. Therefore it can be concluded that soot particles measured by PAX are minimally coated and the recommended MAC value can be safely used.

Thus using equations Equation A.4 and Equation A.11, for PAX accuracy we have:

$$\begin{aligned} \frac{\Delta(f_{m,BC})}{f_{m,BC}} &= \sqrt{\left(\frac{\Delta\alpha_{abs}}{\alpha_{abs}}\right)^2 + \left(\frac{\Delta(\text{MAC})}{\text{MAC}}\right)^2} \\ &= \sqrt{(9.6\%)^2 + \left(\frac{0.76}{4.74}\right)^2} \\ &= 18.69\% \end{aligned} \tag{A.12}$$

Appendix B

Full-size plots

B.1 BC emission index plots

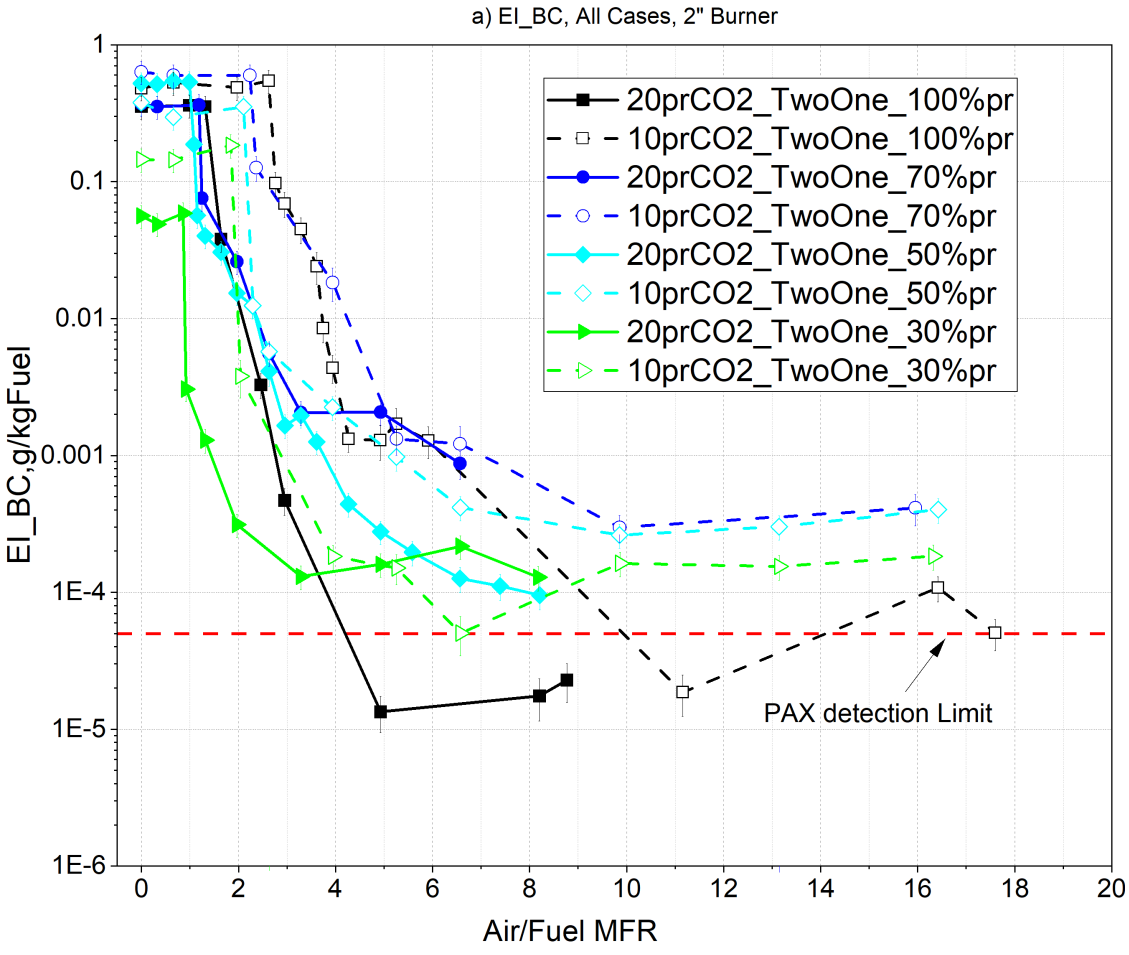

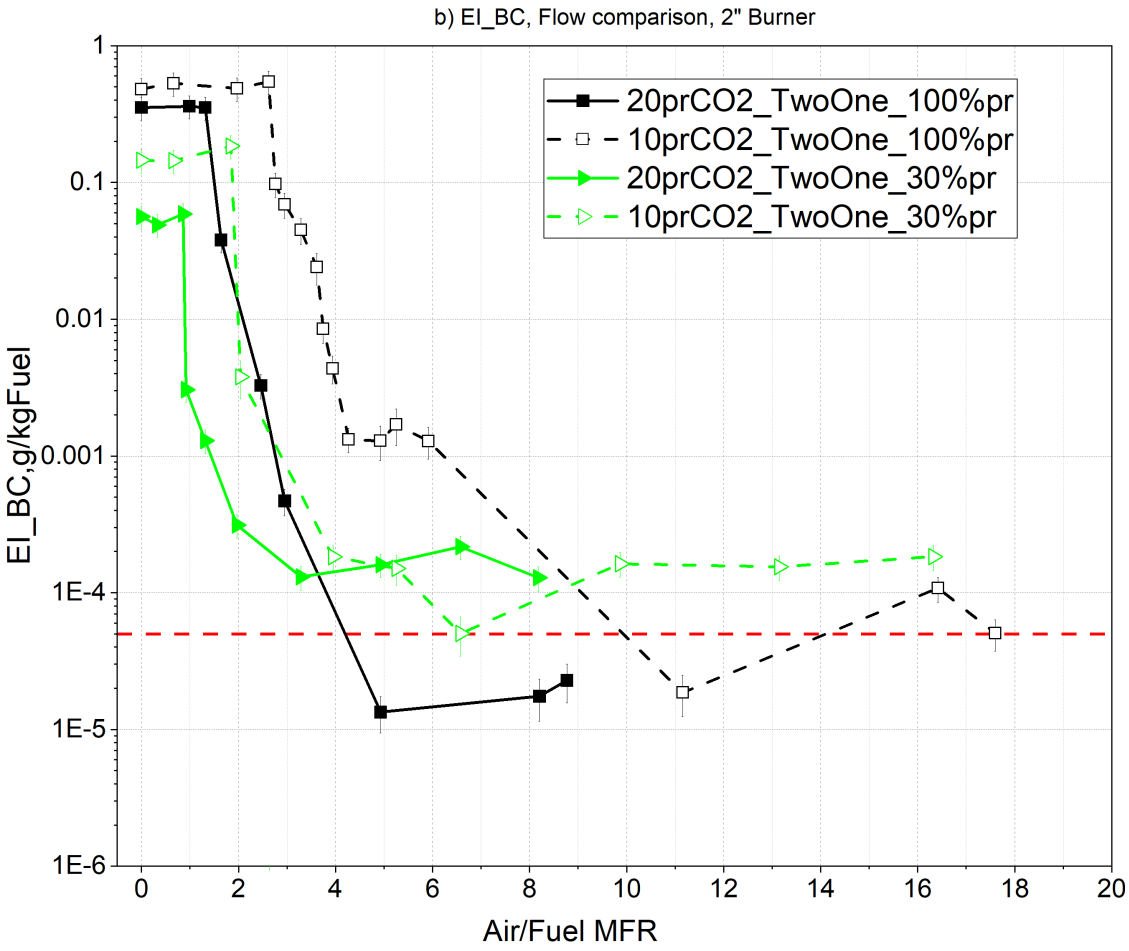
b) EI_BC, Flow comparison, 2" Burner
20prCO2_TwoOne_100%pr
10prCO2_TwoOne_100%pr
20prCO2_TwoOne_30%pr
10prCO2_TwoOne_30%pr
EI_BC,g/kgFuel
Air/Fuel MFR
1
0.1
0.01
0.001
1E-4
1E-5
1E-6
0
2
4
6
8
10
12
14
16
18
20

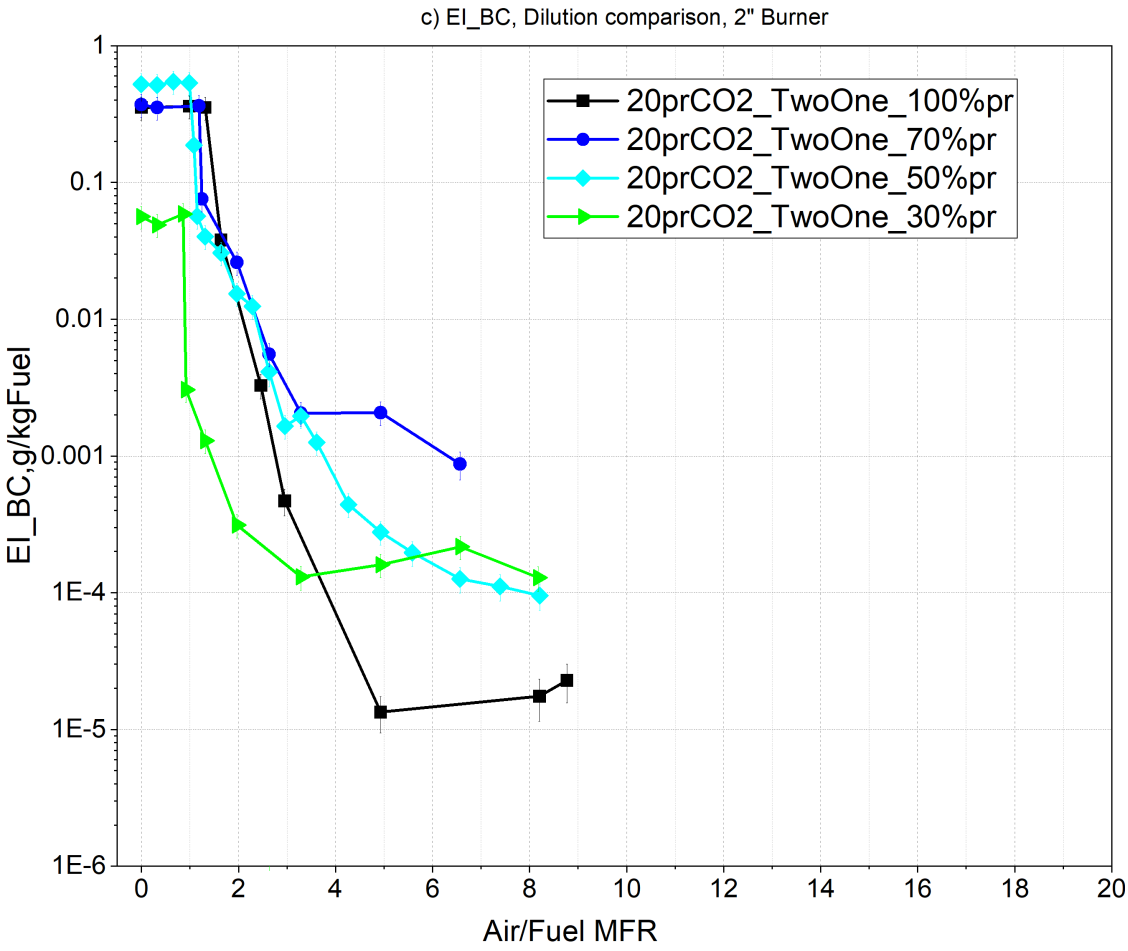
c) EI_BC, Dilution comparison, 2" Burner
20prCO2_TwoOne_100%pr
20prCO2_TwoOne_70%pr
20prCO2_TwoOne_50%pr
20prCO2_TwoOne_30%pr
EI_BC,g/kgFuel
Air/Fuel MFR
1
0.1
0.01
0.001
1E-4
1E-5
1E-6
0
2
4
6
8
10
12
14
16
18
20

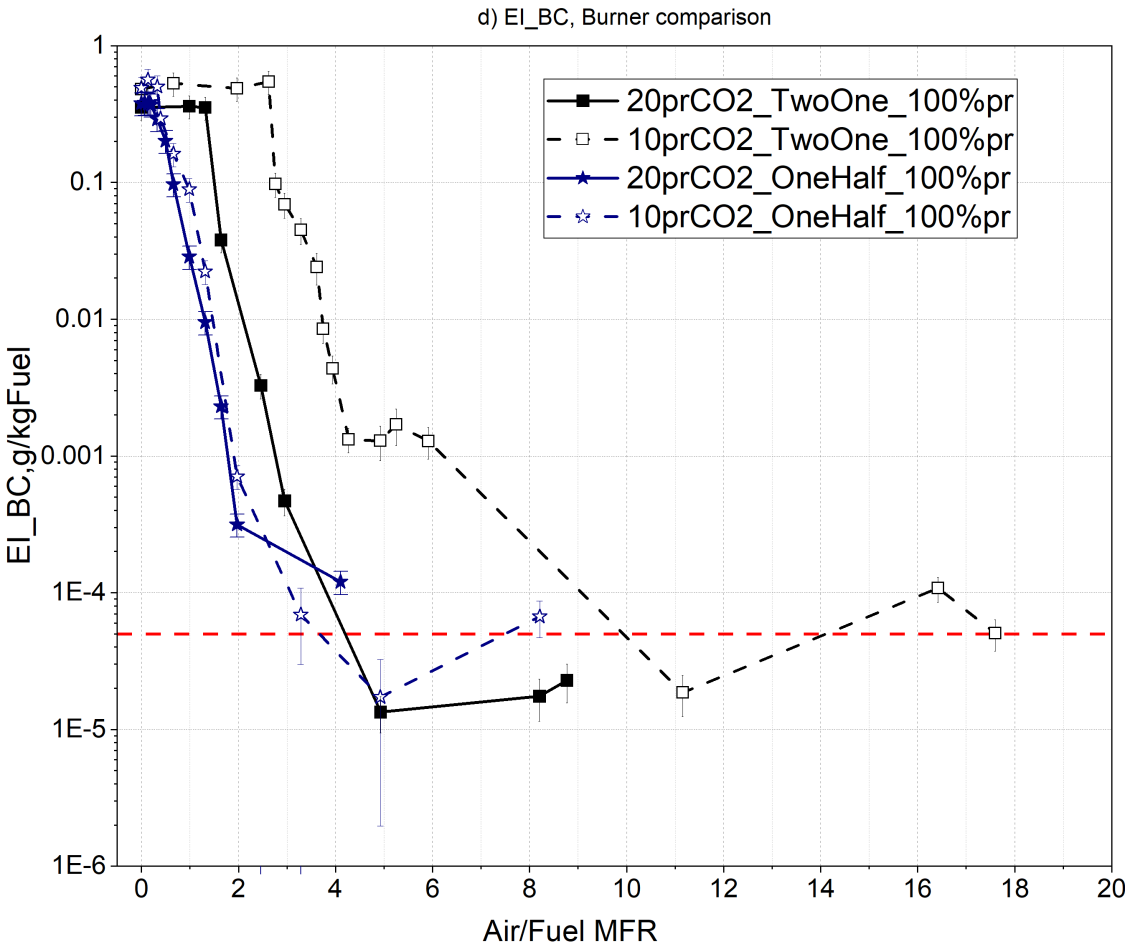
d) EI_BC, Burner comparison
20prCO2_TwoOne_100%pr
10prCO2_TwoOne_100%pr
20prCO2_OneHalf_100%pr
10prCO2_OneHalf_100%pr
EI_BC,g/kgFuel
Air/Fuel MFR
1
0.1
0.01
0.001
1E-4
1E-5
1E-6
0
2
4
6
8
10
12
14
16
18
20

B.2 Flame length plots

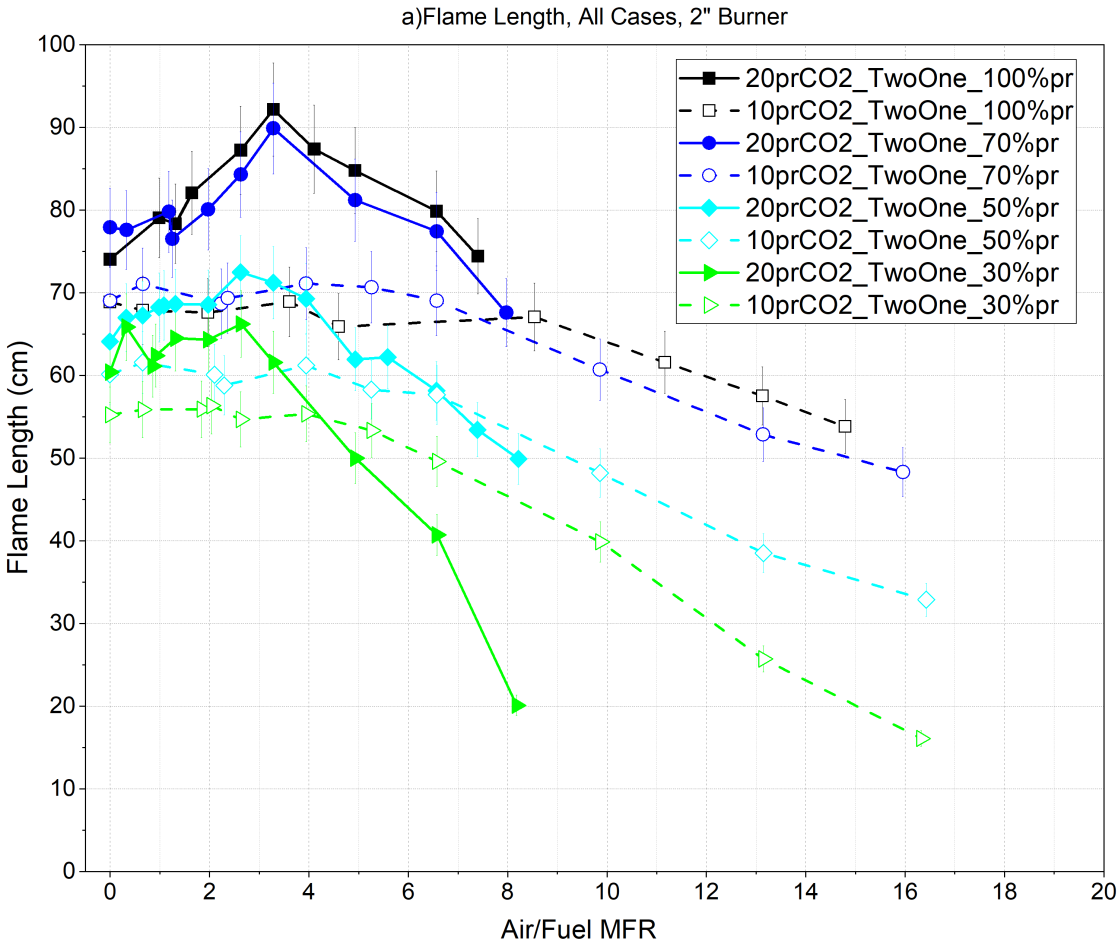

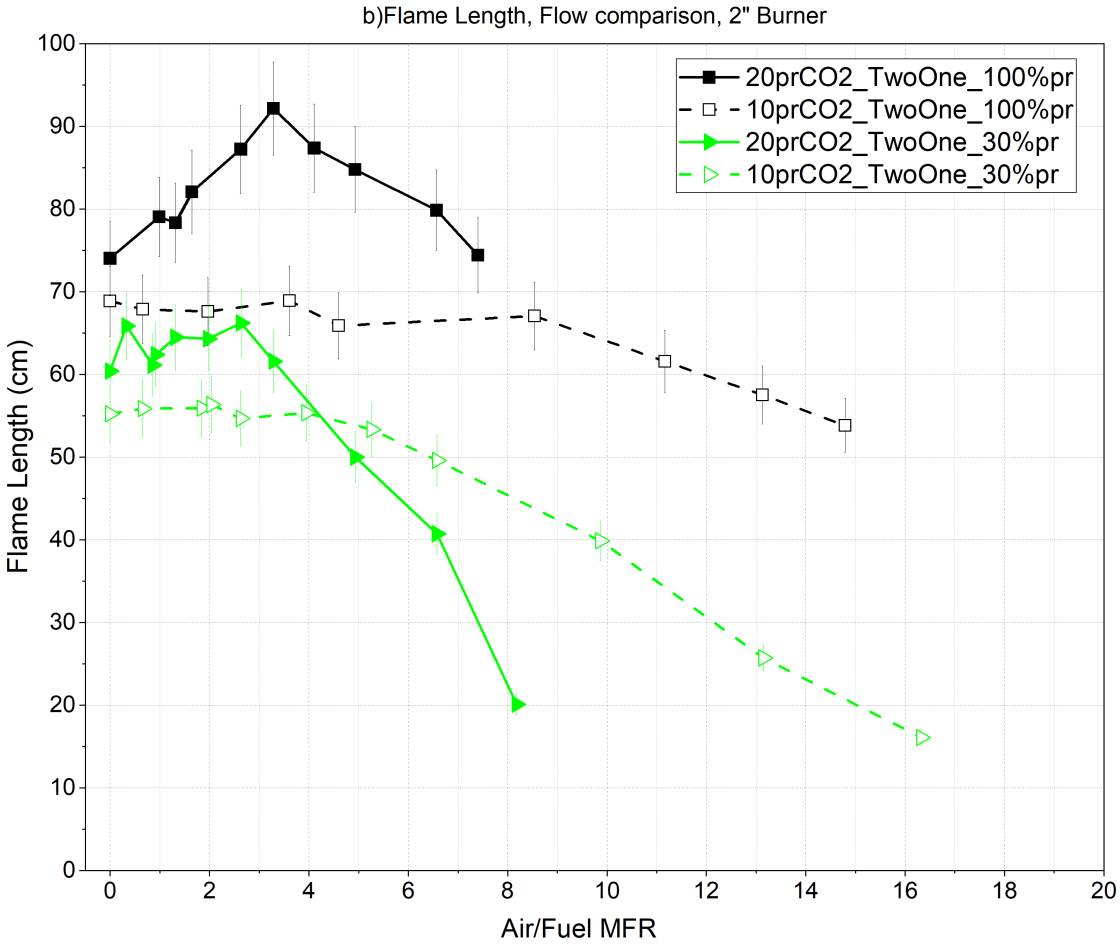
b)Flame Length, Flow comparison, 2" Burner
Flame Length (cm)
Air/Fuel MFR
20prCO2_TwoOne_100%pr
10prCO2_TwoOne_100%pr
20prCO2_TwoOne_30%pr
10prCO2_TwoOne_30%pr
0
10
20
30
40
50
60
70
80
90
100
0
2
4
6
8
10
12
14
16
18
20

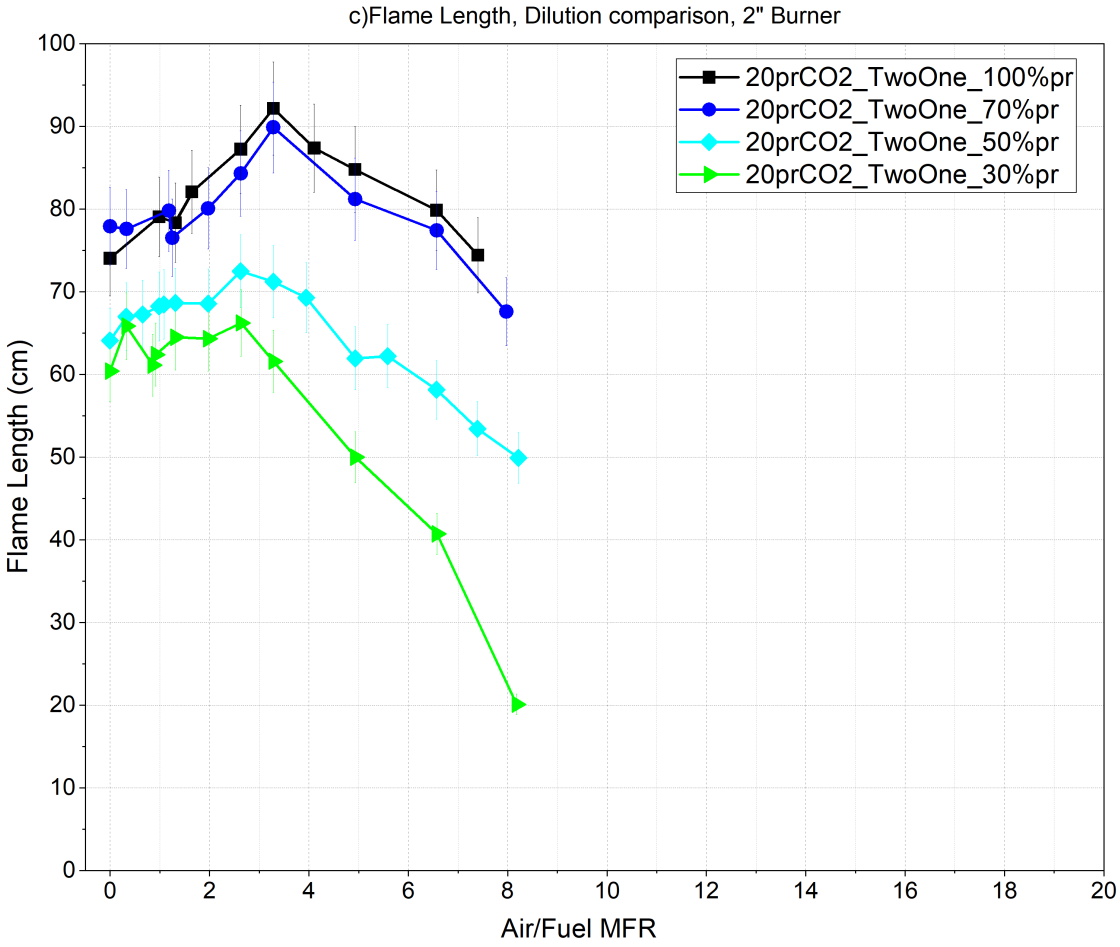
c)Flame Length, Dilution comparison, 2" Burner
Flame Length (cm)
Air/Fuel MFR
20prCO2_TwoOne_100%pr
20prCO2_TwoOne_70%pr
20prCO2_TwoOne_50%pr
20prCO2_TwoOne_30%pr
0
10
20
30
40
50
60
70
80
90
100
0
2
4
6
8
10
12
14
16
18
20

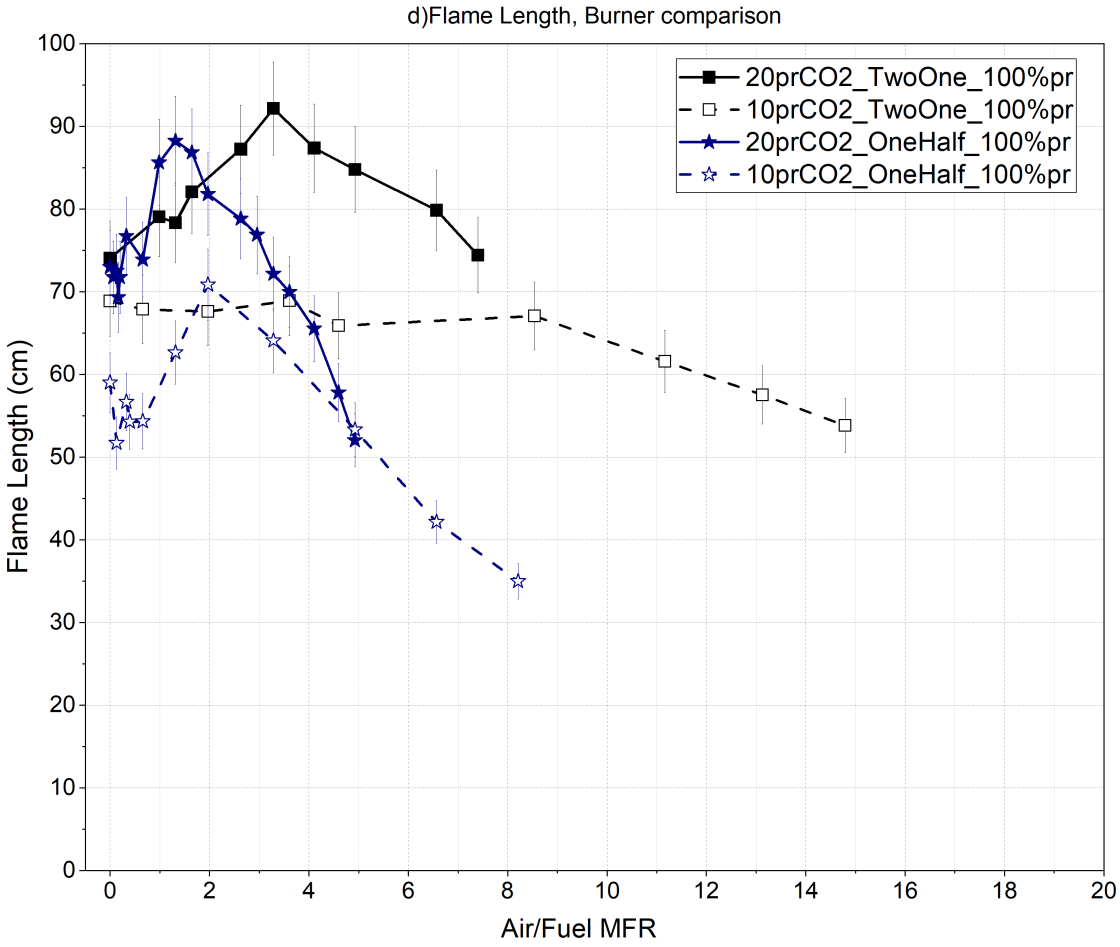
d)Flame Length, Burner comparison
Flame Length (cm)
Air/Fuel MFR
20prCO2_TwoOne_100%pr
10prCO2_TwoOne_100%pr
20prCO2_OneHalf_100%pr
10prCO2_OneHalf_100%pr
0
10
20
30
40
50
60
70
80
90
100
0
2
4
6
8
10
12
14
16
18
20

B.3 Flame width plots

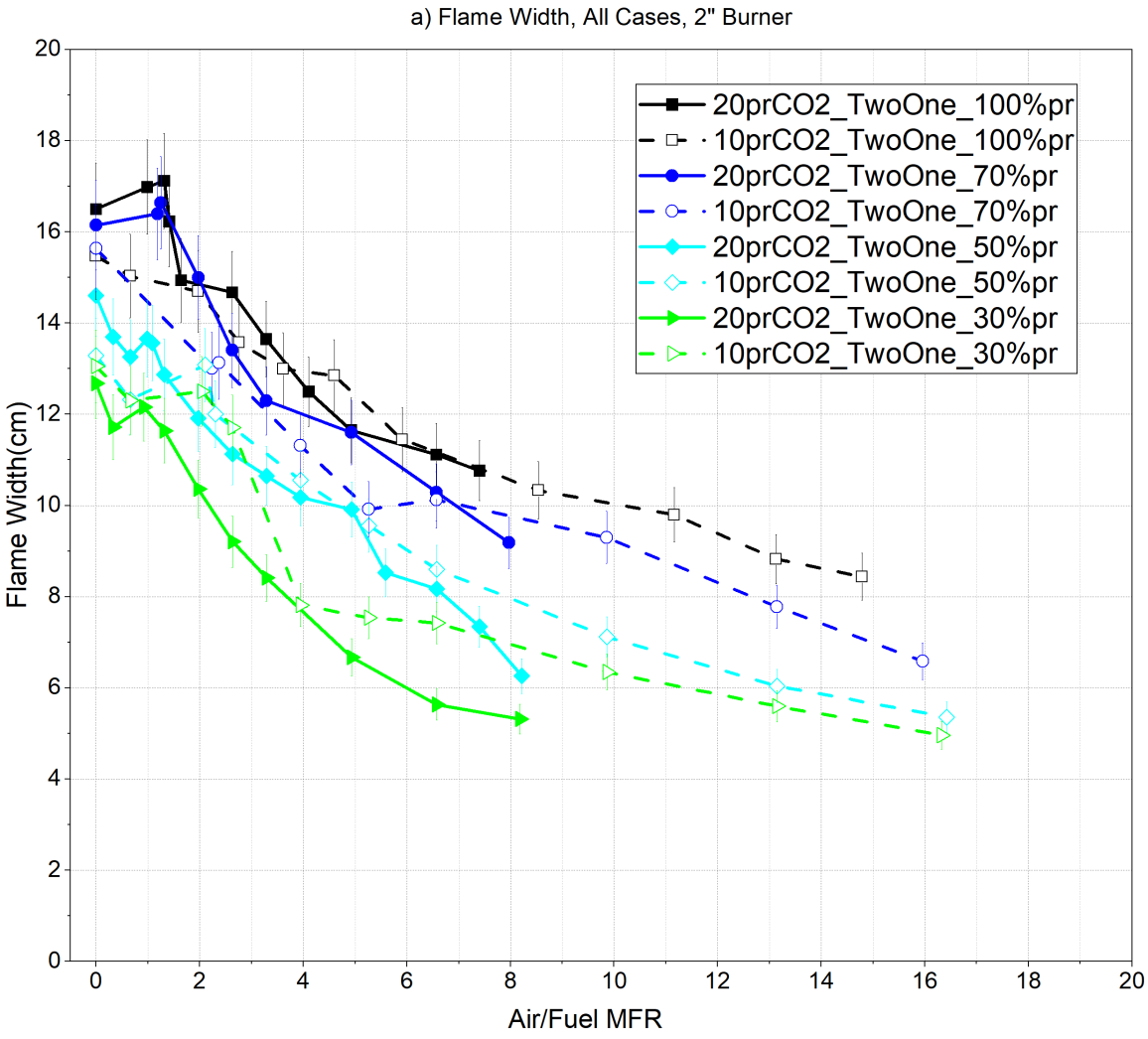

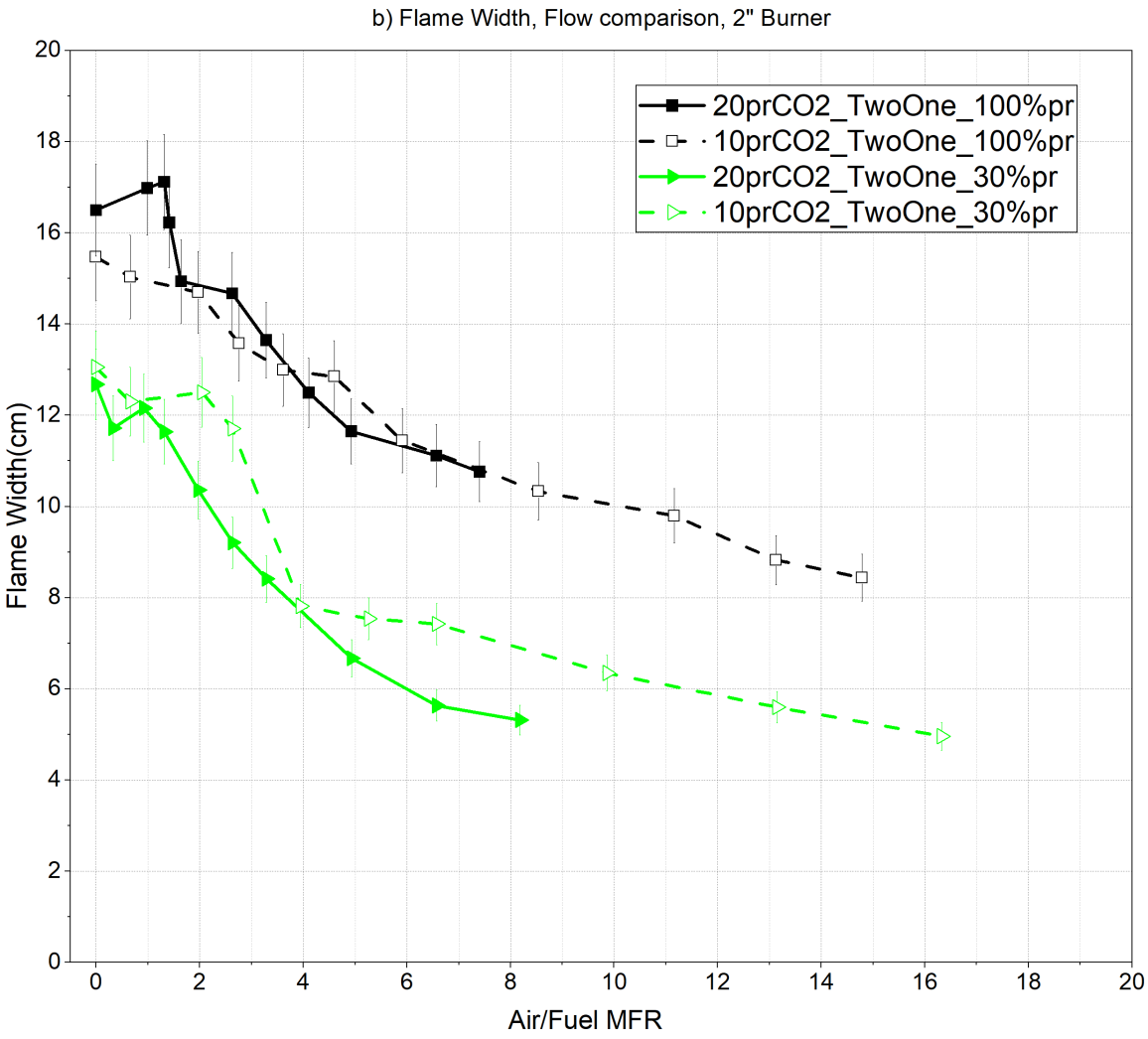
b) Flame Width, Flow comparison, 2" Burner
20prCO2_TwoOne_100%pr
10prCO2_TwoOne_100%pr
20prCO2_TwoOne_30%pr
10prCO2_TwoOne_30%pr
Flame Width(cm)
Air/Fuel MFR
0
2
4
6
8
10
12
14
16
18
20

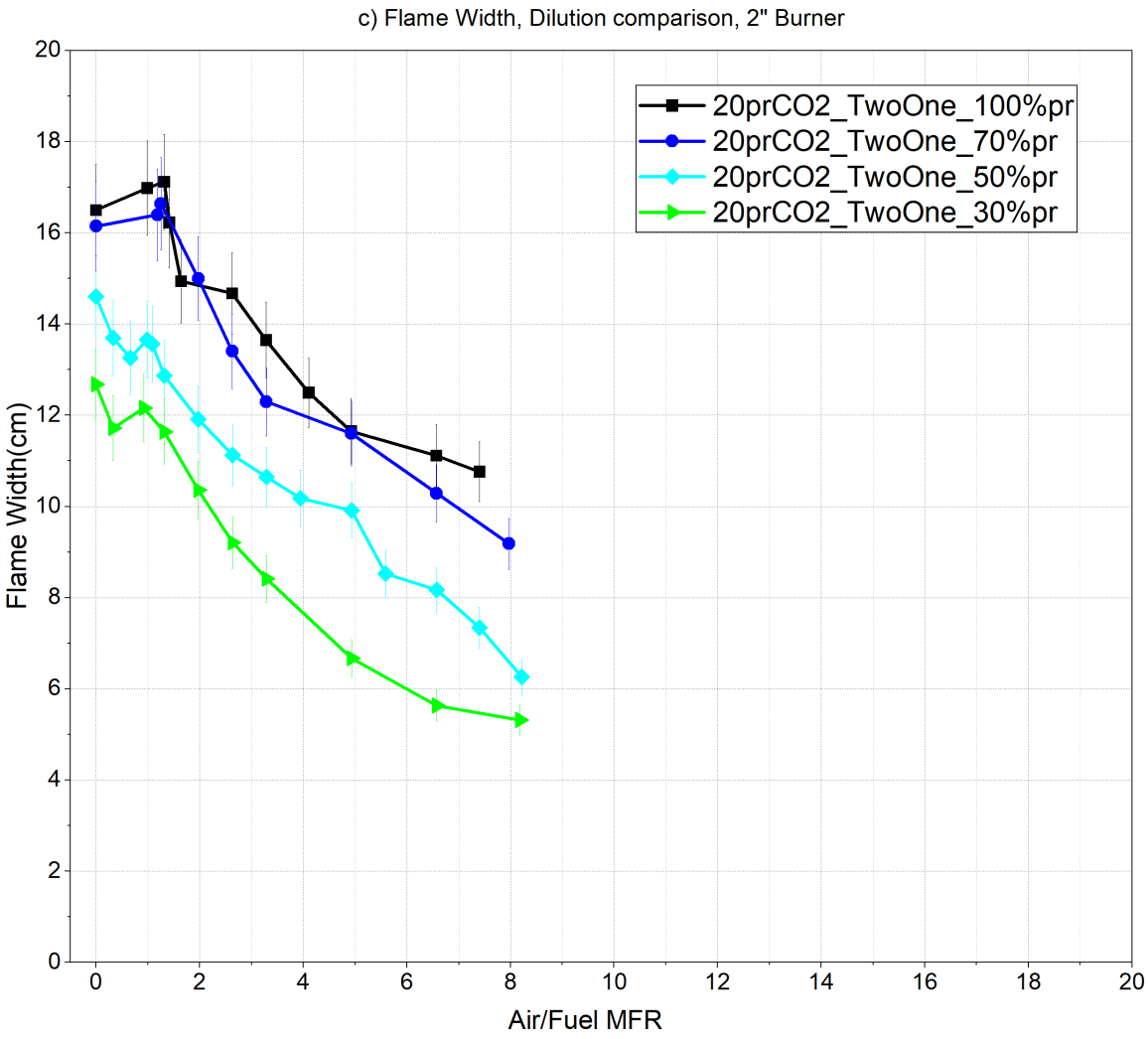
c) Flame Width, Dilution comparison, 2" Burner
20prCO2_TwoOne_100%pr
20prCO2_TwoOne_70%pr
20prCO2_TwoOne_50%pr
20prCO2_TwoOne_30%pr
Flame Width(cm)
Air/Fuel MFR
0
2
4
6
8
10
12
14
16
18
20

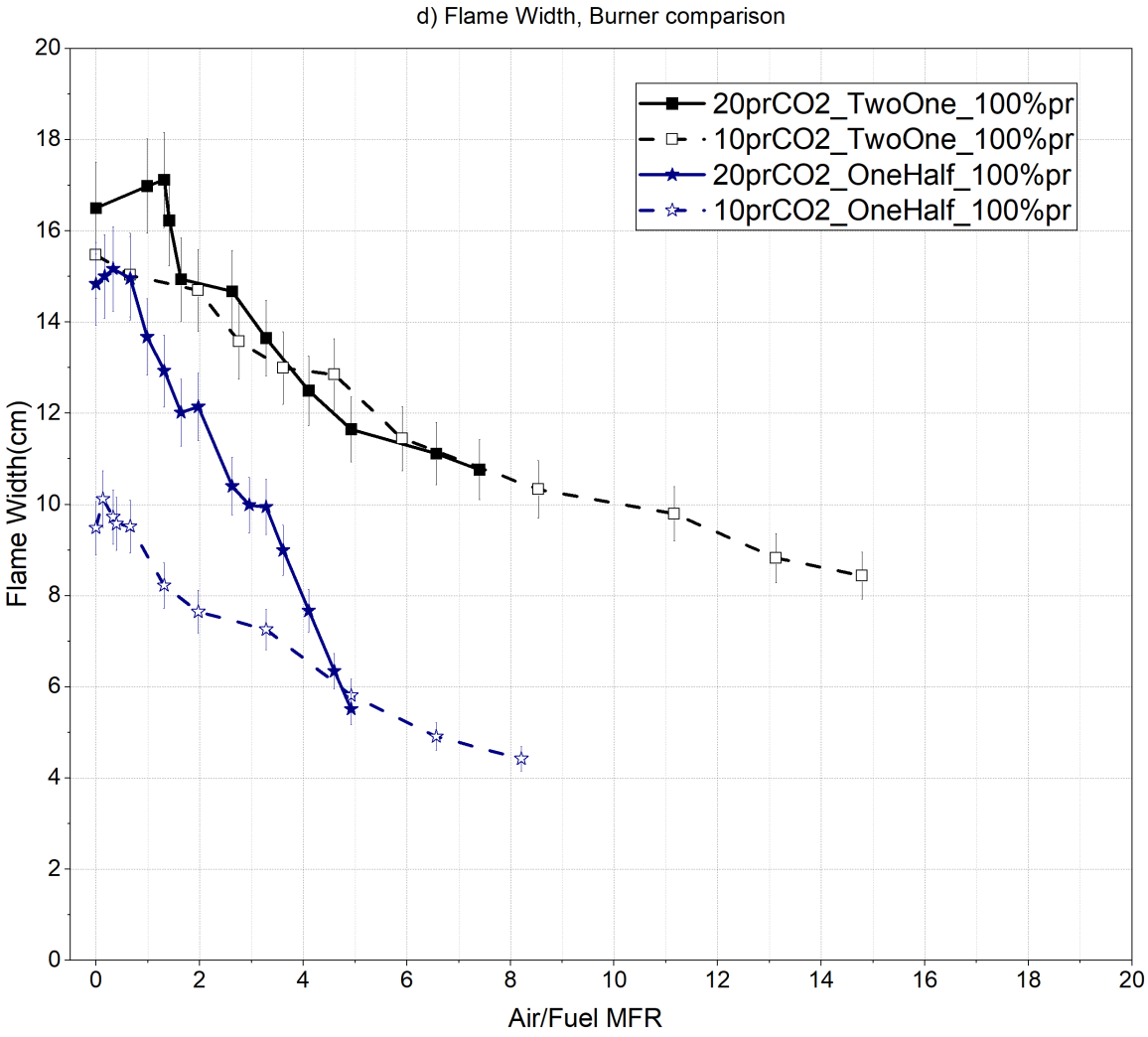
d) Flame Width, Burner comparison
20prCO2_TwoOne_100%pr
10prCO2_TwoOne_100%pr
20prCO2_OneHalf_100%pr
10prCO2_OneHalf_100%pr
Flame Width(cm)
Air/Fuel MFR
0
2
4
6
8
10
12
14
16
18
20

Appendix C

Sample raw instantaneous flame images

C.1 Long exposure images

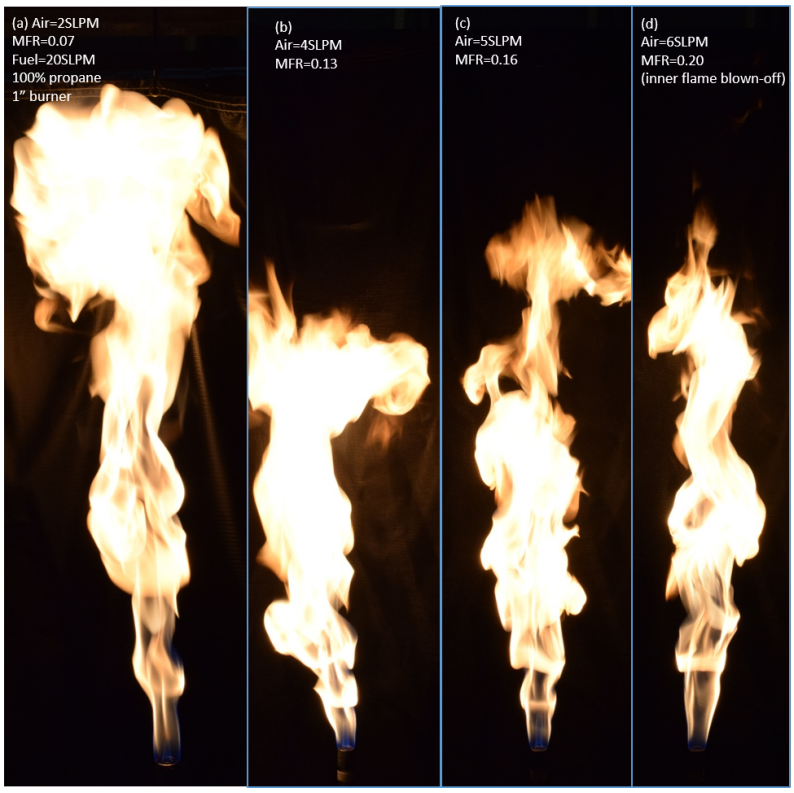

Figure C.1: Long exposure images of 20 SLPM pure propane flame on 1" burner. The inner flame is ignited and elongated with increasing the assist flow rate (a-c), and is finally blown off (d)

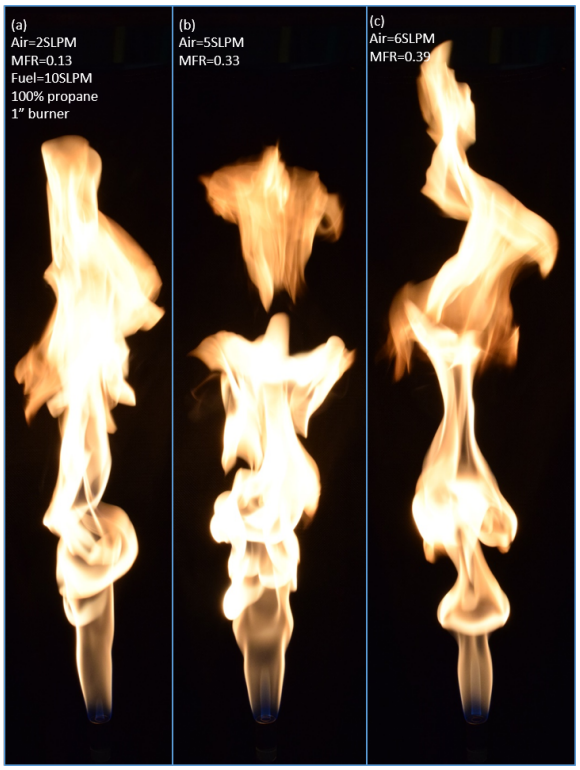

Figure C.2: Long exposure images of 10 SLPM pure propane flame on 1" burner. The inner flame is lifted just before blow-off (c)

C.2 Flame image progression for all cases

A progression of instantaneous flame images with increasing air assist is provided below. Note that for all the cases where an inner flame is observed, the inner flame was blown off within 2 SLPM increase of air assist from the last depicted image with an inner flame.

Figure C.3: Instantaneous images of the flame for the *20prCO2-TwoOne-fuel100percent* case (base case) (also provided in section 3.1)

Figure C.4: Instantaneous images of the flame for the *10prCO2-TwoOne-fuel100percent* case

Figure C.5: Instantaneous images of the flame for the *20prCO2-OneHalf-fuel100percent* case

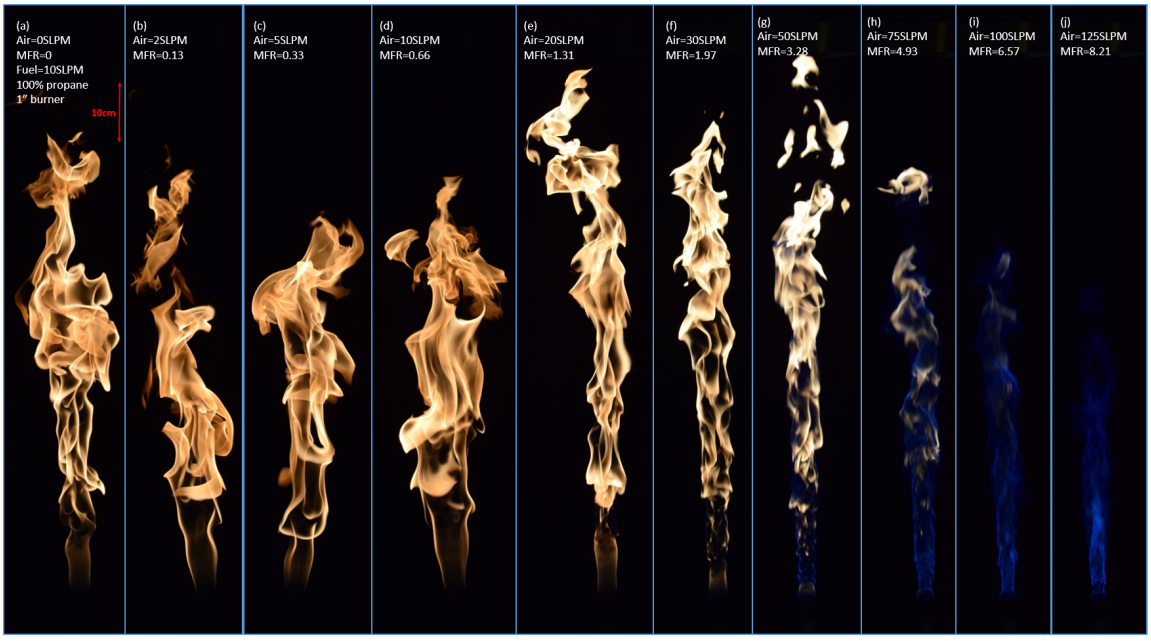

Figure C.6: Instantaneous images of the flame for the *10prCO2-OneHalf-fuel100percent* case

Figure C.7: Instantaneous images of the flame for the *20prCO2-TwoOne-fuel70percent* case

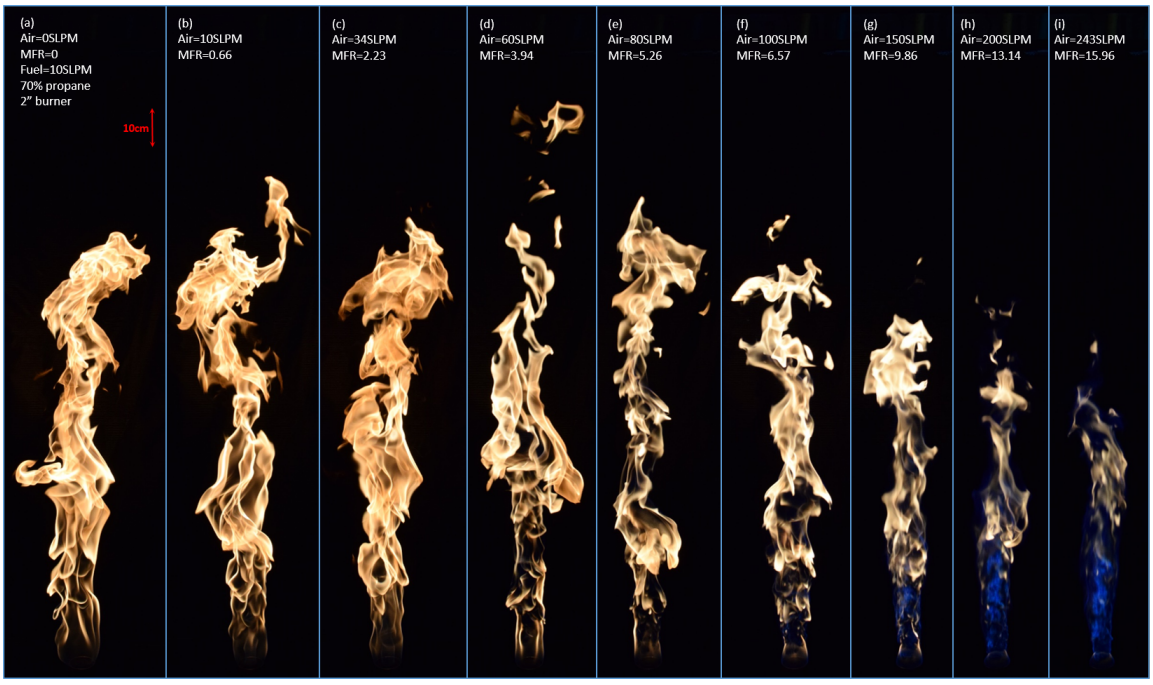

Figure C.8: Instantaneous images of the flame for the *10prCO2-TwoOne-fuel70percent* case

Figure C.9: Instantaneous images of the flame for the *20prCO2-TwoOne-fuel50percent* case

Figure C.10: Instantaneous images of the flame for the *10prCO2-TwoOne-fuel50percent* case

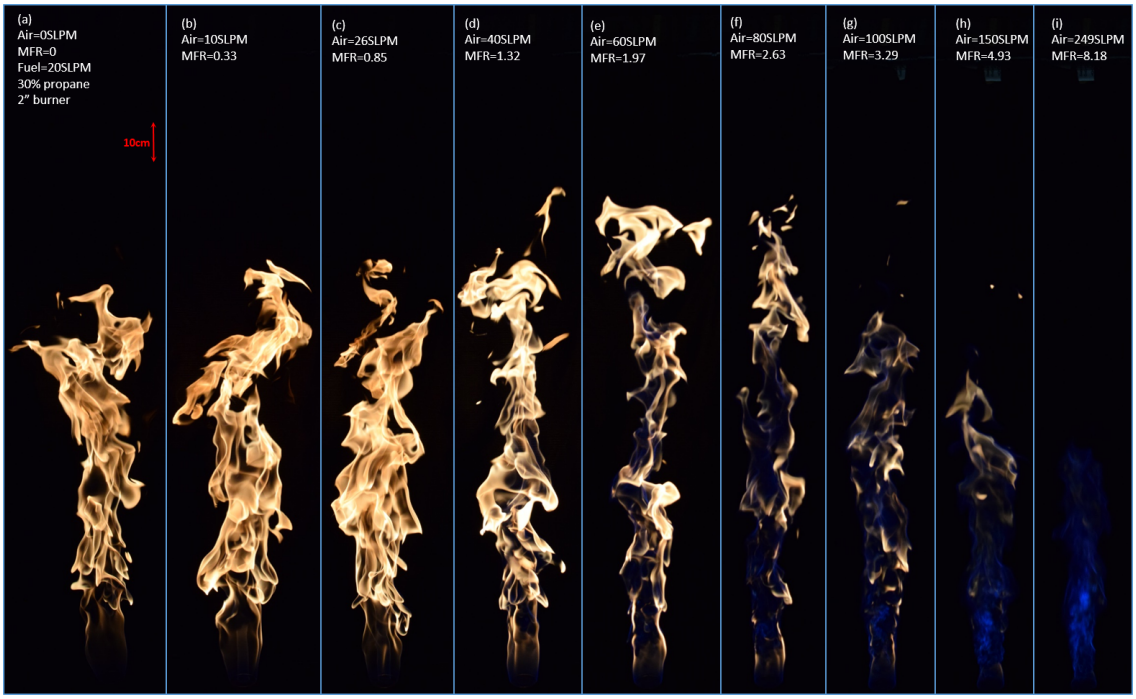

Figure C.11: Instantaneous images of the flame for the *20prCO2-TwoOne-fuel30percent* case

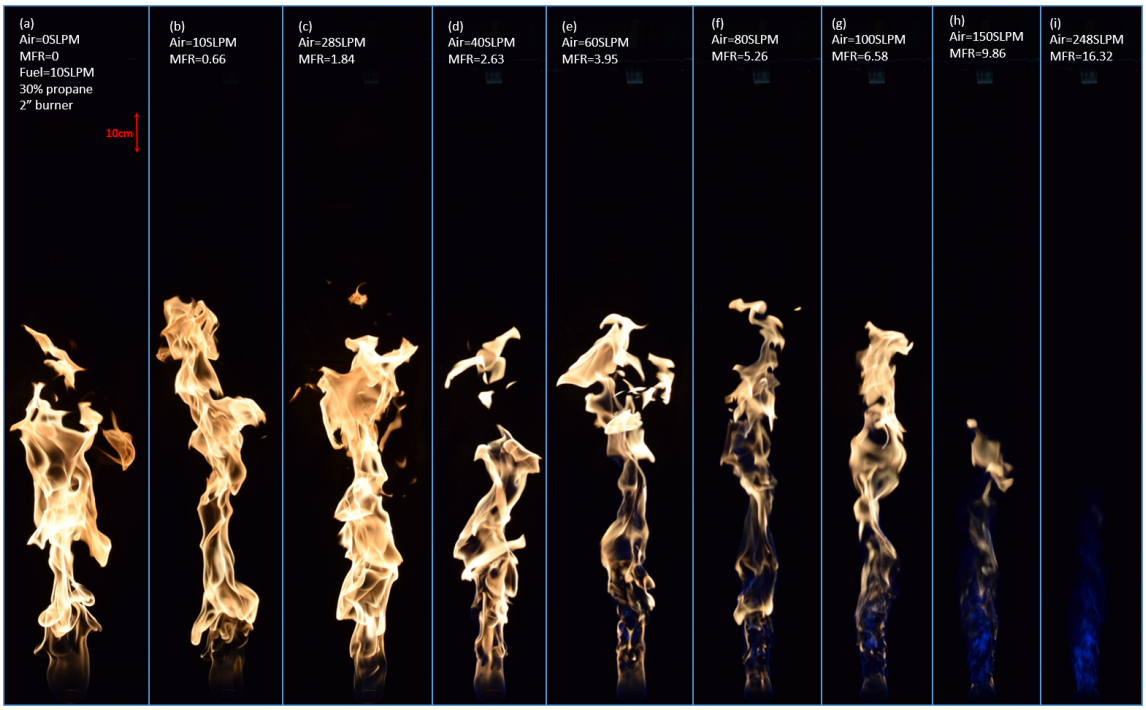

Figure C.12: Instantaneous images of the flame for the *10prCO2-TwoOne-fuel30percent* case

Appendix D

MATLAB image processing code

```
clc
clear
close all


%% image import figure configuration

% To get results for Matlab:
%res=getappdata(hfig_imgImport); fprintf('%s\t 0\t 0\t %.8f\t %.6f\t %.6
    f\t
%%.6f\t %s\t
%%s\t\n',res.case_id,res.px2cm_scale,res.data_contour50_flameLength_cm,
    res.data_contour50_flameWidth_cm,res.data_contour50_burnerWidth_cm,
    num2str(res.data_contour50_neck_width),num2str(res.
    data_contour50_neck_height))

rootDirectory='G:\My Drive\LabVIEW Result Data Files\Thesis Campaign
    Data\March3rd';

hfig_imgImport=figure(1);
set(hfig_imgImport,'Name','Image import and configuration tool',...
     'Tag','fig_ImgImport',...
```

```
18      'NumberTitle','off',...
19      'Units','Normalized',...
20      'Position',[0.1,0.1,0.6,0.8]);
21
22
23
24  % Image preveiw panel
25
26  uipanel('Parent',hfig_imgImport,'Units','normalized',...
27      'Position',[0.01,0.45,.99,.5],'Tag','panel_mainFig');
28
29  uicontrol('Parent',hfig_imgImport,'Style','text',...
30      'Units','Normalized',...
31      'Position',[0.1,0.95,0.15,0.02],...
32      'String','Raw image preview');
33  uicontrol('Parent',hfig_imgImport,'Style','text',...
34      'Units','Normalized',...
35      'Position',[0.43,0.95,0.15,0.02],...
36      'String','Pre-processed image preview');
37  uicontrol('Parent',hfig_imgImport,'Style','text',...
38      'Units','Normalized',...
39      'Position',[0.76,0.95,0.15,0.02],...
40      'String','Processed image preview');
41
42  %Directory browse fields
43
44
45  imgImport_hDirectoryTxt= uicontrol(hfig_imgImport,'Style','edit',...
46      'Units','Normalized',...
47      'Position',[0.01,0.39,0.18,0.03],...
48      'Tag','txt_directory',...
49      'HorizontalAlignment','left',...
```

```
50      'String',pwd);
51
52
53  hlist_images=uicontrol(hfig_imgImport,'Style','listbox',...
54      'Units','Normalized',...
55      'Position',[0.01,0.19,0.12,0.19],...
56      'HorizontalAlignment','left',...
57      'String',0,...
58      'Tag','list_Images',...
59      'Callback',{@ImgListFcn});
60
61
62  imgImport_hBrowseBtn= uicontrol(hfig_imgImport,'Style','pushbutton',...
63      'Units','Normalized',...
64      'Position',[0.14,0.35,0.05,0.03],...
65      'String','Browse',...
66      'BackgroundColor','y',...
67      'Tag','btn_Browse',...
68      'CallBack',{@BrowseFcn,imgImport_hDirectoryTxt,...
69      hlist_images,rootDirectory});
70
71  hbtn_loadConfig= uicontrol(hfig_imgImport,'Style','pushbutton',...
72      'Units','Normalized',...
73      'Position',[0.13,0.31,0.06,0.03],...
74      'String','Load Settings',...
75      'Tag','btn_loadConfig',...
76      'CallBack',{@LoadSettingsFcn});
77
78
79
80
81
```

```
82
83 %% Pre-processing panel
84 hpanel_prePrcs = uipanel('Title','Pre-processing options','Parent',
       hfig_imgImport,'Units','normalized',...
85     'Position',[0.2,0.19,0.35,0.23],'Tag','panel_prePrcs');
86 hlbl_xWinFactor=uicontrol('Parent',hpanel_prePrcs,'Style','text',...
87     'Units','Normalized','HorizontalAlignment','Left',...
88     'Position',[0.01,0.81,0.15,0.1],...
89     'String','X_boost/D:');
90
91 htxt_xWinFactor=uicontrol('Parent',hpanel_prePrcs,'Style','edit',...
92     'Units','Normalized',...
93     'Position',[0.18,0.82,0.1,0.1],...
94     'Tag','txt_xWinFactor',...
95     'String',1.5,'CallBack',{@xWinBoostTxtFcn});
96 setappdata(hfig_imgImport, 'xWinBoost',str2double(htxt_xWinFactor.String
       ));
97
98 hlbl_yWinFactor=uicontrol('Parent',hpanel_prePrcs,'Style','text',...
99     'Units','Normalized','HorizontalAlignment','Left',...
100    'Position',[0.01,0.70,0.15,0.1],...
101    'String','Y_boost/D:');
102
103 htxt_yWinFactor=uicontrol('Parent',hpanel_prePrcs,'Style','edit',...
104    'Units','Normalized',...
105    'Position',[0.18,0.71,0.1,0.1],...
106    'Tag','txt_yWinFactor',...
107    'String',1,'CallBack',{@yWinBoostTxtFcn});
108 setappdata(hfig_imgImport, 'yWinBoost',str2double(htxt_yWinFactor.String
       ));
109
110 hlbl_boostFactor=uicontrol('Parent',hpanel_prePrcs,'Style','text',...
```

```
111     'Units','Normalized','HorizontalAlignment','Left',...
112     'Position',[0.01,0.55,0.18,0.1],...
113     'String','Boost Factor:');
114
115 htxt_boostFactor=uicontrol('Parent',hpanel_prePrcs,'Style','edit',...
116     'Units','Normalized',...
117     'Position',[0.18,0.56,0.1,0.1],...
118     'Tag','txt_boostFactor',...
119     'String',5,'CallBack',{@boostFactorTxtFcn});
120 setappdata(hfig_imgImport, 'boostFactor',str2double(htxt_boostFactor.
        String));
121
122 hbtn_tipROI=uicontrol('Parent',hpanel_prePrcs,'Style','pushbutton',...
123     'Units','Normalized',...
124     'Position',[0.01,0.31,0.28,0.18],...
125     'String','Specify Tip and ROI',...
126     'Tag','btn_tipROI',...
127     'CallBack',{@tipROIFcn});
128 hlbl_tipROI=uicontrol('Parent',hpanel_prePrcs,'Style','text',...
129     'Units','Normalized',...
130     'Position',[0.29,0.31,0.2,0.15],...
131     'String',sprintf('(Region of Interest)'));
132
133 setappdata(hfig_imgImport, 'burner_Rim',[716,2760;863,2760]);
134 setappdata(hfig_imgImport, 'ROI_rect', [275 20 1300 2860]);
135
136 hlbl_scale=uicontrol('Parent',hpanel_prePrcs,'Style','text',...
137     'Units','Normalized',...
138     'Position',[0.19,0.1,0.2,0.15],...
139     'String',sprintf('Scale (px:cm) \n 27:1'),'Tag','lbl_scale');
140
141 hbtn_scale=uicontrol('Parent',hpanel_prePrcs,'Style','pushbutton',...
```

```
142     'Units','Normalized',...
143     'Position',[0.01,0.1,0.18,0.15],...
144     'String','Reset Scale',...
145     'Tag','btn_scale',...
146     'CallBack',{@scaleFcn});
147
148 setappdata(hfig_imgImport, 'px2cm_scale',1/28);
149
150 %% Processing panel
151 hpanel_Prcs = uipanel('Title','Processing options','Parent',
        hfig_imgImport,'Units','normalized',...
152     'Position',[0.56,0.19,0.35,0.23],'Tag','panel_Prcs');
153 hlbl_noMaxBlobs=uicontrol('Parent',hpanel_Prcs,'Style','text',...
154     'Units','Normalized','HorizontalAlignment','Left',...
155     'Position',[0.01,0.81,0.25,0.1],...
156     'String','Max No. of blobs:');
157 setappdata(hfig_imgImport, 'noMaxBlobs',10)
158
159 htxt_noMaxBlobs=uicontrol('Parent',hpanel_Prcs,'Style','edit',...
160     'Units','Normalized',...
161     'Position',[0.27,0.82,0.1,0.1],...
162     'Tag','txt_noMaxBlobs',...
163     'String',10,...
164     'CallBack',{@noMaxBlobsTxtFcn});
165 hlbl_bnrTrsd=uicontrol('Parent',hpanel_Prcs,'Style','text',...
166     'Units','Normalized',...
167     'Position',[0.01,0.6,0.25,0.2],...
168     'String','Binarization threshold (0-256):');
169
170 htxt_bnrTrsd=uicontrol('Parent',hpanel_Prcs,'Style','edit',...
171     'Units','Normalized',...
172     'Position',[0.27,0.65,0.1,0.1],...
```

```
173     'Tag','txt_bnrTrsd',...
174     'String',10,...
175     'CallBack',{@bnrTrsdTxtFcn});
176 setappdata(hfig_imgImport, 'bnrTrsd',10)
177 
178 
179 hlbl_flameAttchd=uicontrol('Parent',hpanel_Prcs,'Style','text',...
180     'Units','Normalized',...
181     'Position',[0.01,0.4,0.25,0.2],...
182     'String',sprintf('White line at rim:'));
183 
184 hchbx_flameAttchd=uicontrol('Parent',hpanel_Prcs,'Style','checkbox',...
185     'Units','Normalized',...
186     'Position',[0.27,0.45,0.25,0.2],...
187     'Tag','chbx_flameAttchd',...
188     'String','Flame Attached',...
189     'Value',1,...
190     'CallBack',{@flameAttchd_chbxFcn});
191 setappdata(hfig_imgImport, 'flameAttached',1);
192 
193 
194 
195 %
196 
197 
198 % Image processing button
199 
200 hbtn_intrmContours=uicontrol(hfig_imgImport,'Style','pushbutton',...
201     'Units','Normalized',...
202     'Position',[0.78,0.12,0.2,0.04],'Tag','intrmContours',...
203     'String','Generate intermittency contours',...
204     'CallBack',{@intrmContours});
```

```
205
206
207 %% Functions
208
209 function boostFactorTxtFcn(hObject,~)
210
211 hfig_imgImport=findobj('Tag','fig_ImgImport');
212 setappdata(hfig_imgImport, 'boostFactor',str2double(hObject.String));
213
214 end
215
216 function xWinBoostTxtFcn(hObject,~)
217
218 hfig_imgImport=findobj('Tag','fig_ImgImport');
219 setappdata(hfig_imgImport, 'xWinBoost',str2double(hObject.String));
220
221 end
222
223
224 function yWinBoostTxtFcn(hObject,~)
225
226 hfig_imgImport=findobj('Tag','fig_ImgImport');
227 setappdata(hfig_imgImport, 'yWinBoost',str2double(hObject.String));
228
229 end
230
231
232
233 function tipROIFcn(hObject,event)
234
235 fig_pts=figure(2);
236 set(fig_pts,'Name','Burner tip and region selection tool',...
```

```
237     'NumberTitle','off',...
238     'Units','Normalized',...
239     'Position',[0.3  0.15  0.2  0.7]);
240
241 btn_ptsReset=uicontrol(fig_pts,'Style','pushbutton',...
242     'Units','Normalized',...
243     'Position',[0.37,0.1,0.25,0.04],...
244     'String','Reset burner tip',...
245     'Tag','btn_ptsReset',...
246     'CallBack',{@ptsResetFcn});
247
248 btn_ROIReset=uicontrol(fig_pts,'Style','pushbutton',...
249     'Units','Normalized',...
250     'Position',[0.35,0.04,0.3,0.04],...
251     'String','Reset ROI',...
252     'Tag','btn_ROIReset',...
253     'CallBack',{@ROIResetFcn});
254 ax1 = axes('Position',[0.01,0.14,0.98,0.85],'Box','on','Tag','
        axes_PointsRegion');
255
256 htxt_directory=findobj('Tag','txt_directory');
257 hlist_images=findobj('Tag','list_Images');
258 Val=hlist_images.Value;
259 imageDir=fullfile(htxt_directory.String, hlist_images.String(Val));
260 imgOrientFixed=fixOrient(imageDir{1});
261
262
263
264 image=imshow(imgOrientFixed,'Parent',ax1);
265
266
267     function ptsResetFcn(hObject,event)
```

```
268
269         [x,y]=ginput(2);
270         y=ones(2,1)*mean(y)
271         delete(findobj('Tag','plot_burnerRim'))
272         hold on
273         line1=plot(x,y,'m','LineWidth',3,'Tag','plot_burnerRim');
274         imgImport_fig=findobj('Tag','fig_ImgImport');
275         setappdata(imgImport_fig, 'burner_Rim',floor([x y]))
276         %     setguidata
277
278     end
279
280     function ROIResetFcn(hObject,event)
281
282         rect = getrect(ax1);
283         delete(findobj('Tag','plot_ROI'))
284         %     y=ones(2,1)*mean(y)
285         hold on
286         rect1=rectangle('Position',rect,'EdgeColor','r','LineWidth',2,'
              Tag','plot_ROI');
287         imgImport_fig=findobj('Tag','fig_ImgImport');
288         setappdata(imgImport_fig, 'ROI_rect',rect)
289
290     end
291
292 % function [x,y]=click(o, event)
293 %     pt = get(ax1, 'CurrentPoint'); hold on rectangle('Position',pos)
294 %     x=pt(1,1); y=pt(1,2);
295 % %     plot(pt(1,1),pt(1,2),'r+', 'MarkerSize', 30, 'LineWidth', 2) end
296
297 end
298
```

```
299 function scaleFcn(hObject,event)
300
301
302 imgImport_fig=findobj('Tag','fig_ImgImport');
303 hfig_scale=figure(3);
304 set(hfig_scale,'Tag','fig_scale',...
305     'Units','Normalized',...
306     'Position',[0.1,0.1,0.6,0.8]);
307
308 hbtn_scaleReset=uicontrol(hfig_scale,'Style','pushbutton',...
309     'Units','Normalized',...
310     'Position',[0.4,0.1,0.2,0.04],...
311     'String','Reset Scale: indicate 10cm scale with pointer',...
312     'Tag','btn_scaleReset',...
313     'CallBack',{@scaleResetFcn});
314
315 hbtn_measure=uicontrol(hfig_scale,'Style','pushbutton',...
316     'Units','Normalized',...
317     'Position',[0.61,0.1,0.13,0.04],...
318     'String','Measure a custom length',...
319     'Tag','btn_measure',...
320     'CallBack',{@measureFcn});
321
322 hpanel_img1 = uipanel('Parent',hfig_scale,'Units','normalized',...
323     'Position',[0.01,0.14,0.98,0.85],'Tag','panel_img1');
324 ax1 = axes('Parent',hpanel_img1,'Tag','axes_PointsRegion');
325
326 uicontrol('Parent',hfig_scale,'Style','text',...
327     'Units','Normalized',...
328     'Position',[0.32,0.04,0.19,0.03],...
329     'String','Scale: 1cm:px',...
330     'HorizontalAlignment','right');
```

```
331
332 htxt_scale=uicontrol('Parent',hfig_scale,'Style','edit',...
333     'Units','Normalized',...
334     'Position',[0.52,0.05,0.12,0.03],...
335     'Tag','txt_scaleReset',...
336     'String',1/getappdata(imgImport_fig, 'px2cm_scale'),...
337     'CallBack',{@scaleTxtFcn});
338 htxt_measure=uicontrol('Parent',hfig_scale,'Style','text',...
339     'Units','Normalized',...
340     'Position',[0.75,0.08,0.15,0.04],...
341     'HorizontalAlignment','left','Tag','txt_measure',...
342     'String',0);
343
344 htxt_directory=findobj('Tag','txt_directory');
345 [file,path] = uigetfile([htxt_directory.String,'\*.jpg'],'Select image
    with scale guide');
346
347 imageDir=fullfile(path,file);
348 imgOrientFixed=fixOrient(imageDir);
349
350
351 figure(3)
352 image1=image(imgOrientFixed,'Parent',ax1);
353 hSP = imscrollpanel(hpanel_img1,image1);
354 % hMagBox = immagbox(hpanel_img1,image1);
355 api = iptgetapi(hSP);
356 % api.setMagnification(api.findFitMag())
357 api.setVisibleLocation(0.5,0)
358
359 % set(ax1,'DataAspectRatio',[1 1 1])
360
361
```

```
362
363     function scaleResetFcn(hObject,event)
364         delete(findobj('Tag','plot_scaleLine'))
365         [x,y]=ginput(2);
366
367         L_px=sqrt((x(2)-x(1))^2+(y(2)-y(1))^2);
368         L_px=L_px/10;
369         htxt_scale.String=L_px;
370         hold on
371         plot(x,y,'r','Parent',ax1,'LineWidth',3,'Tag','plot_scaleLine');
372         imgImport_fig=findobj('Tag','fig_ImgImport');
373         setappdata(imgImport_fig, 'px2cm_scale',1/L_px);
374         hlbl_scaleMain=findobj('Tag','lbl_scale');
375         hlbl_scaleMain.String=sprintf('Scale (px:cm) \n %0.0f:1',L_px);
376
377     end
378
379     function measureFcn(hObject,event)
380         delete(findobj('Tag','plot_scaleLine'))
381         [x,y]=ginput(2);
382         imgImport_fig=findobj('Tag','fig_ImgImport');
383         px2cm=getappdata(imgImport_fig, 'px2cm_scale');
384         L_px=sqrt((x(2)-x(1))^2+(y(2)-y(1))^2);
385         length_measured=L_px*px2cm;
386         htxt_measure.String=sprintf('Length(cm) %0.2f',length_measured);
387         hold on
388         plot(x,y,'r','Parent',ax1,'LineWidth',3,'Tag','plot_scaleLine');
389
390
391     end
392
393     function scaleTxtFcn(hObject,event)
```

```
394
395         L_px=str2double(hObject.String);
396         imgImport_fig=findobj('Tag','fig_ImgImport');
397         setappdata(imgImport_fig, 'px2cm_scale',1/L_px);
398         hlbl_scaleMain=findobj('Tag','lbl_scale');
399         hlbl_scaleMain.String=sprintf('Scale (px:cm) \n %0.0f:1',L_px);
400     end
401
402
403 end
404
405 function BrowseFcn(hObject,event,imgImport_hDirectoryTxt,
    imgImport_hImgList,rootDirectory)
406
407 [~, folder] = uigetfile(fullfile(rootDirectory, '*.jpg'));
408 imgImport_hDirectoryTxt.String=folder;
409
410 files=dir(fullfile(folder, '*.jpg'));
411 imgImport_hImgList.String={files.name};
412 end
413
414
415 function LoadSettingsFcn(hObject,~)
416
417 hfig_imgImport=findobj('Tag','fig_ImgImport');
418 imgImport_hDirectoryTxt=findobj('Tag','txt_directory');
419 [file, folder] = uigetfile(imgImport_hDirectoryTxt.String);
420 a=load(fullfile(folder,file));
421
422
423 setappdata(hfig_imgImport, 'px2cm_scale',a.results.px2cm_scale)
```

```
424 set(findobj('Tag','lbl_scale'),'String',sprintf('Scale (px:cm) \n %0.0f
        :1',1/a.results.px2cm_scale));
425
426 setappdata(hfig_imgImport, 'noMaxBlobs',a.results.noMaxBlobs)
427 set(findobj('Tag','txt_noMaxBlobs'),'String',a.results.noMaxBlobs);
428
429 setappdata(hfig_imgImport, 'bnrTrsd',a.results.bnrTrsd)
430 set(findobj('Tag','txt_bnrTrsd'),'String',a.results.bnrTrsd)
431
432 setappdata(hfig_imgImport, 'flameAttached',a.results.flameAttached)
433 temp=findobj('Tag','chbx_flameAttchd');
434 % set(findobj('Tag','chbx_flameAttchd'),Value,a.results.flameAttached)
435 temp.Value=a.results.flameAttached;
436
437
438 setappdata(hfig_imgImport, 'burner_Rim',a.results.burner_Rim)
439 setappdata(hfig_imgImport, 'ROI_rect',a.results.ROI_rect)
440
441
442
443 setappdata(hfig_imgImport, 'xWinBoost',a.results.xWinBoost)
444 set(findobj('Tag','txt_xWinFactor'),'String',a.results.xWinBoost)
445 setappdata(hfig_imgImport, 'yWinBoost',a.results.yWinBoost)
446 set(findobj('Tag','txt_yWinFactor'),'String',a.results.yWinBoost)
447 setappdata(hfig_imgImport, 'boostFactor',a.results.boostFactor)
448 set(findobj('Tag','txt_boostFactor'),'String',a.results.boostFactor)
449
450
451 end
452
453
454 function ImgListFcn(hObject,event)
```

```
455 delete(findobj('Tag','panel_mainFig'));
456 htxt_directory=findobj('Tag','txt_directory');
457 hfig_imgImport=findobj('Tag','fig_ImgImport');
458 ROI_rect_coords=getappdata(hfig_imgImport, 'ROI_rect');
459 rim_coords=getappdata(hfig_imgImport, 'burner_Rim');
460
461 Val=hObject.Value;
462 imageDir=fullfile(htxt_directory.String, hObject.String(Val));
463 img_OrientFixed=fixOrient(imageDir{1});
464 img_preProcessed=preProcess(imageDir{1});
465 img_processed=imageProcess(img_preProcessed);
466 % AR=size(imgOrientFixed,2)/size(imgOrientFixed,1);
467 % imoverview_htool=getappdata(hObject.Parent,'appdata_imoverview_htool')
    ;
468
469 % close(imoverview_htool)
470
471 % Setting Scrollpanel axes (shorturl.at/fGQZ7) ppp =
472 % uipanel('Units','normalized','Position',[0.01,0.45,0.4,0.5]);
473 hpanel_mainFig=uipanel('Parent',hObject.Parent,'Units','normalized',...
474     'Position',[0.01,0.45,.99,.5],'Tag','panel_mainFig');
475 hpanel_img1 = uipanel('Parent',hpanel_mainFig,'Units','normalized',...
476     'Position',[0 0 0.32 1],'Tag','panel_img1');
477 ax1 = axes('parent',hpanel_img1,'ActivePositionProperty','Position','
    Position',[0 0 1 1]);
478
479
480 hpanel_img2 = uipanel('Parent',hpanel_mainFig,'Units','normalized',...
481     'Position',[0.34 0 0.32 1],'Tag','panel_img2');
482 ax2 = axes('parent',hpanel_img2,'ActivePositionProperty','Position','
    Position',[0 0 1 1]);
483
```

```
484
485 hpanel_img3 = uipanel('Parent',hpanel_mainFig,'Units','normalized',...
486     'Position',[0.68 0 0.32 1],'Tag','panel_img3');
487 ax3 = axes('parent',hpanel_img3,'ActivePositionProperty','Position','
    Position',[0 0 1 1]);
488
489 % Link for adjusting axis tick labels:
490 % https://www.mathworks.com/help/matlab/creating_plots/change-tick-marks
    -and-tick-labels-of-graph-1.html
491
492 % ax2 = axes('parent',hpanel_mainFig,'position',[0.34 0 0.32
493 % 1],'Units','normalized'); daspect([AR 1 1]) ax3 =
494 % axes('parent',hpanel_mainFig,'position',[0.68 0 0.32
495 % 1],'Units','normalized'); daspect([AR 1 1]) hold on; hold off;
496 him1 = image(img_OrientFixed,'parent',ax1);
497 set(ax1,'DataAspectRatio',[1 1 1])
498 him2 = image(img_preProcessed,'parent',ax2);
499 set(ax2,'DataAspectRatio',[1 1 1])
500 rectangle('Position',ROI_rect_coords,'parent',ax2,'EdgeColor','r','
    LineStyle','--')
501 line([rim_coords(1,1) rim_coords(2,1)],[rim_coords(1,2) rim_coords(1,2)
    ],'Color','green','parent',ax2)
502 him3 = imshow(img_processed,'parent',ax3);
503 set(ax3,'DataAspectRatio',[1 1 1])
504
505 end
506
507
508
509 function intrmContours(hObject,event)
510
511 hfig_imgImport=findobj('Tag','fig_ImgImport');
```

```
512 htxt_directory=findobj('Tag','txt_directory');
513 px2cm=getappdata(hfig_imgImport,'px2cm_scale');
514 val_noMaxBlobs=getappdata(hfig_imgImport, 'noMaxBlobs');
515
516 coords=getappdata(hfig_imgImport, 'burner_Rim');
517 Xmin_Noz=coords(1,1);
518 Xmax_Noz=coords(2,1);
519 Noz_D=Xmax_Noz-Xmin_Noz+1;
520
521 files=dir(fullfile(htxt_directory.String, '*.jpg'));
522 filenames={files.name};
523 no_img=length(filenames);
524 setappdata(hfig_imgImport,'no_images',no_img);
525 flames_sum=0;
526
527 tic
528 for k=1:no_img
529 imageDir=fullfile(htxt_directory.String, filenames(k));
530 imageDir=imageDir{1};
531 img_preProcessed=preProcess(imageDir);
532 img_processed=imageProcess(img_preProcessed);
533
534 flames_sum=flames_sum+img_processed;
535
536 end
537 toc
538
539 flame_contour10=flames_sum>.1*k;
540 flame_contour10 = bwareafilt(flame_contour10, val_noMaxBlobs);
541 flame_contour10 = imfill(flame_contour10,'holes');
542 setappdata(hfig_imgImport,'matrix_contour10',flame_contour10)
543
```

```
544 flame_contour50=flames_sum>.5*k;
545 flame_contour50 = bwareafilt(flame_contour50, val_noMaxBlobs);
546 flame_contour50 = imfill(flame_contour50,'holes');
547 setappdata(hfig_imgImport,'matrix_contour50',flame_contour50)
548
549 flame_contour90=flames_sum>.9*k;
550 flame_contour90 = bwareafilt(flame_contour90, val_noMaxBlobs);
551 % flame_contour90 = imfill(flame_contour90,'holes');
552 setappdata(hfig_imgImport,'matrix_contour90',flame_contour90)
553
554 recs=regionprops(bwareafilt(flame_contour50, 1),'BoundingBox','Area');
555 recs_Box=cat(1,recs.BoundingBox);
556 recs_area=cat(1,recs.Area);
557
558 [~,mainBlob_ind]=max(recs_area); %In case other objects than the flame
    have found their way into the contour
559 flameBox=recs_Box(mainBlob_ind,:);
560 setappdata(hfig_imgImport,'data_contour50_flameBox',flameBox)
561 flameLength=flameBox(4);
562 setappdata(hfig_imgImport,'data_contour50_flameLength_cm',flameLength*
    px2cm)
563 flameWidth=flameBox(3);
564 setappdata(hfig_imgImport,'data_contour50_flameWidth_cm',flameWidth*
    px2cm)
565 setappdata(hfig_imgImport,'data_contour50_flameLength_overD',flameLength
    /Noz_D)
566 setappdata(hfig_imgImport,'data_contour50_burnerWidth_cm',Noz_D*px2cm)
567
568
569 hfig_contours=figure(4);
570 set(hfig_contours,'Name','Intermittency contours results',...
571     'Tag','fig_contours',...
```

```
572     'NumberTitle','off',...
573     'Units','Normalized',...
574     'Position',[0.1,0.1,0.6,0.8]);
575 hbtn_saveData=uicontrol(hfig_contours,'Style','pushbutton',...
576     'Units','Normalized',...
577     'Position',[0.45,0.1,0.1,0.04],...
578     'String','Save Results',...
579     'Tag','btn_saveDate',...
580     'CallBack',{@saveDataFcn});
581 
582 hlbl_saveDir=uicontrol('Parent',hfig_contours,'Style','text',...
583     'Units','Normalized','HorizontalAlignment','Left',...
584     'Position',[0.45,0.2,0.1,0.02],...
585     'String','Save Directory:');
586 
587 
588 
589 hlbl_saveName=uicontrol('Parent',hfig_contours,'Style','text',...
590     'Units','Normalized','HorizontalAlignment','Left',...
591     'Position',[0.45,0.15,0.1,0.02],...
592     'String','Mat Filename:');
593 
594 saveName=strsplit(htxt_directory.String,'\');
595 saveName=saveName(length(saveName)-2);
596 saveName=saveName{:};
597 htxt_saveName=uicontrol('Parent',hfig_contours,'Style','edit',...
598     'Units','Normalized',...
599     'Position',[0.55,0.15,0.2,0.03],...
600     'Tag','txt_saveName',...
601     'String',saveName);
602 
```

```
603 saveDir=[htxt_directory.String '\Image Processing Results' ' (' saveName
        ')'];
604 mkdir(saveDir);
605
606 htxt_saveDir=uicontrol('Parent',hfig_contours,'Style','edit',...
607     'Units','Normalized',...
608     'Position',[0.55,0.2,0.2,0.03],...
609     'Tag','txt_saveDir',...
610     'String',saveDir);
611
612 hpanel_contoursFig=uipanel('Parent',hfig_contours,'Units','normalized'
        ,...
613     'Position',[0.01,0.45,.99,.5],'Tag','panel_contoursFig');
614 hpanel_contour10 = uipanel('Parent',hpanel_contoursFig,'Units','
        normalized',...
615     'Position',[0 0 0.32 1],'Tag','panel_contour10');
616 ax1 = axes('parent',hpanel_contour10);
617
618
619 hpanel_contour50 = uipanel('Parent',hpanel_contoursFig,'Units','
        normalized',...
620     'Position',[0.34 0 0.32 1],'Tag','panel_contour50');
621 ax2 = axes('parent',hpanel_contour50);
622
623
624 hpanel_contour90 = uipanel('Parent',hpanel_contoursFig,'Units','
        normalized',...
625     'Position',[0.68 0 0.32 1],'Tag','panel_contour90');
626 ax3 = axes('parent',hpanel_contour90);
627
628
629
```

```
630
631
632
633 % subplot(1, 3, 2);
634 imshow(flame_contour50,'parent',ax2);
635 % setappdata(hfig_imgImport,'axes_contour50',ax2)
636
637 rectangle('Position',flameBox,'EdgeColor','r',...
638     'LineWidth', 1,'parent',ax2,'Tag','plot_boxContour50');
639 flameLengthText=sprintf('Flame length: %0.2f cm (=%0.2fD)',flameLength*
    px2cm,flameLength/Noz_D);
640 text(0,50,flameLengthText,'Color','green','parent',ax2,'Tag','
    plot_textContour50')
641 % setappdata(hfig_imgImport,'axes_contour50_boxText',ax2)
642
643 title('50% intermittency contour','parent',ax2)
644
645
646 % subplot(1, 3, 1);
647 imshow(flame_contour10,'parent',ax1)
648 % setappdata(hfig_imgImport,'axes_contour10',ax1)
649
650 title('10% intermittency contour','parent',ax1)
651
652
653 % subplot(1, 3, 3);
654 imshow(flame_contour90,'parent',ax3)
655 % setappdata(hfig_imgImport,'axes_contour90',ax3)
656
657 title('90% intermittency contour','parent',ax3)
658
659
```

```
660 %% Necking location function
661 hfig_necking=figure(2);
662 set(hfig_necking,'Name','Flame necking finder',...
663     'Tag','fig_necking',...
664     'NumberTitle','off',...
665     'Units','Normalized',...
666     'Position',[0.2,0.1,0.4,0.8]);
667
668
669
670 hpanel_neckImg = uipanel('Parent',hfig_necking,'Units','normalized',...
671     'Position',[0.01,0.14,0.98,0.85],'Tag','panel_neckImg');
672 ax1 = axes('parent',hpanel_neckImg,'ActivePositionProperty','Position','
    Position',[0 0 1 1]);
673 % ax1 = axes('Position',[0.01,0.14,0.98,0.85],'Box','on');
674 hpopmenu_neckPick=uicontrol(hfig_necking,'Style','popupmenu',...
675     'Units','Normalized',...
676     'Position',[0.5,0.1,0.1,0.03],...
677     'Tag','popmenu_neckPick',...
678     'String',0,...
679     'Callback',{@neckPopFcn});
680
681 hlbl_neckPick=uicontrol('Parent',hfig_necking,'Style','text',...
682     'Units','Normalized','HorizontalAlignment','Left',...
683     'Position',[0.35,0.09,0.14,0.03],...
684     'String','Select neck to save:');
685
686
687 burner_y=coords(1,2); % Read burner y location from burner_Rim
688
689 % Smooth contour edges by blurring the image and re-binarizing
```

```
690 windowSize = 10; % Larger windows result in higher blurring. Window
        sizes of 5~10 work well
691 kernel = ones(windowSize) / windowSize ^ 2;
692 blurryImage = conv2(single(flame_contour50), kernel, 'same');
693 contour50_smooth = blurryImage > 0.5;
694
695 setappdata(hfig_imgImport,'matrix_contour50_smooth',contour50_smooth)
696
697 %Loop over the the vertical location from burner tip up to 2*D_burner
        above
698 %the tip
699 for i=burner_y:-1:burner_y-2*Noz_D
700
701     whiteRegion(i).colIndex=find(contour50_smooth(i,:)==1); %Store non-
            zero pixels at this vertical location in a structure variable (in
             the field "colIndex")
702     whiteRegion(i).width=max(whiteRegion(i).colIndex)-min(whiteRegion(i).
            colIndex); %Calculate flame width at this vertical location
703
704
705 end
706 % figure(2)
707 imshow(contour50_smooth,'Parent',ax1);
708 hold on
709 neck_yLocation_all=0;
710 neck_width_all=0;
711 firstX_all=0;
712 lastX_all=0;
713 minimum_counter=0;
714 % Find extrema
715 for i=burner_y-1:-1:burner_y-2*Noz_D+1
716
```

```
717     width=whiteRegion(i).width;
718     width_plus=whiteRegion(i+1).width;
719     width_minus=whiteRegion(i-1).width;
720
721     %check if current y is within flame region
722     if ~isempty(width) && ~isempty(width_plus) && ~isempty(width_minus)
723
724     k=i-1;
725     % If width at y-1 is equal to width at y, check smaller y's until it
            's
726     % not equal (to avoid missing a minimum when the edge becomes
727     % vertically flat);
728     while width_minus==width && k>burner_y-2*Noz_D
729         k=k-1;
730         width_minus=whiteRegion(k).width;
731
732     end
733 %     width_plus=mean([whiteRegion(i+1:i+5).width]);
734 %     width_minus=mean([whiteRegion(i-5:i-1).width]);
735
736     if whiteRegion(i).width<width_minus && whiteRegion(i).width<
            width_plus
737         minimum_counter=minimum_counter+1; %In case more than one minima
                is found
738         neck_yLocation_all(minimum_counter)=i;
739         neck_width_all(minimum_counter)=whiteRegion(i).width;
740         firstX_all(minimum_counter)=whiteRegion(i).colIndex(1);
741         lastX_all(minimum_counter)=whiteRegion(i).colIndex(end);
742         plot([firstX_all(minimum_counter) lastX_all(minimum_counter)],
                neck_yLocation_all(minimum_counter)*ones(1,2),'r','Tag','
                neckLines')
```

```
743             text(firstX_all(minimum_counter)+width/2, neck_yLocation_all(
                    minimum_counter),num2str(minimum_counter),'Tag','neckLines')
744         end
745
746         end
747
748 end
749
750 if minimum_counter==0
751
752         hpopmenu_neckPick.String={'No necking'};
753         hpopmenu_neckPick.Value=1;
754         slectedNeck=str2double(hpopmenu_neckPick.String(hpopmenu_neckPick.
                Value));
755
756 else
757
758         hpopmenu_neckPick.String={'No necking',1:minimum_counter};
759         hpopmenu_neckPick.Value=2;
760         slectedNeck=str2double(hpopmenu_neckPick.String(hpopmenu_neckPick.
                Value));
761
762 end
763
764
765 if ~isnan(slectedNeck)
766 neck_yLocation=neck_yLocation_all(slectedNeck);
767 setappdata(hfig_imgImport,'data_contour50_neck_yLocation',neck_yLocation
        )
768 neck_xLocation=[firstX_all(slectedNeck) lastX_all(slectedNeck)];
769 setappdata(hfig_imgImport,'data_contour50_neck_xLocation',neck_xLocation
        )
```

```
770 neck_width=neck_width_all(slectedNeck);
771 setappdata(hfig_imgImport,'data_contour50_neck_width',neck_width)
772 neck_height=burner_y-neck_yLocation;
773 setappdata(hfig_imgImport,'data_contour50_neck_height',neck_height)
774
775 else
776     setappdata(hfig_imgImport,'data_contour50_neck_yLocation',NaN)
777     setappdata(hfig_imgImport,'data_contour50_neck_xLocation',NaN)
778     setappdata(hfig_imgImport,'data_contour50_neck_width',NaN)
779     setappdata(hfig_imgImport,'data_contour50_neck_height',NaN)
780
781 end
782
783
784     function neckPopFcn(hObject,~)
785         slectedNeck=str2double(hObject.String(hObject.Value));
786         if ~isnan(slectedNeck)
787             neck_yLocation=neck_yLocation_all(slectedNeck);
788             setappdata(hfig_imgImport,'data_contour50_neck_yLocation',
                    neck_yLocation)
789             neck_xLocation=[firstX_all(slectedNeck) lastX_all(
                    slectedNeck)];
790             setappdata(hfig_imgImport,'data_contour50_neck_xLocation',
                    neck_xLocation)
791             neck_width=neck_width_all(slectedNeck);
792             setappdata(hfig_imgImport,'data_contour50_neck_width',
                    neck_width)
793             neck_height=burner_y-neck_yLocation;
794             setappdata(hfig_imgImport,'data_contour50_neck_height',
                    neck_height)
795
796
```

```
797         else
798             setappdata(hfig_imgImport,'data_contour50_neck_yLocation',
                    NaN)
799             setappdata(hfig_imgImport,'data_contour50_neck_xLocation',
                    NaN)
800             setappdata(hfig_imgImport,'data_contour50_neck_width',NaN)
801             setappdata(hfig_imgImport,'data_contour50_neck_height',NaN)
802
803         end
804
805
806     end
807
808
809
810
811 %% Save button function
812     function saveDataFcn(hObject,event)
813
814
815         saveName=htxt_saveName.String;
816         saveDir=htxt_saveDir.String;
817         saveFileDir=fullfile(saveDir,saveName);
818
819
820 %         haxes_contour10=getappdata(hfig_imgImport,'axes_contour10');
821         fignew = figure('Visible','off'); % Invisible figure
822         newAxes=imshow(flame_contour10);
823         title('10% intermittency contour')
824 %         newAxes = copyobj(haxes_contour10,fignew); % Copy the
    appropriate
825 %         axes
```

```
826         saveas(newAxes,fullfile(saveDir, [saveName '_contour10']),'png')
827         delete(fignew);
828
829
830 %         haxes_contour50_boxText=getappdata(hfig_imgImport,'
    axes_contour50_boxText');
831         fignew = figure('Visible','off'); % Invisible figure
832         newAxes=imshow(flame_contour50);
833         title('50% intermittency contour')
834         rectangle('Position',flameBox,'EdgeColor','r',...
835             'LineWidth', 1);
836         flameLengthText=sprintf('Flame length: %0.2f cm (=%0.2fD)',
              flameLength*px2cm,flameLength/Noz_D);
837         text(0,50,flameLengthText,'Color','green')
838         %         newAxes = copyobj(haxes_contour50_boxText,fignew); %
              Copy
839         %         the appropriate axes
840         saveas(newAxes,fullfile(saveDir, [saveName '_contour50_boxText'
              ]),'png')
841         delete(fignew);
842
843
844 %         haxes_contour50=getappdata(hfig_imgImport,'axes_contour50');
845         fignew = figure('Visible','off'); % Invisible figure
846         newAxes=imshow(flame_contour50);
847         title('50% intermittency contour')
848 %         newAxes = copyobj(haxes_contour50,fignew); % Copy the
    appropriate
849 %         axes delete(findobj(newAxes,'Tag','plot_boxContour50'))
850 %         delete(findobj(newAxes,'Tag','plot_textContour50'))
851         saveas(newAxes,fullfile(saveDir, [saveName '_contour50']),'png')
852         delete(fignew);
```

```
853
854
855         fignew = figure('Visible','off'); % Invisible figure
856         newAxes=imshow(contour50_smooth);
857         title('50% intermittency contour, Smoothed edge')
858         saveas(newAxes,fullfile(saveDir, [saveName '_contour50_smooth'])
                ,'png')
859         delete(fignew);
860
861
862         if ~isnan(getappdata(hfig_imgImport,'
                data_contour50_neck_yLocation'))
863
864             neck_xLocation_savePlot=getappdata(hfig_imgImport,'
                    data_contour50_neck_xLocation');
865             neck_yLocation_savePlot=getappdata(hfig_imgImport,'
                    data_contour50_neck_yLocation');
866             neck_width_savePlot=getappdata(hfig_imgImport,'
                    data_contour50_neck_width');
867             fignew = figure('Visible','off'); % Invisible figure
868             newAxes=imshow(contour50_smooth);
869             hold on
870             title('50% intermittency contour, Necking Location')
871             plot(neck_xLocation_savePlot,neck_yLocation_savePlot*ones
                    (1,2),'r')
872             text(neck_xLocation_savePlot(1)+neck_width_savePlot/4,
                    neck_yLocation_savePlot-15,sprintf('%0.2fD',
                    neck_width_savePlot/Noz_D),'Color','blue','FontSize',6)
873             saveas(newAxes,fullfile(saveDir, [saveName '_contour50_neck'
                    ]),'png')
874             delete(fignew);
875
```

```
876         end
877
878         %           haxes_contour90=getappdata(hfig_imgImport,'
                axes_contour90');
879         fignew = figure('Visible','off'); % Invisible figure
880         newAxes=imshow(flame_contour90);
881         title('90% intermittency contour');
882         %           newAxes = copyobj(haxes_contour90,fignew); % Copy the
883         %           appropriate axes
884         saveas(newAxes,fullfile(saveDir, [saveName '_contour90']),'png')
885         delete(fignew);
886
887         %           matrix_contour10=getappdata(hfig_imgImport,'
                matrix_contour10');
888         %           matrix_contour50=getappdata(hfig_imgImport,'
                matrix_contour50');
889         %           matrix_contour90=getappdata(hfig_imgImport,'
                matrix_contour90');
890         %           contour50_flameBox=getappdata(hfig_imgImport,'
                data_contour50_flameBox');
891         %           contour50_flameLength=getappdata(hfig_imgImport,'
                data_contour50_flameLength');
892         %           contour50_flameWidth=getappdata(hfig_imgImport,'
                data_contour50_flameWidth');
893
894
895
896         setappdata(hfig_imgImport,'case_id',saveName);
897
898         results=getappdata(hfig_imgImport);
899         save(fullfile(saveDir, ['Results_' saveName '.mat']),'results')
900         %           save(fullfile(saveDir, [saveName
```

```
901         %           '.mat']),'matrix_contour10','matrix_contour50','
                matrix_contour90',...
902         %               'contour50_flameBox','contour50_flameLength','
                contour50_flameWidth')
903         %           save(fullfile(saveDir, [saveName '.txt']),...
904         %               'contour50_flameLength','contour50_flameWidth','-
                ascii')
905           disp ('Save results done!')
906           msgbox('Save results done!','Done')
907
908       end
909
910   end
911
912   function noMaxBlobsTxtFcn(hObject,event)
913
914   hfig_imgImport=findobj('Tag','fig_ImgImport');
915   setappdata(hfig_imgImport, 'noMaxBlobs',str2double(hObject.String));
916   end
917
918   function bnrTrsdTxtFcn(hObject,event)
919
920   hfig_imgImport=findobj('Tag','fig_ImgImport');
921   setappdata(hfig_imgImport, 'bnrTrsd',str2double(hObject.String));
922   end
923
924   function flameAttchd_chbxFcn(hObject,~)
925
926   hfig_imgImport=findobj('Tag','fig_ImgImport');
927   setappdata(hfig_imgImport, 'flameAttached',hObject.Value);
928   end
929
```

```
930
931
932 %%Processing functions
933
934 function y=fixOrient(filename)
935
936 y=imread(filename);
937 info=imfinfo(filename);
938 if isfield(info,'Orientation')
939     orient=info(1).Orientation;
940     switch orient
941         case 1
942             %normal, leave the data alone
943         case 2
944             y = y(:,end:-1:1,:);          %right to left
945         case 3
946             y = y(end:-1:1,end:-1:1,:);  %180 degree rotation
947         case 4
948             y = y(end:-1:1,:,:);          %bottom to top
949         case 5
950             y = permute(y, [2 1 3]);      %counterclockwise and upside
                down
951         case 6
952             y = rot90(y,3);               %undo 90 degree by rotating 270
953         case 7
954             y = rot90(y(end:-1:1,:,:));  %undo counterclockwise and left
                /right
955         case 8
956             y = rot90(y);                 %undo 270 rotation by rotating
                90
957         otherwise
```

```
958                 warning(sprintf('unknown orientation %g ignored\n', orient))
                        ;
959         end
960 end
961
962
963 end
964
965
966 function img=preProcess(dir_rawimage)
967
968 % Applies flame base pixel intensity boost and region of interest
969 imgImport_fig=findobj('Tag','fig_ImgImport');
970
971 rawimage=fixOrient(dir_rawimage);
972 [image_height, image_width, ~]=size(rawimage);
973
974 coords=getappdata(imgImport_fig, 'burner_Rim');
975 scaleFactor=getappdata(imgImport_fig, 'px2cm_scale');
976 ROI_rect=floor(getappdata(imgImport_fig, 'ROI_rect'));
977
978
979 if isempty(ROI_rect)
980 ROI_x0=275;
981 ROI_y0=20;
982 ROI_width=1300;
983 ROI_height=2860;
984
985 else
986 ROI_x0=ROI_rect(1);
987 ROI_y0=ROI_rect(2);
988 ROI_width=ROI_rect(3);
```

```
989 ROI_height=ROI_rect(4);
990
991
992
993 end
994
995
996 if isempty(coords)
997     Xmin_Noz=716;
998     Xmax_Noz=862;
999     y_tip=2760;
1000 else
1001     Xmin_Noz=coords(1,1);
1002     Xmax_Noz=coords(2,1);
1003     y_tip=coords(1,2);
1004 end
1005
1006
1007 % ROI_bottomY=ROI_y0+ROI_height;
1008 ROI_bottomY=y_tip+1;
1009 ROI_rightX=ROI_x0+ROI_width;
1010
1011
1012
1013
1014 %%Apply ROI: Set pixels outside ROI to zero
1015 zeroIndices_rows=[1:ROI_y0,ROI_bottomY:image_height];
1016 zeroIndices_cols=[1:ROI_x0,ROI_rightX:image_width];
1017 rawimage(zeroIndices_rows,:,:)=0;
1018 rawimage(:,zeroIndices_cols,:)=0;
1019
1020
```

```
1021
1022 Noz_D=Xmax_Noz-Xmin_Noz+1;
1023 Noz_cntr=(Xmax_Noz+Xmin_Noz)/2;
1024
1025
1026 % htxt_blueFactor=findobj('Tag','txt_boostFactor');
1027 % boost_factor=str2double(htxt_blueFactor.String);
1028 boost_factor=getappdata(imgImport_fig, 'boostFactor');
1029
1030
1031 % htxt_xWinFactor=findobj('Tag','txt_xWinFactor');
1032 % htxt_yWinFactor=findobj('Tag','txt_yWinFactor');
1033 % xwin_ratio=str2double(htxt_xWinFactor.String);
1034 % ywin_ratio=str2double(htxt_yWinFactor.String);
1035
1036 xwin_ratio=getappdata(imgImport_fig, 'xWinBoost');
1037 ywin_ratio=getappdata(imgImport_fig, 'yWinBoost');
1038
1039 y_boost=floor(y_tip-ywin_ratio*Noz_D:1:y_tip);
1040 x_boost=floor(Noz_cntr-xwin_ratio*Noz_D/2:1:Noz_cntr+xwin_ratio*Noz_D/2)
      ;
1041 rawimage(y_boost, x_boost,3)=boost_factor*rawimage(y_boost, x_boost,3);
1042
1043
1044 img=rawimage;
1045
1046
1047 end
1048
1049
1050
1051 function img=imageProcess(raw_image)
```

```
1052
1053 hfig_imgImport=findobj('Tag','fig_ImgImport');
1054 val_noMaxBlobs=getappdata(hfig_imgImport, 'noMaxBlobs');
1055 val_bnrTrsd=getappdata(hfig_imgImport, 'bnrTrsd');
1056
1057 coords=getappdata(hfig_imgImport, 'burner_Rim');
1058 check_flameAttached=getappdata(hfig_imgImport, 'flameAttached');
1059
1060
1061 img_BW= rgb2gray(raw_image);
1062 img_bnr = img_BW > val_bnrTrsd; % Binary intensity threshold
1063
1064 if check_flameAttached==1
1065 img_bnr(coords(1,2),coords(1,1):coords(2,1))=1;
1066 end
1067
1068
1069 flame_blob = bwareafilt(img_bnr, val_noMaxBlobs); % Take the largest n
     blobs
1070
1071 flame_blob = imfill(flame_blob,'holes'); %fill the holes
1072
1073
1074 img=flame_blob;
1075 %           figure(3) imshow(img)
1076
1077
1078
1079 %% draw boundaries
1080
1081 % flame_bnd=bwboundaries(flame_blob,'noholes'); num_blob=size(flame_bnd
     ,1);
```

```
1082 % flame_bnd_all=flame_bnd{1}; for j=2:num_blob
1083 %     flame_bnd_all=[flame_bnd_all; flame_bnd{j}];
1084 % end figure imshow(img_color)
1085
1086 % hold on plot(flame_bnd_all(:,2), flame_bnd_all(:,1), '.')
1087 % title('Binarized with Matlab function and manual threshold')
1088
1089
1090 % figure imshow(flame_blob)
1091
1092
1093 end
1094
1095
1096
1097
1098
1099
1100
1101
1102
1103
1104
1105
1106
1107
1108
1109
1110
1111
1112
1113
```

```
1114
1115
1116
1117
1118
1119
1120
1121
1122
1123
1124
1125
1126
1127 %% To be deleted
1128 % clc clear close all
1129 %
1130 % folder_Raw = 'C:\Users\Mobaseri\Google Drive\UofA Stuff\Flame image
1131 % processing\IMP_Raw\';
1132 %
1133 % img_num=10; fileName=strcat(folder_Raw,sprintf('%.0f', img_num),'.jpg
     ');
1134 % img_color=fixOrient(fileName);
1135 %
1136 %
1137 %
1138 % figure
1139 %
1140 %
1141 % Xmin_Noz=775; Xmax_Noz=955;
1142 %
1143 % y_tip=2630;
1144 %
```

```
1145 % Noz_D=Xmax_Noz-Xmin_Noz+1; Noz_cntr=(Xmax_Noz+Xmin_Noz)/2;
1146 %
1147 % img_color(y_tip-0.5*Noz_D:y_tip,Noz_cntr-1.1*Noz_D/2:Noz_cntr+1.1*
     Noz_D/2,3)=5*img_color(y_tip-0.5*Noz_D:y_tip,Noz_cntr-1.1*Noz_D/2:
     Noz_cntr+1.1*Noz_D/2,3);
1148 %
1149 % imshow(img_color)
1150 %
1151 % hold on %% [x_blu, y_blu]=find(img_color(:,:,3)>100); % plot(y_blu,
1152 % x_blu, '.')
1153 %
1154 %
1155 %%% img_BW= rgb2gray(img_color); img_bnr = img_BW > 10; % Whatever
     value
1156 % works. flame_blob = bwareafilt(img_bnr, 3); % Take the largest
1157 %
1158 % flame_blob = imfill(flame_blob,'holes');
1159 %
1160 % flame_bnd=bwboundaries(flame_blob,'noholes'); no_blob=size(flame_bnd
     ,1);
1161 % flame_bnd_all=flame_bnd{1}; for j=2:no_blob
1162 %     flame_bnd_all=[flame_bnd_all; flame_bnd{j}];
1163 % end figure(2) imshow(img_color)
1164 %
1165 % hold on plot(flame_bnd_all(:,2), flame_bnd_all(:,1), '.')
1166 % title('Binarized with Matlab function and manual threshold')
1167 %
1168 %
1169 % figure(3) imshow(flame_blob)
1170 %
1171 %%% image import figure configuration
1172 %
```

```
1173 %
1174 %
1175 %
1176 %%
1177 %
1178 % function y=fixOrient(filename)
1179 %
1180 % y=imread(filename); info=imfinfo(filename);
1181 %     if isfield(info,'Orientation')
1182 %         orient=info(1).Orientation; switch orient
1183 %             case 1
1184 %                 %normal, leave the data alone
1185 %             case 2
1186 %                 y = y(:,end:-1:1,:);          %right to left
1187 %             case 3
1188 %                 y = y(end:-1:1,end:-1:1,:);   %180 degree rotation
1189 %             case 4
1190 %                 y = y(end:-1:1,:,:);          %bottom to top
1191 %             case 5
1192 %                 y = permute(y, [2 1 3]);      %counterclockwise and
    upside
1193 %                 down
1194 %             case 6
1195 %                 y = rot90(y,3);               %undo 90 degree by
    rotating
1196 %                 270
1197 %             case 7
1198 %                 y = rot90(y(end:-1:1,:,:));   %undo counterclockwise
    and
1199 %                 left/right
1200 %             case 8
1201 %                 y = rot90(y);                 %undo 270 rotation by
```

```
1202 %                 rotating 90
1203 %             otherwise
1204 %                 warning(sprintf('unknown orientation %g ignored\n',
1205 %                 orient));
1206 %         end
1207 %     end
1208 %
1209 %
1210 % end
```